

# Search for Standard Model Higgs bosons produced in association with top-quark pairs in $t\bar{t}H$ multilepton final states using the ATLAS detector at the LHC.

## DISSERTATION

zur Erlangung des akademischen Grades

doctor rerum naturalium

(Dr. rer. nat.)

im Fach: Physik

Spezialisierung: experimentelle Teilchenphysik

eingereicht an der

Mathematisch-Naturwissenschaftlichen Fakultät der  
Humboldt-Universität zu Berlin

von

MSc. Yasiel Delabat Díaz

Präsidentin der Humboldt-Universität zu Berlin:

Prof. Dr. Sabine Kunst

Dekan der Mathematisch-Naturwissenschaftlichen Fakultät:

Prof. Dr. Elmar Kulke

Gutachter/innen:

1. PD Dr. Judith Katzy
2. Prof. Dr. Thomas Lohse
3. Prof. Dr. Rainer Wallny

Tag der mündlichen Prüfung: 17.11.2020



# Erklärung

Hiermit erkläre ich, die Dissertation selbstständig und nur unter Verwendung der angegebenen Hilfen und Hilfsmittel angefertigt zu haben. Ich habe mich nicht anderwärts um einen Doktorgrad in dem Promotionsfach beworben und besitze keinen entsprechenden Doktorgrad. Die Promotionsordnung der Mathematisch-Naturwissenschaftlichen Fakultät, veröffentlicht im Amtlichen Mitteilungsblatt der Humboldt-Universität zu Berlin Nr. 42 am 11. Juli 2018, habe ich zur Kenntnis genommen.

I declare that I have completed the thesis independently using only the aids and tools specified. I have not applied for a doctor's degree in the doctoral subject elsewhere and do not hold a corresponding doctor's degree. I have taken due note of the Faculty of Mathematics and Natural Sciences PhD Regulations, published in the Official Gazette of Humboldt-Universität zu Berlin no. 42 on July 11 2018.

Hamburg, 11.05.2020

*Yasiel Delabat Díaz*





*A mi Yordi,  
Sin cuyo apoyo este trabajo  
hubiera sido imposible.*



# Acknowledgments

This work would not have been possible without the support of many people during these last three and a half years.

I would like to specially thank my supervisor, Judith Katzy, for giving me the extraordinary opportunity to work in the exciting and challenging world of particle physics. Her guidance and dedication has been invaluable to me both scientifically and personally.

I would also like to thank my colleagues of the Top group at DESY-Hamburg, Stefan, Loïc, Chris, Xingguo and Paul, for their willingness to help with any question, and specially to Kirill for his time and effort reviewing this thesis.

To my family, although far, I thank for their constant support and confidence.

Finally, to my wife Yoana, I owe my deepest gratitude. Thank you for being always by my side and believing in me, even when I did not.



# Abstract

This thesis describes the search for the associated production of a Higgs boson and a top-quark pair in proton-proton collisions with a center-of-mass energy of 13 TeV. The analysis focuses on events containing two leptons with same-sign electric charge or exactly three leptons in the final state. With these requirements, the analysis is sensitive to the  $H \rightarrow WW^*$ ,  $H \rightarrow ZZ^*$  and  $H \rightarrow \tau^-\tau^+$  Higgs decay modes. The used data was recorded with the ATLAS detector at the Large Hadron Collider (LHC) during the 2015-17 period.

The primary sources of background were found to be  $t\bar{t}W$ ,  $t\bar{t}(Z/\gamma^*)$ , Diboson processes and events containing fake or non-prompt leptons coming from hadron decays, photon conversions and electron charge mis-identification. The estimation of the hadron decay and photon conversion fake backgrounds was performed using a novel semi-data driven technique where Monte Carlo background categories are created for each fake process of interest. A profile likelihood fit to data is then used to extract a normalization factor for each fake category, which are used to correct the Monte Carlo predictions. The ratio of the measured  $t\bar{t}H$  signal cross-section to the Standard Model expectations,  $\mu_{t\bar{t}H}$ , and a normalization factor for the  $t\bar{t}W$  process are extracted simultaneously from the same fit.

The  $\mu_{t\bar{t}H}$  for a Standard Model Higgs boson of mass 125 GeV was found to be  $\mu_{t\bar{t}H} = 0.88^{+0.37}_{-0.36}(stat)^{+0.39}_{-0.36}(syst)$  with an observed (expected) significance of 1.80 (2.52) standard deviations. This corresponds to an estimated  $t\bar{t}H$  cross-section of  $446^{+241}_{-227}$  fb, in agreement with the Standard Model prediction of  $507^{+35}_{-50}$  fb.



# Zusammenfassung

Diese Arbeit beschreibt die Suche nach assoziierter Produktion eines Higgsbosons und eines Top-Quark Paares in Proton-Proton Kollisionen bei einer Schwerpunktsenergie von 13 TeV. Für diese Analyse wurden Ereignisse analysiert, die exakt zwei Leptonen mit gleichem Ladungsvorzeichen oder exakt drei Leptonen enthalten und daher auf die Higgs Zerfallsmoden in  $H \rightarrow WW^*$ ,  $H \rightarrow ZZ^*$  und  $H \rightarrow \tau^-\tau^+$  sensitiv sind. Die Daten wurden mit dem ATLAS Detektor am Large Hadron Collider (LHC) in den Jahren 2015-17 aufgezeichnet.

Der grösste Untergrund in beiden Kanälen stammt aus assoziierter Produktion von Vektorbosonen mit einem Top-Quark Paar ( $t\bar{t}W$  und  $t\bar{t}(Z/\gamma^*)$ ), Dibosonproduktion und Ereignisse, die Photonen und Hadronen, die fehlerhaft als Leptonen identifiziert wurden, erhalten oder Leptonen, die aus Zerfällen von Hadronen stammen. Der Leptonuntergrund wurde mit einer neuen Methode abgeschätzt, die auf separaten Kategorien für jeden Produktionsmodus des Leptonuntergrundes basiert. Der Beitrag jeder Kategorie wird in verschiedenen Kontrollregionen aus dem Vergleich von Daten mit der Simulation bestimmt. Das Verhältnis des gemessenen  $t\bar{t}H$  Wirkungsquerschnitts zu der Vorhersage des Standardmodells,  $\mu_{t\bar{t}H}$ , und die Normierungsfaktoren des Untergrundes werden gleichzeitig in einem Profile-Likelihood-Fit bestimmt.

Das Verhältnis  $\mu_{t\bar{t}H}$ , unter der Annahme einer Higgsbosonmasse von 125 GeV, wurde zu  $\mu_{t\bar{t}H} = 0.88^{+0.37}_{-0.36}(stat)^{+0.39}_{-0.36}(syst)$  mit einer beobachteten (erwarteten) Signifikanz von 1.80 (2.52) Standardabweichungen gemessen. Das entspricht einem geschätzten Wirkungsquerschnitt für die  $t\bar{t}H$  Produktion von  $446^{+241}_{-227}$  fb, in Übereinstimmung mit der Standardmodellvorhersage von  $507^{+35}_{-50}$  fb.





# Contents

Acknowledgments	i
Abstract	iii
Introduction	1
<b>1 The Higgs boson in the Standard Model</b>	<b>3</b>
1.1 The Standard Model of particle physics . . . . .	3
1.1.1 Symmetries and gauge invariance . . . . .	5
1.1.2 Electromagnetic interaction . . . . .	6
1.1.3 Strong interaction . . . . .	7
1.1.4 Electroweak interaction . . . . .	8
1.1.5 Spontaneous symmetry breaking and the Higgs mechanism . . . . .	11
1.2 Higgs boson production and decay . . . . .	14
1.3 Measurement of Higgs boson properties . . . . .	16
1.4 Current status of $t\bar{t}H$ searches . . . . .	17
1.5 Measurements of the top Yukawa coupling . . . . .	19
<b>2 The ATLAS experiment at the Large Hadron Collider</b>	<b>21</b>
2.1 LHC accelerator complex . . . . .	21
2.1.1 Luminosity and pileup . . . . .	22
2.2 The ATLAS detector . . . . .	24
2.2.1 Inner detector . . . . .	26
2.2.2 Calorimeters . . . . .	29
2.2.3 Muon spectrometer . . . . .	33
2.2.4 Trigger system . . . . .	34
<b>3 Objects reconstruction and identification</b>	<b>37</b>
3.1 Tracks and primary vertex . . . . .	37
3.2 Leptons . . . . .	39
3.2.1 Electrons . . . . .	39
3.2.2 Muons . . . . .	44

3.2.3	Fake and non-prompt leptons . . . . .	47
3.3	Jets . . . . .	49
3.3.1	Jet energy scale calibration . . . . .	50
3.3.2	Jet energy resolution . . . . .	52
3.3.3	$b$ -jets identification . . . . .	53
3.4	Missing transverse energy . . . . .	54
3.5	Ambiguity resolution in objects selection . . . . .	55
4	<b>Search for Higgs bosons produced in association with top-quark pairs in multilepton final states</b>	<b>57</b>
4.1	Data and Monte Carlo samples . . . . .	58
4.1.1	Data taking . . . . .	58
4.1.2	Triggered data events . . . . .	59
4.1.3	Monte Carlo samples . . . . .	59
4.2	Physics objects selections . . . . .	64
4.2.1	Lepton selection . . . . .	64
4.2.2	Jet selection . . . . .	67
4.3	Selection of $t\bar{t}H$ signal events . . . . .	68
4.3.1	Signal selection in the $2\ell SS$ channel . . . . .	68
4.3.2	Signal selection in the $3\ell$ channel . . . . .	68
4.4	Background processes . . . . .	70
4.4.1	Backgrounds containing fake leptons . . . . .	71
4.4.2	Background from other physics processes . . . . .	73
4.5	Event categorization . . . . .	73
4.5.1	Fake-dominated event categories. . . . .	75
4.5.2	$2\ell SS$ channel categories. . . . .	76
4.5.3	$3\ell$ channel categories. . . . .	81
4.6	Statistical model description . . . . .	82
4.6.1	The maximum likelihood method . . . . .	83
4.6.2	Definition of the test statistic and the fit significance . . . . .	86
4.6.3	Treatment of systematic uncertainties . . . . .	89
4.7	Fit results . . . . .	94
	<b>Conclusions and Outlook</b>	<b>101</b>
	<b>Bibliography</b>	<b>103</b>

---

# Introduction

An important milestone for the physics program at the Large Hadron Collider (LHC) was achieved in 2012 with the discovery of the Higgs boson by the ATLAS and CMS collaborations [1, 2]. It constituted the last missing piece of the Standard Model (SM) [3] of particle physics, which helped explain how particles acquire mass.

Ever since then, precise measurement of the Higgs boson properties have been of paramount importance as any potential disagreement with the SM could indicate the existence of new physics phenomena. For example, any deviation from the SM predictions of the fermion Yukawa couplings could be very sensitive to physics beyond the Standard Model (BSM) [4]. Since the top-quark is the heaviest fundamental particle in the SM, its coupling to the Higgs boson is expected to be the strongest. Thus, the search for the SM Higgs boson produced in association with a top quark pair (i.e.  $t\bar{t}H$  processes) plays a crucial role in the LHC physics program.

The  $t\bar{t}H$  production cross-section is low ( $\sim 1\%$ ) compared to other Higgs boson production mechanisms accessible at the LHC. However,  $t\bar{t}H$  provides a direct method of probing the top Yukawa coupling, as it does not require loop diagrams to describe the interaction at leading order in perturbation theory. This significantly reduces the dependence of the coupling measurement procedure on specific model hypotheses, and disentangles it from any potential effect due to non-SM particles. The ATLAS and CMS experiments have reported observation of the  $t\bar{t}H$  production with a statistical significance in excess of  $5\sigma$  by combining all the Higgs decay modes [5, 6]. In particular, for the  $H \rightarrow \gamma\gamma$  decay channel, observations with statistical significances of  $5.2\sigma$  and  $6.6\sigma$  have been achieved by ATLAS [7] and CMS [8] respectively.

This thesis describes the search of  $t\bar{t}H$  production in multilepton final states ( $t\bar{t}HML$ ), which are sensitive to the  $H \rightarrow WW^*$ ,  $H \rightarrow ZZ^*$  and  $H \rightarrow \tau^-\tau^+$  decay modes. The analysis uses data collected during 2015, 2016 and 2017 at a center-of-mass energy ( $\sqrt{s}$ ) of 13 TeV by the ATLAS detector. This corresponds to more than double the amount of data utilized in the previous  $t\bar{t}HML$  searches [5]. The focus of this analysis lies on the two most sensitive  $t\bar{t}HML$  channels: one with exactly two same-sign leptons in the final state ( $2\ell SS$ ), and the other with exactly three leptons ( $3\ell$ ).

This thesis is structured as follows. Chapter 1 contains a short overview of the Standard Model of particle physics. Particular emphasis is made on the Spontaneous Symme-

---

try Breaking (SSB) in the electroweak sector, which justifies the mass degree of freedom of the  $W/Z$  bosons and fermions through the Higgs mechanism. It also provides a summary of the current status of Higgs boson searches at the LHC and a review of the most recent measurements of its properties, focusing on the top quark coupling.

Chapter 2 gives a broad description of the LHC accelerator complex and the ATLAS detector. This description includes only those characteristics relevant to the reconstruction of the physics objects used in this thesis.

A detailed description of the objects reconstruction and identification processes as well as their performance is presented in Chapter 3.

Finally, Chapter 4 describes the  $t\bar{t}HML$  analysis performed in this thesis. It provides details about the event selection targeting the  $2\ell SS$  and  $3\ell$  final states and describes the main backgrounds estimation strategy. In particular, background events containing fake leptons are estimated using a novel semi-data driven technique, where Monte Carlo background categories are created for each fake process of interest. These estimations are later adjusted using scale factors derived from a likelihood fit to data. From this fit, normalization factors for the  $t\bar{t}H$  signal and specific background events are simultaneously extracted and the results are compared with the SM expectations. The fit is performed across several event categories, defined by cuts on kinematic properties of the selected events in order to produce regions of phase-space enriched in  $t\bar{t}H$  signal or the background events of interest.

---

# Chapter 1

## The Higgs boson in the Standard Model

This chapter presents an overview of the Standard Model (SM) of particle physics. Special focus is dedicated to describe the interaction between the Higgs boson and fermions. In particular, given its importance for the analysis presented here, the coupling of the Higgs boson and the top-quark is described.

In Section 1.1, a brief summary of the properties of elementary particles and their interactions within the SM is presented. Sections 1.2 and 1.3 contain a description of the Higgs boson production and decay mechanisms as well as the measurement of its most important properties. An overview of the current status of  $t\bar{t}H$  searches and measurements of the top Yukawa coupling is given in Sections 1.4 and 1.5.

### 1.1 The Standard Model of particle physics

The current understanding of the elementary particles and their interactions is included in the theoretical framework known as the Standard Model of particle physics [3]. The modern form of the SM was established in the 1960s by S. Glashow [9], A. Salam [10] and S. Weinberg [11]. It consists in a quantum field theory (QFT) that collectively describes the electromagnetic, weak and strong interactions among elementary particles<sup>1</sup>.

Figure 1.1 shows a schematic representation of the elementary particles conforming the SM. As shown, three types of particles are distinguished in the SM: *quarks*, *leptons* and *bosons*. Leptons and quarks have spin-1/2 and are described by Fermi-Dirac statistics (fermions). In the SM, fermions are organized in three *generations* of particles. Each generation contains two quarks and two leptons.

---

<sup>1</sup>Gravitational interaction is not included in the SM formulation. However, its effects are very weak at quantum scales and thus, negligible for the purposes of this work.

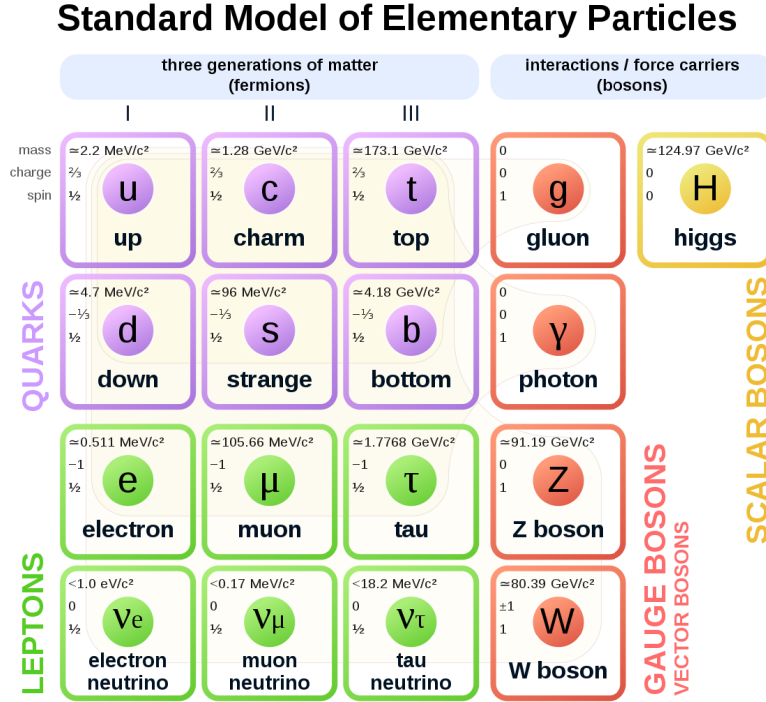


**Figure 1.1:** Schematic representation of the Standard Model (SM) of particle physics consisting of three generations of quarks, leptons, and neutrinos as well as five force carrying bosons [12]. For each particle, the mass, spin and electric charge is given.

Most of the matter<sup>2</sup> in the universe is composed of electrons, up- and down-quarks, which belong to the first generation of particles in the SM. Fermions from the other two generations are identical to their first generation counterpart except for their higher masses. Thus, charm and top-quarks are called “up-type” or “up-like” quarks while strange- and bottom-quarks are called “down-type” or “down-like” quarks. All fermions, except neutrinos, are electrically charged: leptons have unit charge, whereas quarks are characterized by fractional electric charges. Moreover, each fermion has a “partner” with the same mass, but opposite charge<sup>3</sup>, called *anti*-particle.

The fermion interactions are mediated by spin-1 particles that obey Bose-Einstein statistics (bosons): gluons ( $g$ ), photons ( $\gamma$ ), and  $Z^0/W^\pm$  bosons. In addition, the SM also includes the mechanism through which particles can obtain mass (discussed in more detail in Section 1.1.5) by interacting with a scalar (spin-0) field, which is quantized in the form of Higgs bosons.

Electrically charged particles interact through the *electromagnetic force*. This interaction is mediated by photons, the quanta of the electromagnetic field. Furthermore, all

<sup>2</sup>Here matter refers specifically to the  $\sim 5\%$  *visible* matter present in the universe. Invisible (dark) matter and energy constitute the remaining  $\sim 95\%$ .

<sup>3</sup>In this context, “opposite charge” refers to the *charge conjugate*, which not only inverts electric charge but also lepton, baryon and strangeness numbers.

fermions in the SM can interact via the *weak force*, which is mediated by the massive  $W^\pm$  or  $Z^0$  vector bosons. In the SM, both interactions are treated as different manifestations of the same fundamental force, called *Electroweak* (EW) interaction [13].

Quarks are the only particles that can interact through the *strong force* by exchanging gluons. This is the case due to a unique property of quarks: *color*. The gluon exists in eight different quantum states and carries a combination of color and anti-color charge. Within the SM, the dedicated QFT that describes the strong interaction is called Quantum Chromodynamics (QCD).

### 1.1.1 Symmetries and gauge invariance

The Standard Model is based on the Lagrangian formalism and the fundamental notion of symmetries, which are related to conservation laws through the Noether's theorem [14]. This theorem states that for every differentiable symmetry generated by local actions there corresponds a conserved quantity. The eigenvalues of operators related to conserved quantities are called *quantum numbers*. Thus, each symmetry is associated with a specific quantum number (a set of quantum numbers characterize the *quantum state* of a particle). Two types of symmetries can be identified:

- (i) **Global Symmetries:** Obtained when the Lagrangian is invariant under transformations that are independent of the space-time coordinates (i.e., invariant with respect to *global* phase transformations). These symmetries are related to particle quantum number such as spin (rotational symmetry) and parity (related to the Poincaré symmetry of space-time).
- (ii) **Local Symmetries:** Obtained when the Lagrangian is invariant under transformations that depend on the space-time coordinates (i.e., invariant with respect to *local* phase transformations). These symmetries are related to quantum numbers such as the charge, baryon number, etc.

In the SM theoretical framework, global symmetries are required to also hold locally. This requirement is known as *local gauge invariance*. For the SM, the symmetry that is gauged corresponds to the non-Abelian<sup>4</sup> group  $SU(3) \otimes SU(2)_L \otimes U(1)_Y$ , where the subscript  $L$  implies that the symmetry applies to left-handed fields only and  $Y \equiv 2(Q - T_3)$  denotes the weak hypercharge ( $T_3$  represents the projection of the weak isospin along the z-axis and  $Q$  stands for the electric charge).

The first symmetry group ( $SU(3)$ ) corresponds to the color symmetry. The color quantum number acts as the “charge” of the strong interaction. Differently to the electric charge, which is either *positive* or *negative* (“anti-positive”), color comes in three types:

---

<sup>4</sup>A non-Abelian symmetry group is that where the transformation operators do not commute.

*red*, *green* and *blue* with their corresponding anti-colors (anti-*red*, anti-*green* and anti-*blue*).

The second group ( $SU(2)_L \otimes U(1)_Y$ ) corresponds to the electroweak symmetry group, which is related to transformations of the weak isospin and weak hypercharge and is associated with the conservation of the corresponding quantities.

### 1.1.2 Electromagnetic interaction

The electromagnetic interactions are described by the quantum electrodynamics (QED) theory. For spin-1/2 particles (fermions), the free Lagrangian must satisfy the Dirac equation<sup>5</sup>:

$$i\gamma^\mu \partial_\mu \psi_f - m_f \psi_f = 0 \quad (1.1)$$

This requirement is fulfilled by a Lagrangian of the form:

$$\mathcal{L}_{QED} = \bar{\psi}_f (i\gamma^\mu \partial_\mu - m_f) \psi_f \quad (1.2)$$

where  $\psi_f$  and  $\bar{\psi}_f$  are the fermion field spinor and its adjoint respectively;  $\gamma^\mu$  ( $\mu = 0, 1, 2, 3$ ) are the Dirac matrices and  $m_f$  corresponds to the mass of the fermion.

Next, by requiring local gauge invariance, a vector field  $B_\mu$  (*gauge field*) is introduced, which couples to the fermion field ( $\psi_f$ ) forming a new interaction term in the original free Lagrangian:

$$\mathcal{L}_{QED} = \bar{\psi}_f (i\gamma^\mu \partial_\mu - m_f) \psi_f - (g_e \bar{\psi}_f \gamma^\mu \psi_f) \cdot B_\mu \quad (1.3)$$

where  $g_e$  is the electromagnetic coupling strength factor.

Finally, the photon (spin-1) free Lagrangian is also added and the final QED Lagrangian takes the form:

$$\mathcal{L}_{QED} = \bar{\psi}_f (i\gamma^\mu \partial_\mu - m_f) \psi_f - (g_e \bar{\psi}_f \gamma^\mu \psi_f) \cdot B_\mu - \frac{1}{4} B^{\mu\nu} \cdot B_{\mu\nu} \quad (1.4)$$

where  $B_{\mu\nu}$  is the field strength tensor, which is given by:

$$B_{\mu\nu} \equiv \partial_\mu B_\nu - \partial_\nu B_\mu \quad (1.5)$$

The addition of a mass term of the form  $\frac{1}{2} m_f^2 B_\mu B^\mu$  for photons in Eq. 1.4 would lead to a loss of local gauge invariance and, therefore, the photons must be massless.

---

<sup>5</sup>Natural units  $c = \hbar = 1$  are assumed hereafter unless otherwise specified.



### 1.1.3 Strong interaction

The strong interactions are described by the QCD formulation. It is based on the same principles of QED but extended to account for the quark color. Analogous to the QED case, the QCD Lagrangian for a particular quark flavor  $q$  ( $q = up, down, charm, strange, top, bottom$ ) can be expressed as:

$$\mathcal{L}_{QCD} = \bar{\psi}_q(i\gamma^\mu\partial_\mu - m_q)\psi_q = i\bar{\psi}_q\gamma^\mu\partial_\mu\psi_q - m_q\bar{\psi}_q\psi_q \quad (1.6)$$

However, since each quark flavor comes in three colors, the Lagrangian in Eq. 1.6 takes the form:

$$\mathcal{L}_{QCD} = \bar{\psi}_{q,R}(i\gamma^\mu\partial_\mu - m_q)\psi_{q,R} + \bar{\psi}_{q,G}(i\gamma^\mu\partial_\mu - m_q)\psi_{q,G} + \bar{\psi}_{q,B}(i\gamma^\mu\partial_\mu - m_q)\psi_{q,B} \quad (1.7)$$

where the additional indices  $R, G$  and  $B$  stand for the *Red, Green* and *Blue* colors respectively<sup>6</sup>.

In order to simplify the notation, the following definitions can be made:

$$\psi_q = \begin{pmatrix} \psi_{q,R} \\ \psi_{q,G} \\ \psi_{q,B} \end{pmatrix}, \quad \bar{\psi}_q = (\bar{\psi}_{q,R}, \bar{\psi}_{q,G}, \bar{\psi}_{q,B}) \quad (1.8)$$

In this way, Eq. 1.7 acquires again the form of Eq. 1.6, where now  $\psi_q$  and  $\bar{\psi}_q$  represent three-component vectors (one for each color) of the quark field spinors. This notation will be used hereafter.

The next step is to require local gauge invariance for the Lagrangian in Eq. 1.7 under  $SU(3)$  transformations. Analogous to the QED case, this leads to the introduction of the gluon vector fields  $A_\mu$ :

$$\mathcal{L}_{QCD} = \bar{\psi}_q(i\gamma^\mu\partial_\mu - m_q)\psi_q - (g_S\bar{\psi}_q\gamma^\mu G\psi_q) \cdot A_\mu \quad (1.9)$$

where the factor  $g_S$  is the coupling strength, which is related to the coupling constant by  $\alpha_S = g_S^2/4\pi$ . The factor  $G$  represent the Gell-Mann matrices.

Finally, by adding the gluon (spin-1) free Lagrangian, Eq. 1.9 takes the form:

$$\mathcal{L}_{QCD} = \sum_q \bar{\psi}_q(i\gamma^\mu\partial_\mu - g_S\gamma^\mu G \cdot A_\mu - m_q)\psi_q - \frac{1}{16\pi}F^{\mu\nu} \cdot F_{\mu\nu} \quad (1.10)$$

---

<sup>6</sup>Note that, although the different quark flavors carry different masses (i.e.,  $m_{up} \neq m_{down} \neq m_{charm} \dots$ ), the three color states of a *single* quark flavor are assumed to have the same mass (i.e.,  $m_{q,G} = m_{q,B} = m_{q,R} = m_q$ ).

where the sum accounts for all quark flavors and the last term corresponds to the gluon free Lagrangian with  $F_{\mu\nu}$  being the field strength tensor, which is given by:

$$F_{\mu\nu} \equiv \partial_\mu A_\nu - \partial_\nu A_\mu - 2g_S(A_\mu \times A_\nu) \quad (1.11)$$

where the term  $2g_S(A_\mu \times A_\nu)$  represents the gluon-gluon self-interaction.

Just as in the case of photons, the addition of a mass term for gluons in Eq. 1.10 would lead to a loss of local gauge invariance, therefore, the gluons must be also massless. Furthermore, for the QCD formulation, the quark mass term of the form  $m_q \bar{\psi}_q \psi_q$  does not affect the gauge invariance under  $SU(3)$  transformations. However, when computing the complete SM Lagrangian (i.e. including the Electroweak interaction) this term would indeed “break” the  $SU(2)_L$  symmetry of weak interactions. Therefore, the term for quark masses (and in fact for all fermion masses) is typically included in the electroweak sector through spontaneous symmetry breaking. However, the discussion of this subject will be postpone until Section 1.1.5, where the Higgs mechanism will be introduced.

Moreover, the term  $i\bar{\psi}_q \gamma^\mu \partial_\mu \psi_q$  will appear again in the EW Lagrangian ( $\mathcal{L}_{EW}$ ) due to the fact that quarks also interact weakly. Thus, it is usually considered as part of  $\mathcal{L}_{EW}$  when the  $\mathcal{L}_{SM}$  is computed, to avoid repetition. However, for pure QCD interactions, the Lagrangian given by Eq. 1.10 still holds.

An important characteristic of the strong interaction is the fact that the coupling constant  $\alpha_S$  depends on the separation between the interacting particles. For small distances (less than the size of a proton),  $\alpha_S$  is relatively small (in the order of 0.1). However, for distances equivalent to the size of atomic nuclei ( $\sim 1$  fm),  $\alpha_S$  is in the order of 1. This is known as *asymptotic freedom*. As a consequence, color-charged partons can only be observed experimentally forming colorless bound states, called *hadrons*. The hadron formation is depicted in the example of Figure 1.2. As the distance between a quark/anti-quark pair increases,  $\alpha_S$  also grows. This makes the color lines of the strong field stretch until the increasing potential energy is sufficient to create another  $q\bar{q}$  pair. This process continues until the kinetic energy degrades bellow the threshold at which it is not possible to create more partons. At this point, colorless hadrons are formed from the parton clusters created by each quark.

### 1.1.4 Electroweak interaction

The electroweak formulation unifies the electromagnetic and weak interactions under a single framework. The main challenge of this integration was posed by a unique feature of the weak force: parity violation [15]. This characteristic can be described theoretically

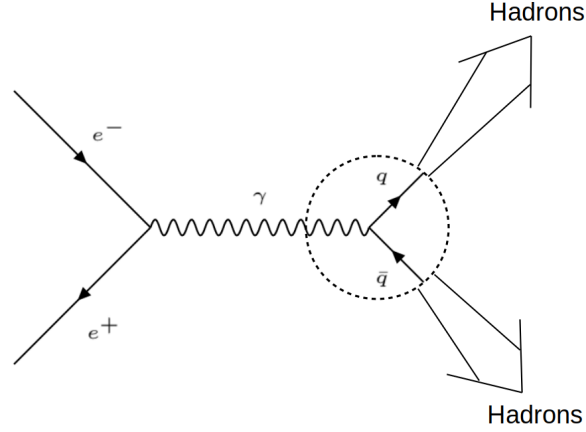


**Figure 1.2:** Example of hadronization in which two hadrons are formed from a quark/anti-quark pair.

if a factor  $(1 \pm \gamma^5)^\dagger$  is added to the Dirac spinors corresponding to the weakly interacting fermions, where  $\gamma^5 = i\gamma^0\gamma^1\gamma^2\gamma^3$ . These factors are called *chirality* operators, which effectively transform the spinor into the left-handed component, meaning that the weak interaction only couples left-handed states:

$$\psi_L = \frac{1}{2}(1 - \gamma^5)\psi \quad \psi'_L = \frac{1}{2}(1 + \gamma^5)\psi' \quad (1.12)$$

where the prime states correspond to anti-particle states.

The corresponding right-handed spinors are:

$$\psi_R = \frac{1}{2}(1 + \gamma^5)\psi \quad \psi'_R = \frac{1}{2}(1 - \gamma^5)\psi' \quad (1.13)$$

Note that  $\psi_L + \psi_R = \psi$ , which means that the electromagnetic interaction spinors can be expressed in terms of chiral spinors.

In the SM, left-handed fermions (neutrinos  $N$ , charged leptons  $E$ , up-type quarks  $U$  and down-type quarks  $D$ ) can be represented in doublets of  $SU(2)_L$  by:

$$\begin{aligned} L_L &= \begin{pmatrix} N \\ E \end{pmatrix}_L = \begin{pmatrix} \nu_e \\ e \end{pmatrix}_L, \begin{pmatrix} \nu_\mu \\ \mu \end{pmatrix}_L, \begin{pmatrix} \nu_\tau \\ \tau \end{pmatrix}_L \\ Q_L &= \begin{pmatrix} U \\ D' \end{pmatrix}_L = \begin{pmatrix} u \\ d' \end{pmatrix}_L, \begin{pmatrix} c \\ s' \end{pmatrix}_L, \begin{pmatrix} t \\ b' \end{pmatrix}_L \end{aligned} \quad (1.14)$$

where the down-type quarks are denoted with a prime due to the flavor mixing in the

---

<sup>†</sup>For left-handed states, the minus sign is used to operate on particles, while the plus sign operates on anti-particles. The opposite is true for right-handed states.

quark sector, described by the Cabibbo-Kobayashi-Maskawa (CKM) mixing matrix  $\mathcal{V}$  in:

$$\begin{pmatrix} d' \\ s' \\ b' \end{pmatrix} = \mathcal{V} \begin{pmatrix} d \\ s \\ b \end{pmatrix} = \begin{pmatrix} V_{ud} & V_{us} & V_{ub} \\ V_{cd} & V_{cs} & V_{cb} \\ V_{td} & V_{ts} & V_{tb} \end{pmatrix} \begin{pmatrix} d \\ s \\ b \end{pmatrix} \quad (1.15)$$

where the experimentally determined elements are [12]:

$$\mathcal{V} = \begin{pmatrix} 0.9738 & 0.2272 & 0.0040 \\ 0.2271 & 0.9730 & 0.0422 \\ 0.0081 & 0.0416 & 0.9991 \end{pmatrix} \quad (1.16)$$

The element  $V_{ud}$ , for example, specifies the coupling of the up to down-quark ( $d \rightarrow u + W^-$ ). Notice that the diagonal elements are the biggest (and close to 1), which indicates that flavor changing weak interactions are most probable to occur within the same quark generation. However, the off-diagonal elements are also non-zero (although much smaller than the diagonal ones), which means that some cross-generation *mixing* is possible. A particularly relevant case for this thesis is the bottom-quark weak decay. The bottom-quark cannot decay within its own generation because the top-quark has higher mass. Instead it can decay to a charm-quark one generation back, but the rate is limited by the mixing coupling ( $V_{cb} = 0.0422$ ). This results in a relatively high life-time of hadrons containing bottom-quark.

On the other hand, the right-handed components of the SM fermions can be represented as singlets<sup>7</sup>:

$$\begin{aligned} E_R &= e_R, \mu_R, \tau_R \\ U_R &= u_R, c_R, t_R \\ D_R &= d_R, s_R, b_R \end{aligned} \quad (1.17)$$

Following the same procedure used in Sections 1.1.2 and 1.1.3 for QED and QCD, in order to preserve gauge invariance two new vector fields are introduced for  $SU(2)_L$  and  $U(1)_Y$  symmetry groups respectively:  $W_\mu^a$  ( $a = 1, 2, 3$ ) and  $B_\mu$ . Then, the Lagrangian for the electroweak interaction takes the form:

$$\mathcal{L}_{EW} = \sum_f \bar{\psi}_f \gamma^\mu (i\partial_\mu - g_W \frac{T^a}{2} W_\mu^a - g_e \frac{Y}{2} B_\mu) \psi_f - \frac{1}{4} W_a^{\mu\nu} \cdot W_{\mu\nu}^a - \frac{1}{4} B^{\mu\nu} \cdot B_{\mu\nu} \quad (1.18)$$

---

<sup>7</sup>Right-handed neutrinos do not exist in the SM, i.e. they only “participate” in the weak part of the electroweak interaction, which has  $SU(2)_L$  symmetry.

In this case, the sum indices ( $f$ ) run over all fermion flavors (leptons and quark flavors). The factor  $g_W$  is the coupling strength factors of the weak interactions. The hypercharge ( $Y$ ) is  $+1/2$  ( $-1/2$ ) for the upper (lower) components of the left-handed doublets  $\psi_L$  and 0 for the right-handed singlets  $\psi_R$ . The Pauli matrices ( $T^a$ ), which are infinitesimal generators of the  $SU(2)_L$  group, are defined as:

$$T^1 = \begin{pmatrix} 0 & 1 \\ 1 & 0 \end{pmatrix}, \quad T^2 = \begin{pmatrix} 0 & -i \\ i & 0 \end{pmatrix}, \quad T^3 = \begin{pmatrix} 1 & 0 \\ 0 & -1 \end{pmatrix} \quad (1.19)$$

They act only on the weak isospin doublets and return zero when applied on right-handed singlets.

The field strength tensors,  $B_{\mu\nu}$  and  $W_{\mu\nu}^a$ , are given by:

$$B_{\mu\nu} = \partial_\mu B_\nu - \partial_\nu B_\mu \quad (1.20)$$

$$W_{\mu\nu}^a = \partial_\mu W_\nu^a - \partial_\nu W_\mu^a - g_W \epsilon_{bc}^a W_\nu^b W_\mu^c \quad (1.21)$$

where  $\epsilon_{bc}^a$  is the Levi-Civita symbol which is  $+1$  ( $-1$ ) for even (odd) permutations of the indices  $a$ ,  $b$  and  $c$  and zero for repeated indices.

Note that the form of the Lagrangian given by Eq. 1.18 differs from the QCD Lagrangian of Eq. 1.10 in one crucial aspect: the fermion mass term of the form  $m_f \bar{\psi}_f \psi_f$ . The introduction of such term here would result in the violation of the chiral symmetry. Furthermore, it is still assumed that all the vector bosons are massless, since the assumption of massive bosons would lead to violation of gauge symmetry. This assumption is valid for the electromagnetic interaction, where the photons are known to be massless. However, it does not hold for the case of weak interactions, where the  $W$  and  $Z$  boson masses have been measured experimentally to be:  $m_{W^\pm} = 80.379 \pm 0.012$  GeV and  $m_{Z^0} = 91.1876 \pm 0.0021$  GeV [12].

In the next section, the resolution of this discrepancy will be discussed. It will be shown how spontaneously breaking the symmetry through the so called *Higgs mechanism* leads to the gauge bosons and the fermions acquiring their masses through the interaction with the Higgs field.

### 1.1.5 Spontaneous symmetry breaking and the Higgs mechanism

Given the necessity of accommodating massive vector bosons for the weak interaction, a formulation known as the *Higgs mechanism*, was introduced in 1964 [16–18]. For this, ad-

ditional isospin doublet of a complex scalar field<sup>8</sup>, known as the Higgs field, is introduced:

$$\phi = \begin{pmatrix} \phi^\dagger \\ \phi^0 \end{pmatrix} = \frac{1}{\sqrt{2}} \begin{pmatrix} \phi_3 + i\phi_4 \\ \phi_1 + i\phi_2 \end{pmatrix} \quad (1.22)$$

The Lagrangian term associated to this scalar field is given by:

$$\mathcal{L}_{Higgs} = \left| \left[ \partial_\mu + i \left( g_W \frac{T^a}{2} W_\mu^a + g_e \frac{Y}{2} B_\mu \right) \right] \phi \right|^2 - V(\phi) \quad (1.23)$$

where the first term describes the kinetic energy of the field while the second term is the Higgs potential:

$$V(\phi) = \mu^2 \phi^\dagger \phi + \frac{\lambda}{2} (\phi^\dagger \phi)^2 = \mu^2 \phi^2 + \frac{\lambda}{2} \phi^4 \quad (1.24)$$

where  $\mu$  and  $\lambda$  are (real) constant parameters.

The first term in Eq. 1.24 can be associated with the mass of the field, while the second term stands for the self-interaction of the field. The “neutral” scalar field ( $\phi^0$ ) in Eq. 1.22 is chosen such that  $V(\phi^0)$  correspond to the minimum of the potential:

$$\left. \frac{\partial V}{\partial \phi} \right|_{\phi=\phi^0} = \phi^0 (\mu^2 + \lambda (\phi^0)^2) = 0 \quad (1.25)$$

Which has solutions of the form:

$$\phi^0 = 0, \quad \phi^0 = \pm \sqrt{\frac{-\mu^2}{\lambda}} = \pm \frac{v}{\sqrt{2}} \quad (1.26)$$

where the quantity  $v$  is referred to as the *vacuum expectation value* (VEV). However, these minima will also depend on the choice of the real constants  $\mu$  and  $\lambda$  in Eq. 1.24.

Only positive  $\lambda$  are allowed to provide a stable global minimum. If  $\mu^2 \geq 0$ , the potential will have the form represented in Figure 1.3 (right), where the minimum corresponds to  $\phi^0 = \phi_1 = \phi_2 = 0$ . This case represents a scalar field with mass  $\mu$ . This is a symmetric ground state under  $SU(2)$ . However, if  $\mu^2 < 0$ , the potential will have the form represented in Figure 1.3 (left). In this case, the trivial solution  $\phi^0 = 0$  does not correspond to a minimum, instead it is a local maximum. Therefore, the solution  $\phi^0 = \pm \frac{v}{\sqrt{2}}$  will correspond to the actual potential minimum. This means that the choice of the physical vacuum state *spontaneously* breaks the symmetry of the Lagrangian.

The expansion of the field around the ground state can be expressed as:

$$\phi = \begin{pmatrix} \eta_3 + i\eta_4 \\ v + \eta_1 + i\eta_2 \end{pmatrix} \quad (1.27)$$

---

<sup>8</sup>The dagger ( $\dagger$ ) symbol here identifies the complex conjugate.

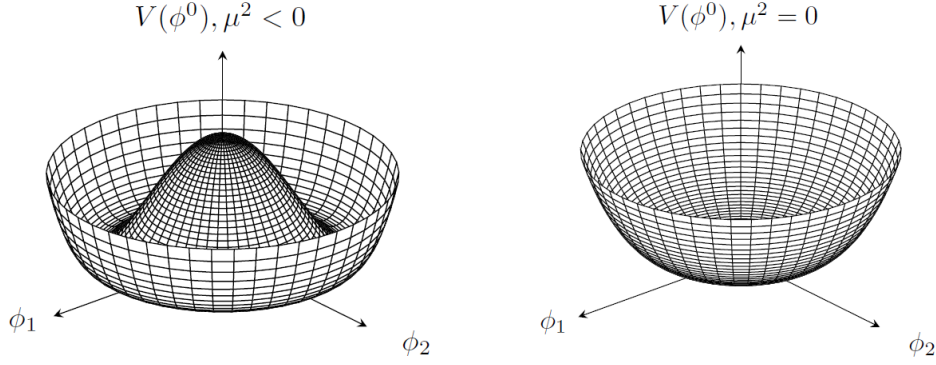


**Figure 1.3:** Higgs potential  $V(\phi^0)$  with  $\lambda > 0$  as a function of the real ( $\phi_1$ ) and imaginary ( $\phi_2$ ) part of the neutral complex scalar field  $\phi^0$  for (left)  $\mu^2 < 0$  and (right)  $\mu^2 = 0$ .

with small perturbations  $\eta_j$  to the vacuum state. Then the Lagrangian becomes:

$$\mathcal{L}_{Higgs} = \frac{1}{2} \sum_{j=1}^4 D_\mu \eta_j D^\mu \eta_j + \mu^2 (\eta_1)^2 + \frac{\lambda v^4}{4} + \mathcal{O}(\eta_1, \eta_2, \eta_3, \eta_4)^3 \quad (1.28)$$

where  $D_\mu$  is the *covariant derivative* operator with the form:

$$D_\mu = \partial_\mu + i \left( g_W \frac{T^a}{2} W_\mu^a + g_e \frac{Y}{2} B_\mu \right) \quad (1.29)$$

The second term of this expression corresponds to a mass term for the Higgs field ( $H \equiv \eta_1$ ) with a mass given by:

$$m_H = \sqrt{-2\mu^2} = \lambda v \quad (1.30)$$

Since  $\lambda$  is not predicted, the theory does not predict  $m_H$  either, and it needs to be determined experimentally.

The other three perturbations are massless fields, which can be associated to Goldstone bosons [19]. In gauge theory they can be removed by proper gauge choices. This transformation leads to masses of three of the vector bosons of electroweak interaction, the charged  $W^\pm$  bosons and the neutral  $Z^0$  boson:

$$m_W = \frac{g_W v}{2} \quad m_Z = \frac{v}{2} \sqrt{g_W^2 + g_e^2} \quad (1.31)$$

It only remains to be discussed how the fermion masses are included in the SM theory. This can be achieved by using the principle of spontaneous symmetry breaking in a similar way to how it was done for the weak vector bosons. Thus, a new Lagrangian term is introduced that describes the interaction among the fermion and the Higgs fields. This

new term is known as the Yukawa interaction Lagrangian and has the form<sup>9</sup>:

$$\mathcal{L}_{Yukawa} = \sum_f y_f [\bar{\psi}_{f,R} \phi \psi_{f,L} + \bar{\psi}_{f,L} \bar{\phi} \psi_{f,R}] + h.c. \quad (1.32)$$

where the sum is carried out over all fermion flavors (leptons and quarks) and  $y_f$  are matrices that contain the Yukawa coupling constants between fermions and the Higgs field. For leptons these matrices are diagonal, but for quarks they are not. However, they can be diagonalized by using unitary transformations that will redefine the fermion fields. For leptons this transformation has no effect due to the absence of right-handed neutrinos. For quarks, however, the rotation to the mass eigenstate basis leads to mixing among the fermion generations, which is the manifestation of the weak interactions. The mixing is characterized by the CKM matrix (Eq. 1.16), presented in Section 1.1.4.

Using the same field expansion described in Eq. 1.27 to the Yukawa Lagrangian in Eq. 1.32, the fermion masses are obtained in the form:

$$m_f = y_f \frac{v}{\sqrt{2}} \quad (1.33)$$

For the particular case of the top-quark Yukawa coupling, taking the measured VEV value of 246 GeV [12] and a top mass of  $\sim 173$  GeV [12], Eq. 1.33 can be expressed as:

$$y_{top} = \frac{\sqrt{2}}{v} \cdot m_{top} \approx 1 \quad (1.34)$$

Since the top-quark is the heaviest fermion, the Higgs coupling to the top-quark is the strongest.

## 1.2 Higgs boson production and decay

In highly energetic proton-proton collisions there are four main mechanisms through which the Higgs boson is produced (see Figure 1.4): gluon-gluon fusion ( $ggF$ ), vector boson fusion ( $VBF$ ), associated production with W/Z bosons ( $WH/ZH$ ) and associated production with a top-quark pair ( $t\bar{t}H$ ). Table 1.1 shows the production cross sections for these mechanisms.

Studies dedicated to determine the top Yukawa coupling use the production mechanisms that involve Higgs coupling to top-quarks, i.e.  $ggF$  and  $t\bar{t}H$  (Figure 1.4 (a) and (b)). Given its large production cross-section in relation with  $t\bar{t}H$ , mainly  $ggF$  has been used to probe this coupling. However, this production mode has a important disadvantage against  $t\bar{t}H$ : it involves the occurrence of a virtual quark loop. This is due to the fact that

---

<sup>9</sup>The term *h.c.* indicates that additional terms corresponding to the Hermitian-Conjugate of all previous ones.



**Table 1.1:** Higgs boson production cross sections corresponding to a center-of-mass energy of 13 TeV [20].

Production mechanism	Cross-section
$ggF$	48.5 pb
$VBF$	3.8 pb
$WH/ZH$	2.4 pb
$t\bar{t}H$	0.5 pb

the Higgs boson does not couples directly to massless particles, such as gluons. Because of this,  $ggF$  offers only an *indirect* way of probing the top Yukawa coupling, since the flavor of the quarks in the loop can not be uniquely determined. However, since the top quark is the heaviest quark (i.e., has the largest Yukawa coupling), the top-quark loop dominates in  $ggF$  production.

In order to *directly* probing the top Yukawa coupling, the  $t\bar{t}H$  production mechanism can be used (Figure 1.4 (b)). This process can be uniquely identified by the presence of the top-quarks in the partonic final state. For that reason, this thesis focuses on the  $t\bar{t}H$  process.

The remaining two production mechanisms,  $VBF$  and  $WH/ZH$  (Figure 1.4 (c) and (d)), do not involve the coupling of a Higgs quark with a top-quark but with vector bosons ( $W^\pm$  or  $Z^0$ ). The former occurs when initial state quarks emit a pair of vector bosons ( $W^\pm$  or  $Z^0$ ) that annihilate to produce a Higgs boson. The latter is also known as *Higgs-strahlung* due to the fact that the Higgs boson is radiated off a virtual vector boson.

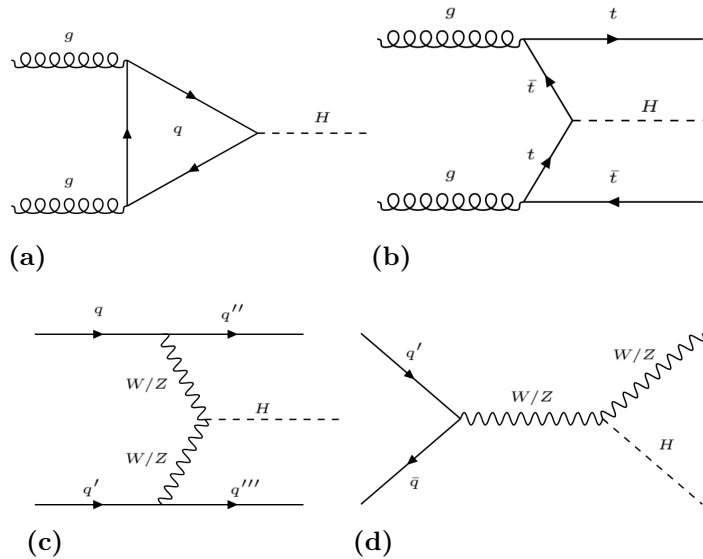


**Figure 1.4:** Example of Higgs boson production Feynman diagrams at leading order for (a)  $ggF$ , (b)  $t\bar{t}H$ , (c)  $VBF$  and (d)  $WH/ZH$ .

The Higgs boson can also be produced in association with a single top-quark. How-

ever, the cross-section of this production process is almost an order of magnitude smaller than the  $t\bar{t}H$  production and is only considered as small background in this thesis.

In addition to the production mechanism, the decay channels of the Higgs boson are also discussed in the following paragraphs. This is due to the fact that the Higgs boson has a very short life-time of about  $10^{-22}$  s and, therefore, it can only be indirectly observed from its decay products.

Table 1.2 shows the most important Higgs decay branching ratios. For fermions, as illustrated by Eq. 1.33, the dominant Higgs boson decay channels correspond to those where heaviest particles are produced<sup>10</sup>. For vector bosons ( $W^\pm$  or  $Z^0$ ), a similar argument can be made (see Eq. 1.31). However, the decay of the Higgs boson into  $W^\pm$  or  $Z^0$  pairs necessarily implies that one of the bosons must be off-shell. Figures 1.5 (a) and 1.5 (b) illustrate these decay channels.

**Table 1.2:** Summary of the most important SM Higgs ( $m_H = 125$  GeV) decay branching ratios ordered from highest to lowest [20]. Particles with a star (\*) represent off-shell particles. Note that for electrically charge particles, their sign must be opposite in order to preserve the neutrality of the Higgs boson.

Decay channel	Branching ratio (%)
$H \rightarrow b\bar{b}$	58.2
$H \rightarrow WW^*$	21.4
$H \rightarrow gg$	8.19
$H \rightarrow \tau\tau$	6.27
$H \rightarrow c\bar{c}$	2.89
$H \rightarrow ZZ^*$	2.62
$H \rightarrow \gamma\gamma$	0.227
$H \rightarrow Z\gamma$	0.153
$H \rightarrow \mu\mu$	0.022

Since the Higgs boson does not couple with massless particles, the decays producing photons and gluons can only occur via loops (Figures 1.5 (c), (d) and (e)). In particular, even though the  $H \rightarrow \gamma\gamma$  channel has a very small branching ratio, it does produce a very clean detector signature, which made it one of the most sensitive channels.

### 1.3 Measurement of Higgs boson properties

One of the most important parameters of the SM is the Higgs boson mass. As mentioned before, its value is not determined by the theory and must be obtained experimentally.

<sup>10</sup>Note that the  $H \rightarrow t\bar{t}$  decay is not possible due to the fact that  $2m_t > m_H$ . The decay  $H \rightarrow t\bar{t}^*$  (with an off-shell top-quark) is still strongly suppressed because  $\bar{t}^*$  would have to be too far away from its mass shell.

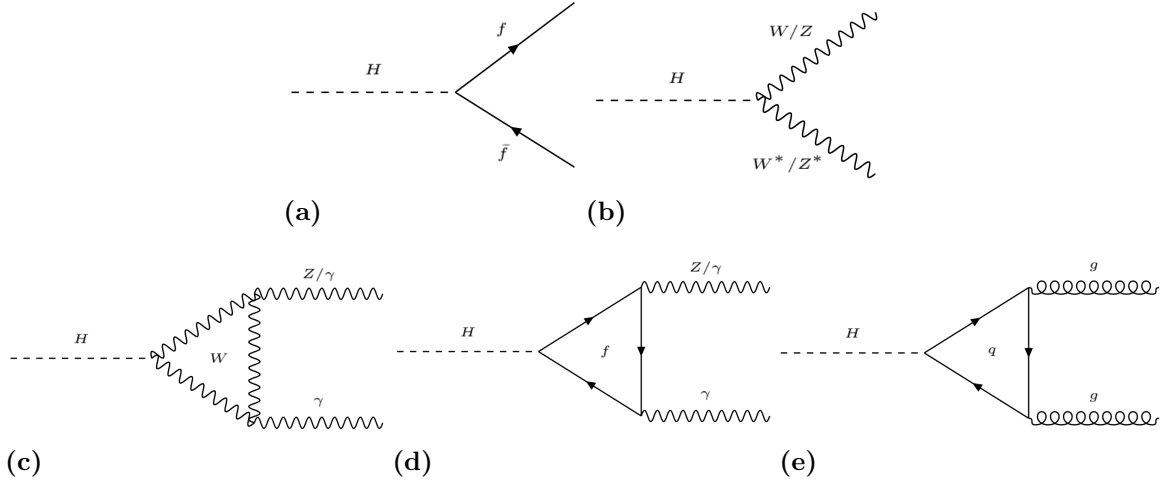


**Figure 1.5:** Examples of leading order Feynman diagrams for the Higgs decay channels: (a)  $H \rightarrow f\bar{f}$  ( $f$  =fermions), (b)  $H \rightarrow WW^*/ZZ^*$ , (c)  $H \rightarrow Z\gamma/\gamma\gamma$  (W-loop), (d)  $H \rightarrow Z\gamma/\gamma\gamma$  (fermion-loop) and (e)  $H \rightarrow gg$  (quark-loop). Particles with a star (\*) represent off-shell particles.

A precise Higgs boson mass measurement of  $m_H = 125.09 \pm 0.24$  GeV was obtained by combining the data samples of the ATLAS and CMS experiments collected during 2011 and 2012 [21]. For this measurement the  $H \rightarrow \gamma\gamma$  and  $H \rightarrow ZZ^* \rightarrow 4\ell$  decay channels were used. The results are obtained from a simultaneous fit to the reconstructed Higgs boson invariant mass in the two channels and for the two experiments.

Spin and parity of the Higgs boson were also studied by ATLAS and CMS collaborations [22–24]. As part of these studies the SM spin-parity  $J^P = 0^+$  hypothesis was compared with alternative hypotheses using the Higgs boson decays  $H \rightarrow \gamma\gamma$ ,  $H \rightarrow ZZ^* \rightarrow 4\ell$  and  $H \rightarrow WW^* \rightarrow \ell^+\nu_\ell\ell^-\bar{\nu}_\ell$ , as well as the combination of these channels. All tested alternative models are excluded in favor of the  $J^P = 0^+$  hypothesis at more than 99.9% confidence level<sup>11</sup>.

## 1.4 Current status of $t\bar{t}H$ searches

The search of the production of the Higgs boson in association with a pair of top-quark is typically performed in terms of the signal strength parameter,  $\mu_{t\bar{t}H}$ , which is defined as the ratio of the observed to the expected cross-section according to the SM:

$$\mu_{t\bar{t}H} = \frac{\sigma_{t\bar{t}H}}{\sigma_{t\bar{t}H}^{SM}} \quad (1.35)$$

Table 1.3 shows the best-fit value of  $\mu_{t\bar{t}H}$  obtained by the ATLAS experiment for the  $H \rightarrow b\bar{b}$ ,  $H \rightarrow \gamma\gamma$  and multilepton ( $H \rightarrow WW^*$ ,  $H \rightarrow ZZ^*$  and  $H \rightarrow \tau^-\tau^+$ ) decay

<sup>11</sup>Note that these channels are all probing decay to bosons. The  $J^P$  could still be different in fermionic decays.

channels [5]. Different dataset periods, collected at  $\sqrt{s}=13$  TeV, were used to compute these values for each individual channel. As shown, the  $H \rightarrow \gamma\gamma$  and multilepton channels achieved equal observed significance ( $4.1\sigma$ ). However, the  $H \rightarrow \gamma\gamma$  channel includes the data collected during 2015-2017, while the multilepton channel only uses 2015-2016 data. In fact, the observed significance for  $H \rightarrow \gamma\gamma$  using only 2015-2016 data is  $0.9\sigma$  [25].

The  $H \rightarrow b\bar{b}$  channel, despite having the highest branching ratio (see Table 1.2), suffers from the large backgrounds from the production of top-quark pairs with additional QCD radiation producing  $b$ -quark pairs [26]. Furthermore, due to the presence of  $b$ -quarks from top decays, combinatorial ambiguity in the final state makes it challenging to find the two  $b$ -quarks originating from the Higgs boson in order to identify the signal events.

The table also includes the best-fit for  $\mu_{t\bar{t}H}$  combining all three channels at  $\sqrt{s}=13$  TeV. A value of  $\mu_{t\bar{t}H} = 1.32^{+0.28}_{-0.26}$  was obtained with an observed (expected) significance of  $5.8\sigma$  ( $4.9\sigma$ ). Furthermore, an observed (expected) significance of  $6.3\sigma$  ( $5.1\sigma$ ) was computed by including datasets collected with 7 and 8 TeV.

The CMS collaboration has reported a best-fit value for  $\mu_{t\bar{t}H}$  of  $1.26^{+0.31}_{-0.26}$  by combining the data collected during 2011-2017 with a center-of-mass energies of 7, 8 and 13 TeV for all Higgs decay modes [6]. The observed (expected) statistical significance for this result was 5.2 (4.2) standard deviations.

**Table 1.3:** Best fit values of  $\mu_{t\bar{t}H}$  for the  $H \rightarrow b\bar{b}$ ,  $H \rightarrow \gamma\gamma$  and multilepton channels together with the corresponding observed and expected significances. The last two rows show the combined results for these channels using the 2016-2017 datasets as well as the combination of the 2011-2012 ( $\sqrt{s}=7, 8$  TeV) and 2015-2017 datasets ( $\sqrt{s}=13$  TeV).

Analysis	Data period	$\sqrt{s}$	Best fit $\mu_{t\bar{t}H}$	Significance	
				Observed	Expected
$t\bar{t}H$ (multilepton)	2015-2016	13 TeV	$1.6^{+0.5}_{-0.4}$	$4.1\sigma$	$2.8\sigma$
$t\bar{t}H$ ( $H \rightarrow b\bar{b}$ )	2015-2016	13 TeV	$0.8^{+0.6}_{-0.6}$	$1.4\sigma$	$1.6\sigma$
$t\bar{t}H$ ( $H \rightarrow \gamma\gamma$ )	2015-2017	13 TeV	$1.4^{+0.4}_{-0.4}$	$4.1\sigma$	$3.7\sigma$
Combination	2015-2017	13 TeV	$1.32^{+0.28}_{-0.26}$	$5.8\sigma$	$4.9\sigma$
Combination	2011-2012, 2015-2017	7, 8, 13 TeV	-	$6.3\sigma$	$5.1\sigma$

More recently, by using additional data collected in 2018 with the ATLAS detector, a  $\mu_{t\bar{t}H}$  value of  $1.4 \pm 0.4(stat.) \pm 0.2(syst.)$  was obtained in the  $H \rightarrow \gamma\gamma$  channel [7]. The observed (expected) significance for this result correspond to  $5.2\sigma$  ( $4.4\sigma$ ). Similarly, the CMS experiment has obtained a  $\mu_{t\bar{t}H}$  value of  $1.38^{+0.36}_{-0.29}(stat.)^{+0.21}_{-0.11}(syst.)$  for the  $H \rightarrow \gamma\gamma$  channel by including the data collected during the 2018 campaign [8]. This result corresponds to an observed (expected) significance of  $6.6\sigma$  ( $4.7\sigma$ ).

## 1.5 Measurements of the top Yukawa coupling

The couplings of the SM Higgs boson to fermions and vector bosons are “pseudo-observables”, i.e. they cannot be directly measured. This is because each observed process involves at least two different couplings: one for the production and one for the decay mode of the Higgs. Thus, in order to study the Higgs boson couplings, the so called  $\kappa$ -framework has been used, based on the leading order contributions to each Higgs boson production and decay modes [27].

In such framework, it is assumed that the width of the Higgs boson resonance is negligible compared to the current experimental resolution. Under this assumption, the Higgs boson production and decay can be factorized, such that the cross-section of an individual channel contributing to a measured signal yield is given by:

$$\sigma(i \rightarrow H \rightarrow f) = \frac{\sigma_i \times \Gamma_f}{\Gamma_H} \quad (1.36)$$

where  $\sigma_i$  is the production cross-section through the initial state  $i$ ,  $\Gamma_f$  is the partial decay width into the final state  $f$  and  $\Gamma_H$  is the total width of the Higgs boson.

In order to probe how compatible are the leading order SM predictions of the Higgs couplings with measurements, the *coupling strength modifiers*  $\kappa_j$  ( $j$  refers to any particle to which the Higgs can couple) are used. These modifiers are defined in such a way that  $\sigma_i$  or  $\Gamma_f$  associated with the SM particle  $j$  scale with the factor  $\kappa_j^2$  when compared to the corresponding SM prediction:

$$\begin{aligned} \sigma_i &= \kappa_j^2 \cdot \sigma_i^{SM} \\ \Gamma_f &= \kappa_j^2 \cdot \Gamma_f^{SM} \\ \Gamma_H &= \kappa_H^2 \cdot \Gamma_H^{SM} \quad \left( \kappa_H^2 = \sum_j \kappa_j^2 \cdot \Gamma_j^{SM} \right) \end{aligned} \quad (1.37)$$

By definition, the best available SM predictions for all  $\sigma_i$ ,  $\Gamma_f$  or  $\Gamma_H$  are recovered when all  $\kappa_j = 1$ . These definitions rely on the assumptions that the Higgs boson can only decay to SM particles (in order to determine  $\Gamma_H$ ), and only SM particles can couple to the Higgs boson in loops, such as in the  $ggF$  or  $H \rightarrow \gamma\gamma$  case.

Furthermore, using the coupling strength modifiers, new parameters  $c_f$  and  $c_V$  ( $V$  represents either  $Z$  or  $W$  bosons) that are explicitly linearly dependent on the weak bosons and fermions masses can also be defined:

$$\begin{aligned} c_f &= \kappa_f \cdot \frac{y_f}{\sqrt{2}} = \kappa_f \cdot \frac{m_f}{v} \\ c_V &= \sqrt{\kappa_V \cdot \frac{g_V}{2v}} = \sqrt{\kappa_V} \cdot \frac{m_V}{v} \end{aligned} \quad (1.38)$$

Figure 1.6 shows the best fit values for the parameters  $c_f$  and  $c_V$  as a function of the particle mass. As shown, such linear scaling as a function of the particle masses is effectively found, indicating the compatibility of the measurements with the SM. From

this fit, the strength modifier for the top Yukawa coupling ( $\kappa_t$ ) was found to be  $1.02^{+0.11}_{-0.10}$ , consistent with the SM expectation within the 68% confidence level interval [28].

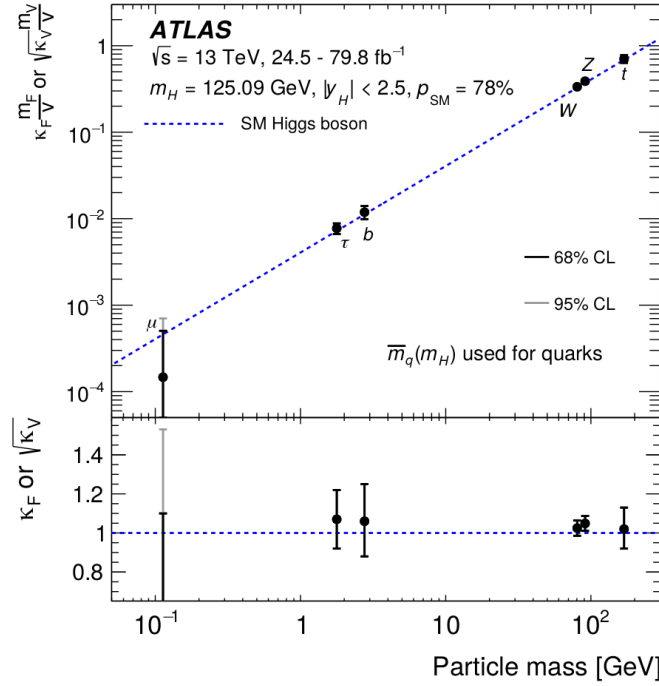


**Figure 1.6:** Best fit values of the effective coupling strength modifier parameters ( $c_f$  and  $c_V$ ) for fermions and vector bosons as a function of their masses [28]. The SM prediction for both cases is also shown (dotted blue line). The black error bars represent 68% confidence level (CL) intervals for the measured parameters. For  $\kappa_\mu$  the light error bars indicate the 95% CL interval. The lower panel shows the ratios of the values to their SM predictions.

---

## Chapter 2

# The ATLAS experiment at the Large Hadron Collider

For the physics analysis presented in this thesis, collision datasets recorded with the ATLAS (A Toroidal LHC Apparatus) detector were used [29]. ATLAS is one of the main experiments currently operating at the LHC, which is part of the *European Organization for Nuclear Research* (CERN) facility based in Geneva, Switzerland.

This chapter presents an overview of the LHC and the ATLAS detector. Section 2.1 contains a brief description of the LHC accelerator complex. Then, in Section 2.2, a summarized description of the ATLAS detector and its different sub-systems will be given.

### 2.1 LHC accelerator complex

The LHC is a synchrotron of approximately 27 kilometers of circumference designed to accelerate protons close to the speed of light<sup>1</sup>.

The LHC started operating in September of 2008 with a beam energy of 3.5 TeV and subsequently raised to 4 TeV until early 2013, which concluded the *Run 1* operations. The machine was shut down for about two years to allow for upgrades in the accelerator chain to increase the energy and rate of collisions for the *Run 2* data-taking period. It resumed operations in April of 2015 with an increased beam energy of 6.5 TeV.

Two proton beams circulate in opposite directions and cross at the center of the four experiments ATLAS, CMS [30], LHCb [31] and ALICE [32] with a center-of-mass energy of  $\sqrt{s}=13$  TeV (Run 2). In addition to protons, the LHC is also capable of colliding heavy ions (e.g. Lead) at a lower center-of-mass energies.

Protons are obtained by ionizing Hydrogen atoms in an electric field and then sent, in bunches of roughly  $1.15 \times 10^{11}$  protons, through the linear accelerator *LINAC2* (Figure 2.1), where they are accelerated up to 50 MeV. Next, the proton bunches are further

---

<sup>1</sup>Up to approximately  $0.999999991c$ , which is equivalent to a proton energy of about 7 TeV.

accelerated in sequence up to 1.4 GeV by the *BOOSTER* proton synchrotron (PSB), up to 26 GeV by the proton synchrotron (PS) and up to 450 GeV by the super proton synchrotron (SPS). Finally they are injected into the LHC ring, where they are accelerated to the final collision energies of 6.5 TeV by 16 superconducting radio frequency (RF) cavities (8 in each beam direction) with oscillating electromagnetic fields at 400 MHz.

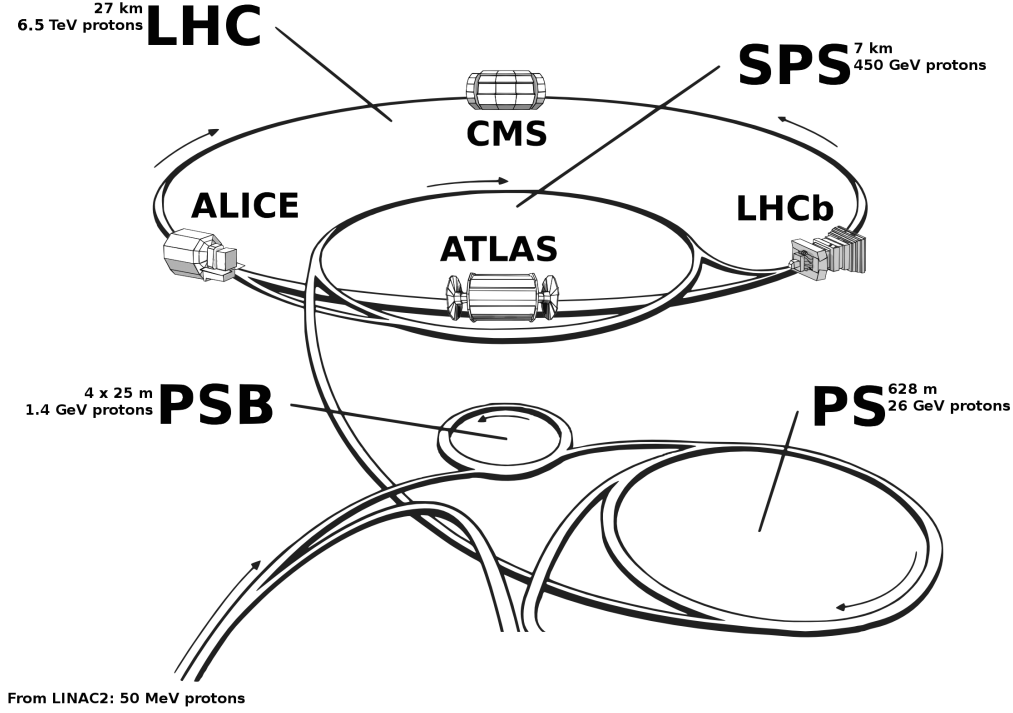


**Figure 2.1:** Schematic representation of the CERN accelerator complex showing the various stages in the proton acceleration: LINAC2, BOOSTER(PSB), PS, SPS, and the LHC.

The proton beams, each containing between 1909 and 2544 bunches (Run 2) [33], are kept in circular orbit with a revolution frequency of  $\sim 11.2$  kHz. This is achieved by means of a 7.7 T magnetic field provided by 1392 superconducting Nb-Ti dipole magnets operating at a temperature of 1.9 K. Beams are focused by 392 quadrupole magnets with strongest focusing power near the interaction points to maximize the collision rate.

### 2.1.1 Luminosity and pileup

An important parameter that characterizes the accelerator performance of the LHC is the *instantaneous luminosity* ( $L_{inst}$ ). It is defined as the ratio of the event rate ( $dN_i/dt$ ) for a given process  $i$  and its production cross-section ( $\sigma_i$ ):

$$L_{inst} = \frac{1}{\sigma_i} \cdot \frac{dN_i}{dt} \quad (2.1)$$



The instantaneous luminosity can be determined experimentally by using the parameters of the circulating beams, and the collider magnets optics. If Gaussian transverse profiles of the beams are assumed, then the following expression holds:

$$L_{inst} = \frac{n_1 n_2 n_b f_r F}{4\pi \sigma_x \sigma_y} \quad (2.2)$$

where  $n_1$  and  $n_2$  are the numbers of protons for the colliding bunches,  $n_b$  is the number of bunches in the beam,  $f_r$  is the LHC beam revolution frequency,  $F$  is a geometric correction factor related to the crossing angle of the two bunches in the interaction point (IP) and  $\sigma_x$  and  $\sigma_y$  are the horizontal and vertical Gaussian widths of the beam.

The instantaneous luminosity is expressed in units of  $cm^{-2}/s$  or  $b^{-1}/s$ <sup>†</sup>. In the 2015-2017 period,  $L_{inst}$  reached peak values between  $5 \times 10^9 b^{-1}/s$  and  $16 \times 10^9 b^{-1}/s$  [33]. When  $L_{inst}$  is integrated over a period of time, the result is proportional to the number of events contained in the data sample collected over that period:

$$N_i(T) = \varepsilon \sigma_i L(T) \quad (2.3)$$

where  $\varepsilon$  is the detection efficiency factor;  $T$  is a specific time period and  $L(T)$  is the *integrated luminosity* over that period, given by:

$$L = \int_T L_{inst} dt \quad (2.4)$$

Thus, in all the LHC experiments the integrated luminosity is used to refer to the amount of collected data over certain operation periods. This is illustrated in Figure 2.2, where the cumulative distributions of  $L$  recorded by ATLAS in the 2015-2017 period is shown. The figure shows in green color the amount of luminosity *delivered* by the LHC during stable beam conditions. The *recorded* luminosity (yellow) reflects the Data Acquisition (DAQ) inefficiency, as well as the inefficiency of the so called “warm start” (i.e., when the stable beam flag is raised and the detectors undergo a ramp-up of the high voltage). The blue distribution corresponds to the amount of data that fulfill certain quality parameters imposed by the physics analysis, which will be discussed in Section 4.1.1.

When two proton bunches collide it is likely that a large number of  $pp$  interactions occur simultaneously. Only the collision that produces the highest momentum transfer (i.e. produces particles with the highest momentum fraction from the initial protons) is of interest for the physics analysis. All the additional  $pp$  interactions that occur are referred to as *pileup*. More specifically, two types of pileup interaction can be defined: *in-time* pileup refers to additional interactions that occur within the current bunch pair crossing, while *out-of-time* pileup refers to pileup from previous or following bunches crossing.

---

<sup>†</sup>The *barn*( $b$ ) is typically used as the unit for cross-section and corresponds to  $10^{-24} cm^2$ .

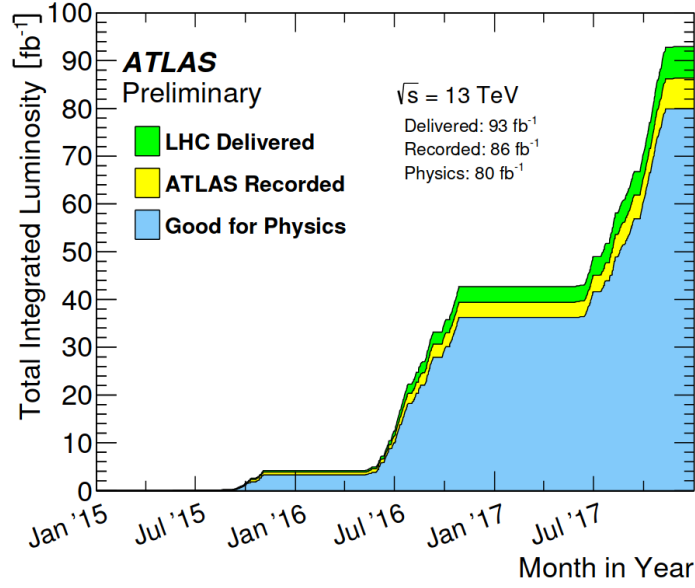


**Figure 2.2:** Time evolution of the total integrated luminosity for the data taking period 2015-2017 [34]. The plateaus represent periods of time where the LHC was not delivering luminosity. The slopes in the periods where the integrated luminosity increases is proportional to the instantaneous luminosity. Note, for example, that the instantaneous luminosity increased in 2016 and 2017 (steeper slopes) with respect to 2015.

The amount of pileup can be estimated from the mean of the Poisson distribution of the total number of interactions per bunch crossing as:

$$\mu = \frac{L_{inst} \times \sigma_{inel}}{n_b \cdot f_r} \quad (2.5)$$

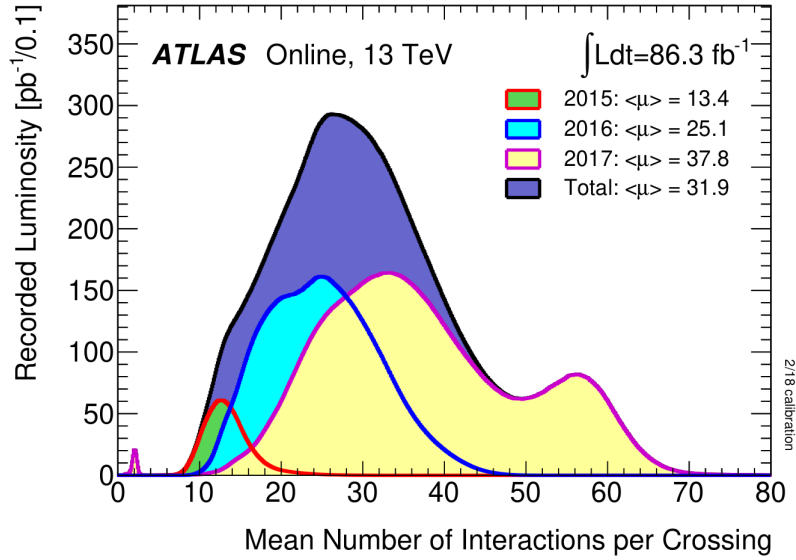
where  $\sigma_{inel}$  is the inelastic cross-section for  $pp$  interactions. For 13 TeV collisions,  $\sigma_{inel}$  is measured to be equal to about 80 mb [35].

Figure 2.3 presents the luminosity-weighted distributions of  $\mu$  for the data collected in 2015, 2016 and 2017 as well as the combined distribution for the entire 2015-2017 period. These plots show the amount of integrated luminosity that was recorded for a given value of  $\mu$ . The total (2015-2017) and per-year average pileup values are presented as well.

Due to the dependence of  $\mu$  on the instantaneous luminosity, the mean number of interactions per bunch crossing increases with instantaneous luminosity. This leads to the double peak shape of the 2017 distribution, where  $L_{inst}$  was increased towards the end of the 2017 data taking campaign.

## 2.2 The ATLAS detector

The ATLAS detector is the largest general-purpose particle detectors in the LHC ring [29]. It weighs over 7000 tons and has a cylindrical shape with a diameter of approximately 25 m and a length of 44 m (Figure 2.4). It is composed by several concentric detector sub-



**Figure 2.3:** Luminosity-weighted distribution of the mean number of interactions per crossing ( $\mu$ ) for the 2015-2017 period at 13 TeV center-of-mass energy [34]. The plot also shows the average  $\mu$  for each individual year and the combined period.

systems, which provide an almost  $4\pi$  coverage in solid angle, essential for reconstructing the energy flow in an event.

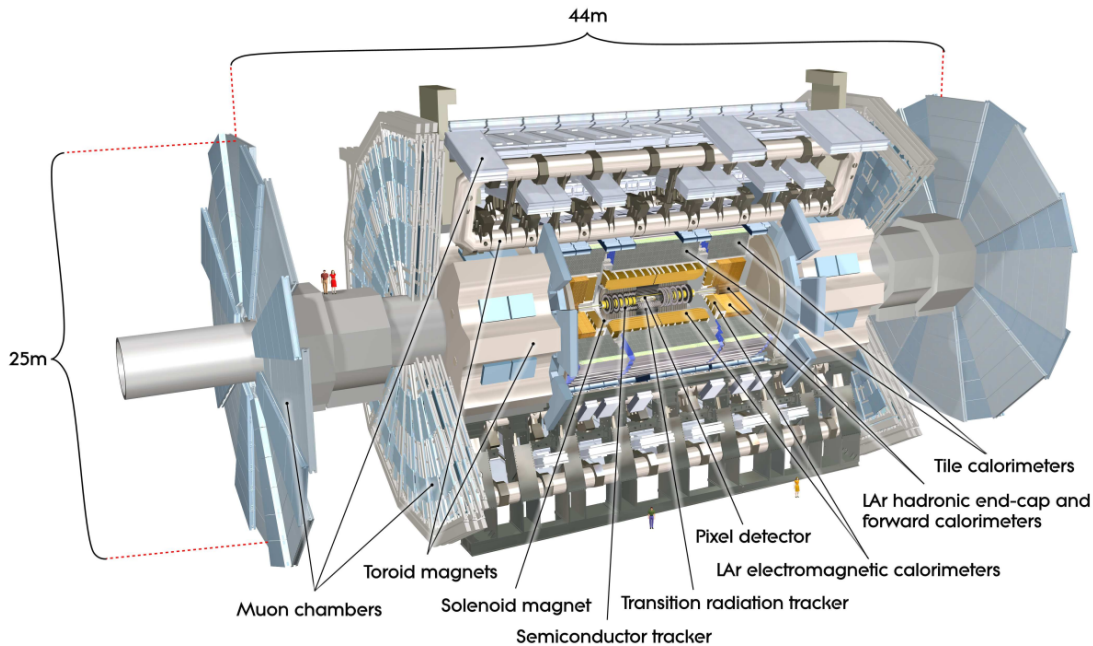


**Figure 2.4:** Sketch of the ATLAS detector showing the Magnet systems (Toroid and Solenoid magnets), the Inner Detector (Pixel, SCT, TRT), the Calorimeters (Liquid Argon and Tile calorimeters) and the Muon Detectors [29].

ATLAS uses a right-handed coordinates system with origin in the center of the detector. The beam direction defines the  $z$ -axis and thus, the  $x - y$  (transverse) plane is perpendicular to the beam direction. The positive  $x$ -axis is defined as pointing from the

IP to the center of the LHC ring and the positive  $y$ -axis is defined as pointing upwards. The azimuthal angle  $\phi$  is measured around the beam axis (in the  $x - y$  plane), and the polar angle  $\theta$  is the angle from the beam axis (in the  $y - z$  plane). Typically, the relativistic invariant quantity called *pseudo-rapidity* ( $\eta$ ) is used instead of  $\theta$ :

$$\eta \equiv -\ln \tan \left( \frac{\theta}{2} \right) \quad (2.6)$$

The transverse momentum  $p_T$  and the transverse energy  $E_T$  are defined in the  $x - y$  plane through:

$$p_T = p \cdot \sin(\theta), \quad E_T = E \cdot \sin(\theta) \quad (2.7)$$

The distance  $\Delta R$  in the  $\eta - \phi$  space is defined as:

$$\Delta R \equiv \sqrt{(\Delta\eta)^2 + (\Delta\phi)^2} \quad (2.8)$$

The different ATLAS detector sub-systems will be described in the next sections starting from the inner-most outwards.

### 2.2.1 Inner detector

The ATLAS inner detector consists of four independent detector sub-systems: the Insertable B-Layer (IBL), the Pixel detector, the Silicon microstrip tracker (SCT) and the Transition Radiation Tracker (TRT). They are arranged in different layers around the beam pipe as depicted in Figure 2.5. The Pixel and SCT are split into concentric cylindrical *barrel* modules covering the central region and disk-shaped *end-cap* modules covering the forward regions of the ID (see Figure 2.6). In addition, the entire ID is surrounded by an uniform 2 T axial magnetic field generated by a central superconducting solenoid, which is kept at temperature of 4.5 K with liquid helium. The strong magnetic field bends the trajectory of incoming charged particles, allowing accurate measurement of their momenta using the curvature radius of their tracks.

#### The IBL

The IBL is the inner-most detector of the ID and consist of 224 modules with a total of six million pixels with independent readout. Each pixel provides a spatial hit resolution of 8  $\mu\text{m}$  in the azimuthal direction and 40  $\mu\text{m}$  along the  $z$ -axis. It was added before the start of Run 2 of the LHC with the main goal of improving the tracking and vertex reconstruction [37]. It provided more precise vertex measurement and identification of jets originating from  $b$ -quarks, which greatly benefits the correct identification of jets

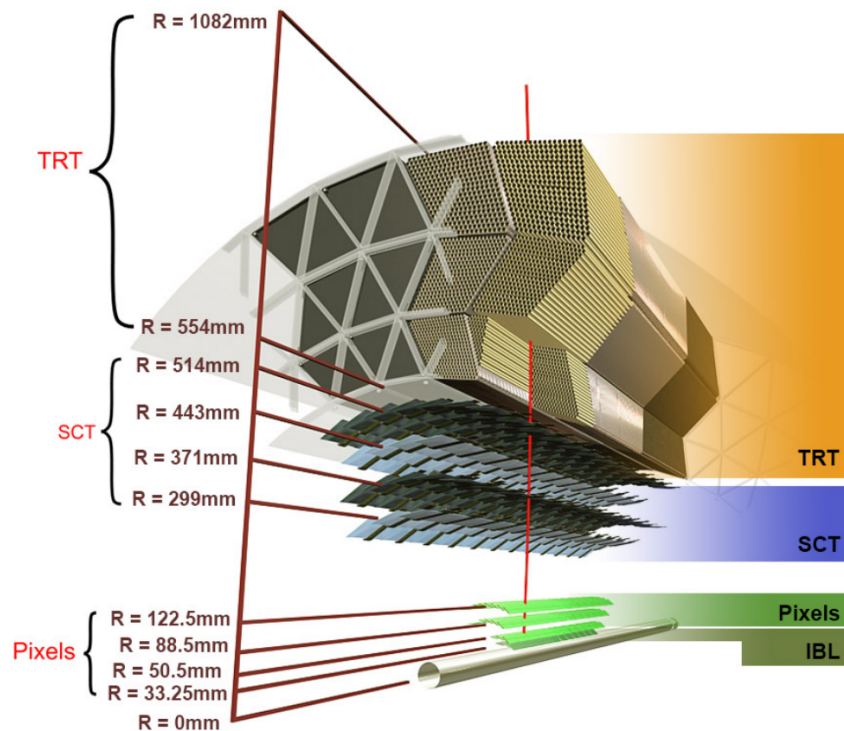


**Figure 2.5:** ATLAS inner detector in the barrel region [36].

containing  $b$ -hadrons, referred to as  $b$ -tagging. The improvement in  $b$ -tagging due to the addition of the IBL has been estimated around 10% [38].

### The Pixel detector

The Pixel detector is the next sub-system of the ID after the IBL. It consists of 3 barrel and 3 end-cap (in each of the two Pixel end-caps) layers of silicon semiconductor pixel sensors and covers up to  $|\eta| < 2.5$  in pseudo-rapidity (see Figure 2.6).

In total, the Pixel detector has 1744 modules with about 80 million pixels and the spatial hit resolution is  $\sim 10 \mu\text{m}$  in the azimuthal direction and  $\sim 115 \mu\text{m}$  along the  $z$ -axis (for the barrel) and the radial direction from the beam pipe (for the end-caps).

### The SCT

The SCT comes after the Pixel detector in the radial direction from the beam pipe and is also composed of silicon semiconductor sensors. However, instead of pixels, the SCT silicon sensors are segmented into microstrips spaced by  $80 \mu\text{m}$ . The SCT has 4 cylindrical barrel layers and 9 disks in each of the two end-caps. Similar to the Pixel detector, the SCT has limited pseudo-rapidity coverage up to  $|\eta| < 2.5$  (Figure 2.6).

The barrel and end-caps are populated with a total of 4088 two-sided modules with 768 active microstrips, which provides a spatial resolution of  $\sim 17 \mu\text{m}$  in the azimuthal

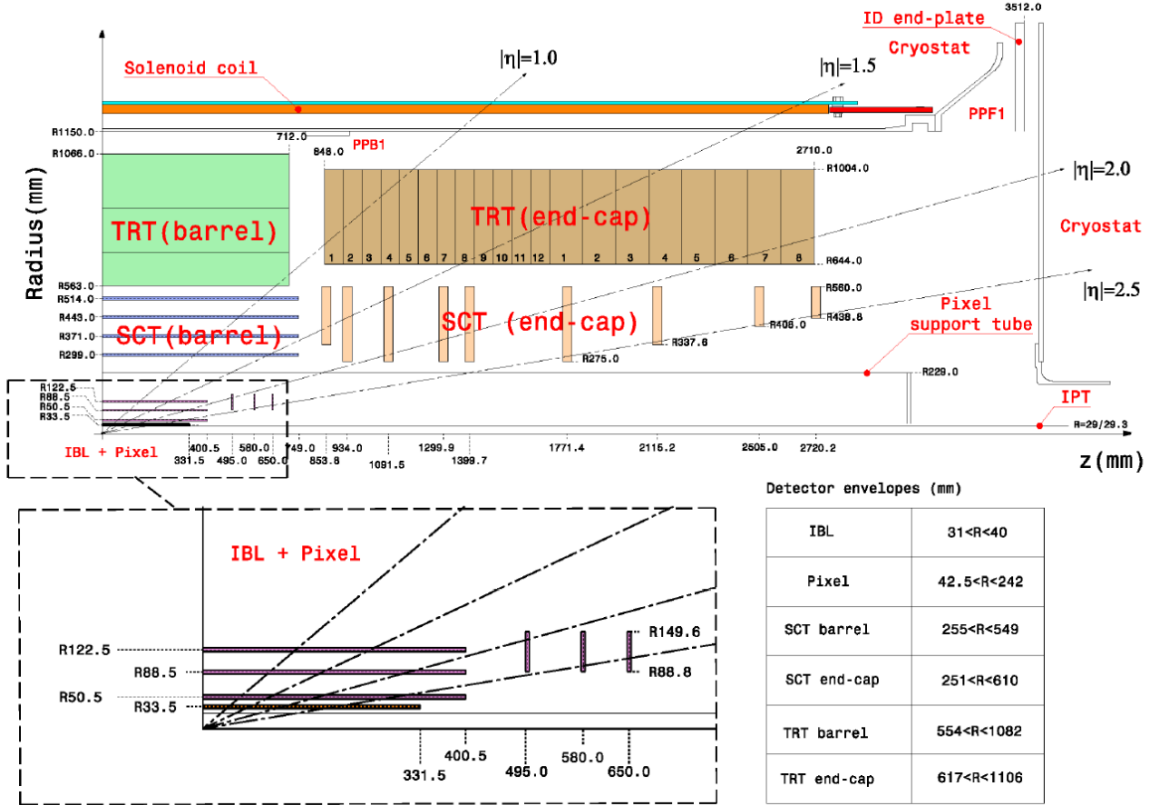


**Figure 2.6:** View of a quarter-section of the ATLAS inner detector showing each of the major detector sub-systems. [39]. As shown, the pseudo-rapidity of the ID is limited to  $|\eta| < 2.5$  due to the Pixel and SCT end-cap coverage.

direction and  $\sim 580 \mu\text{m}$  along the  $z$ -axis (for the barrel) and the radial direction from the beam pipe (for the end-caps).

## The TRT

Finally, the TRT is the outer-most detector sub-system of the ID. It is composed of straw tubes with 144 cm in length and 4 mm in diameter. The straws are filled with a gas mixture of Xe (70%),  $\text{CO}_2$  (27%) and  $\text{O}_2$  (3%). Through the center of each straw, a gold-coated wire of  $31 \mu\text{m}$  of diameter serves as anode at ground potential. The wall of the straws act as cathodes and are kept at a negative potential of approximately -1.5 kV.

When charged particles pass through the straws, they ionize the gas mixture. Then, the electrons and ions drift towards the cathode and anode respectively and produce a signal proportional to the energy deposited by the particle. Typically, about 36 straw hits are recorded by the TRT, which provides a spatial resolution of  $\sim 130 \mu\text{m}$  in the plane perpendicular to the wire. The TRT does not provide tracking information in the direction parallel to the straws ( $z$ -axis).

The TRT barrel consists of 72 layers of straw tubes and the end-cap regions consist of 160 layers, which are radially oriented on 18 wheels. The layers of straws are separated by



a polypropylene radiator which changes the refractive index of the volume and can provide discrimination between electrons and heavier charged particles, since lighter particles emit much more transition radiation.

## 2.2.2 Calorimeters

The calorimeters enclose the ID and are designed to stop the particles in order to measure their energies. This is achieved by using sampling calorimeters [40], formed by alternating layers of dense absorber material and an active medium. The dense material induces particle showers, which can be of electromagnetic or hadronic nature. After that, the showers generate a signal in the active material that is proportional to the total energy deposited.

Two types of calorimeters are used in ATLAS: Electromagnetic Calorimeter (EMCal) and Hadronic Calorimeter (HCal). They cover a pseudo-rapidity range of up to  $|\eta| = 4.9$  and are divided into barrel and end-cap<sup>2</sup> sections, as shown in Figure 2.7.

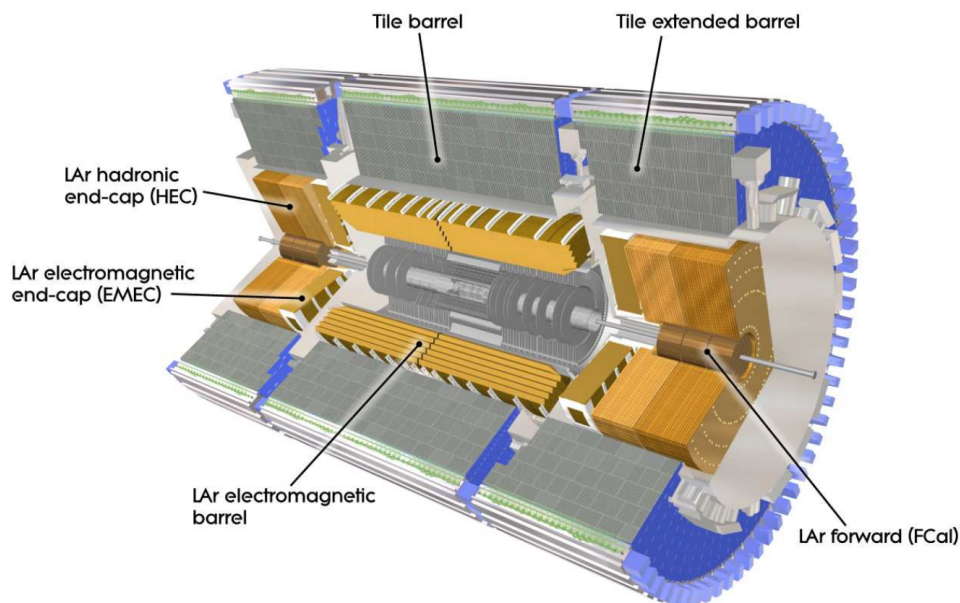


**Figure 2.7:** ATLAS calorimeter system [29].

Since the main goal is to measure the energy of the particles, calorimeters must provide good containment for electromagnetic/hadronic showers and limit *punch-through* (hadronic shower leakage) into the muon system. In the case of muons, they are expected to deposit only a small amount of energy in both calorimeters systems. Neutrinos do not interact at all with the detector and only appear as momentum imbalance inside the detector (see Section 3.4).

<sup>2</sup>In the case of the hadronic calorimeter, two “extended” barrels are used instead.

## The electromagnetic calorimeter

The EMCal is the first ATLAS calorimeter layer, just outside the solenoid magnet that surrounds the ID. It is designed to measure the energy deposited by electrons and photons by means of electromagnetic showers. These showers are characteristic of highly energetic electrons and photons, which interact with matter primarily through bremsstrahlung and  $e^-e^+$  pair production, respectively. Sufficiently energetic bremsstrahlung photons can further produce  $e^-e^+$  pairs and electrons and positrons with high momentum can create more bremsstrahlung, which continues the process leading to a cascade or shower as shown in Figure 2.8.

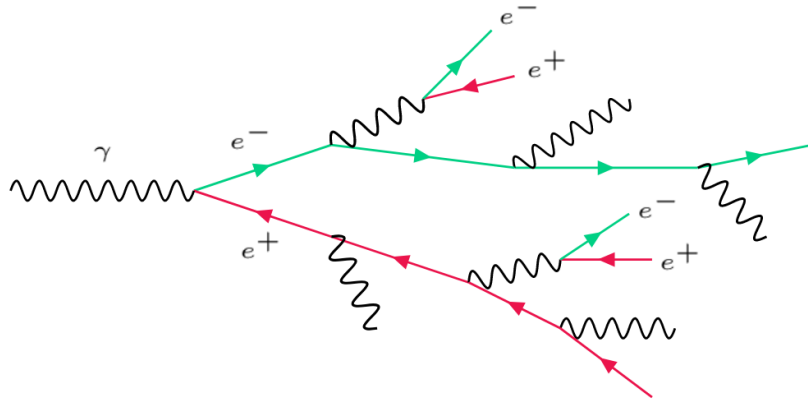


**Figure 2.8:** Example of a photon-initiated electromagnetic shower.

These two processes (pair production and bremsstrahlung) continue until the energy of the photons falls below 1.022 MeV ( $e^-e^+$  pair production threshold), and energy losses of electrons due to ionization start to dominate instead. Since muons have much higher mass than electrons, they do not produce much bremsstrahlung. Therefore, they can pass through the EMCal losing only a small amount of their energy (mainly due to ionization). The same happens to sufficiently energetic charged hadrons.

The electromagnetic showers are characterized by a parameter called *radiation length* ( $X_0$ ), which is defined as the mean distance over which an electron loses all but  $1/e^\dagger$  of its energy by bremsstrahlung or, in the case of photons,  $7/9$  of the mean free path for pair production. The radiation length depends on the atomic number of the media through which the electron or photon traverses. The higher the atomic number (heavier elements) the shorter  $X_0$  will be. Therefore, heavy materials are typically used as absorber media. In the case of the ATLAS EMCal, Lead is used. Consequently, the thickness of the EMCal varies between 22 and 33  $X_0$ , which ensures good containment of the electromagnetic cascades.

The EMCal uses liquid argon (LAr) as active medium, which is characterized by excellent radiation hardness and energy resolution. The electrodes are capton-plated copper

<sup>†</sup>Here  $e$  represents the Euler number, not the electron charge.





$15 \leq E_{electrons} \leq 180$  GeV, the reconstructed energy response was found to be linear within  $\pm 0.1\%$ .

## The hadronic calorimeter

The ATLAS HCal encloses the EMCal and it is designed to measure the energy deposited by hadrons such as pions, kaons and neutrons. The strong interaction of hadrons in the HCal absorber material produces hadronic showers. These hadronic showers caused by nuclear interactions are characterized by a parameter known as *nuclear interaction length* ( $\lambda_{int}$ ). It represents the mean distance traveled by a hadron before undergoing an inelastic nuclear interaction and is given by:

$$\lambda_{int} = \frac{A}{N_A \cdot \sigma_{int}} \quad (2.10)$$

where  $A$  is the atomic mass of the absorber material,  $N_A$  is the Avogadro number and  $\sigma_{int}$  is the total nuclear interaction cross-section.

The ATLAS HCal system is divided into three parts: the Tile (*barrel* and *extended barrel*) Hadronic Calorimeter (TileCal), the LAr Hadronic End-cap Calorimeter (HEC), and the LAr Forward Calorimeter (FCal), as shown in Figure 2.7:

**TileCal:** The TileCal uses steel as the absorber and scintillating tiles as the active material. It is placed directly outside the EMCal with inner radius of 2.28 m and an outer radius of 4.25 m. Its barrel portion covers the region  $|\eta| < 1.0$  and its two extended barrels cover the range  $0.8 < |\eta| < 1.7$ . Both are segmented in depth in three layers with approximately 1.5, 4.1 and 1.8  $\lambda_{int}$  thick for the barrel and 1.5, 2.6, and 3.3  $\lambda_{int}$  for the extended barrel. The total detector thickness at the outer edge of the tile-instrumented region is 9.7  $\lambda_{int}$  at  $|\eta| = 0$ .

**HEC:** The HEC uses the same active material as the EMCal: LAr. However, the absorber material is Copper, instead of Lead. It consists of two independent wheels per end-cap, located directly behind the end-cap EMCal. Each wheel is divided into two segments in depth, for a total of four layers per end-cap. The pseudo-rapidity coverage lies in the range  $1.5 < |\eta| < 3.2$ . The average thickness of the HEC is 10  $\lambda_{int}$ .

**FCal:** The FCal consists of three modules in each of the two end-caps: the first, uses Copper as absorber material and is optimized for electromagnetic measurements, while the other two, use tungsten and measure predominantly the energy of hadronic interactions. All three use LAr as active material. The FCal is approximately 10  $\lambda_{int}$  deep and covers up to  $|\eta| = 4.9$ .

The granularity of the HCal is coarser than for the EMCal, in the order of  $\Delta\eta \times \Delta\phi = 0.1 \times 0.1$  for  $|\eta| < 2.5$ . Additionally, its energy resolution, measured in test beams, ranges from less than 14% for pions with  $p_T = 20$  GeV to less than 7% for pions with  $p_T > 180$  GeV [42]. This resolution is parameterized as a function of energy in a similar way as the EMCal (see Eq. 2.9).

### 2.2.3 Muon spectrometer

For the analysis presented in this thesis, the correct identification of muons is of paramount importance, since they are part of the  $t\bar{t}H$  signature. Muons are characterized for producing low ionization losses in the calorimeter system as they traverse its entire volume. The Muon Spectrometer (MS) is, therefore, the outer-most detector sub-system of ATLAS and is designed to measure the muon momentum. It provides a relative momentum resolution better than 3% over a wide  $p_T$  range and up to 10% at  $p_T = 1$  TeV [43]. The MS is also designed to offer trigger capabilities for the ATLAS data acquisition system.

The MS consists of three concentric cylinders in the barrel region around the beam axis at radii of approximately 5 m, 7.5 m, and 10 m. In the two end-cap regions, the muon chambers form four wheels perpendicular to the  $z$ -axis and located at distances of  $|z| \sim 7.4$  m, 10.8 m, 14 m, and 21.5 m from the interaction point. The total pseudo-rapidity coverage of the MS is  $|\eta| < 2.7$ . In the center of the detector ( $|\eta| = 0$ ), a gap has been left open to allow for services to the solenoid magnet, the calorimeters and the ID. Figure 2.10 shows a schematic representation of the MS.

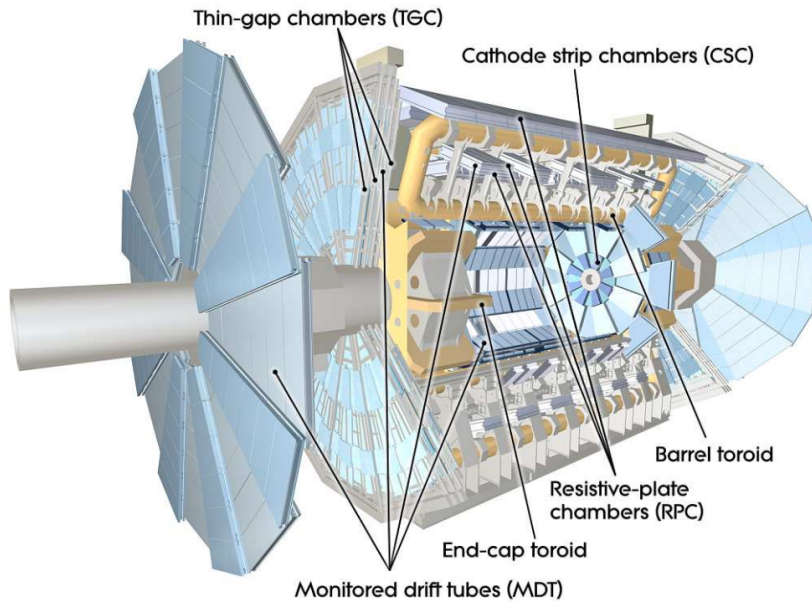


**Figure 2.10:** Cut-away view of the ATLAS muon system [29].

The precision momentum measurement of muons is performed by the so called Monitored Drift Tube (MDT) chambers, which cover the  $|\eta| < 2.7$  range, except for the

inner-most end-cap layer, where the coverage is limited to  $2.0 < |\eta| < 2.7$ . The MDTs consist of three to eight layers of drift tubes with an average resolution of  $80 \mu\text{m}$  per tube, or about  $35 \mu\text{m}$  per chamber. The momentum measurements are possible due to the magnetic field created by air-core superconducting toroid magnets that generate a magnetic field between 0.5 and 1 T. This field bends the muon trajectories in the  $\phi - z$  plane (see Figure 2.11).

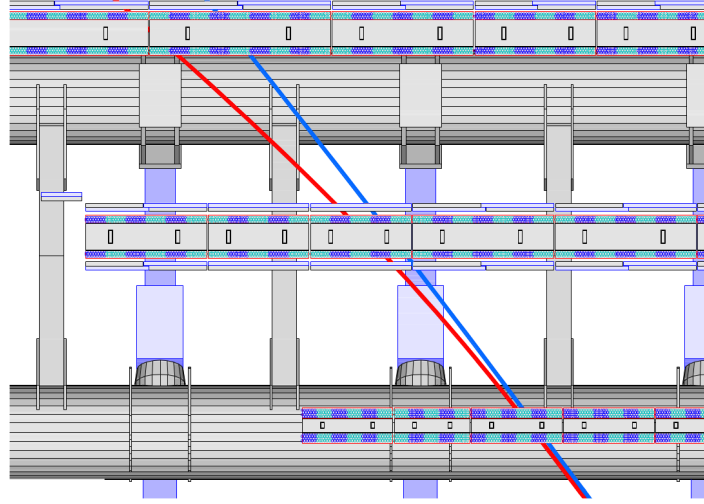


**Figure 2.11:** Illustration of a 4 GeV (red) and a 20 GeV (blue) muon track traversing the barrel region of the MS [29]. The image shows a view of a quarter-section of the ATLAS MS in which the air-core superconducting toroid magnet bends the muon track in the  $\phi - z$  plane.

In the  $2.0 < |\eta| < 2.7$  region, Cathode-Strip Chambers (CSC) are used in the inner-most layer due to their higher event rate capability and time resolution. The CSCs consist of multiwire proportional chambers (MPC) with cathode planes segmented into strips in orthogonal directions. The CSC spatial resolution is about  $40 \mu\text{m}$  in the bending plane ( $\phi - z$ ) and about 5 mm in the transverse plane ( $x - y$ )<sup>†</sup>.

Additionally, the MS was designed to have independent trigger capabilities in the  $|\eta| < 2.4$  range. This is achieved by using fast-response chambers capable of delivering track information within a few tens of nanoseconds after the passage of the muon. In the region of  $|\eta| < 1.05$ , Resistive Plate Chambers (RPC) [44] are used for this purpose, while in the  $1.05 < |\eta| < 2.4$  region, Thin Gap Chambers (TGC) [45] were chosen.

## 2.2.4 Trigger system

Due to the high luminosity of the LHC, a large collision rate is produced. However, it is not possible to record all of them due to limitations on the rates that the read-out system is able to handle. Thus, a trigger system is implemented in order to reduce the

<sup>†</sup>The difference in resolution between the bending and non-bending planes is due to the different readout pitch, and to the fact that the azimuthal readout runs parallel to the anode wires.

event acceptance to a manageable amount and be able to record only the most interesting events after a series of increasingly strict selection criteria [46]. The ATLAS trigger system consists on two sequential algorithms called *Level 1* (L1) trigger and *High Level Trigger* (HLT).

The L1 trigger is a hardware-based system that uses coarse information from the calorimeters and the MS to select events of interest. The algorithms search for physics objects like electrons, muons, jets and hadronically decaying tau leptons and apply certain selection criteria, which includes  $E_T$  and  $p_T$  thresholds and particle multiplicities. With this trigger, event recording rates of approximately 1 kHz (from collision rates of  $\sim 40$  MHz) are achieved.

The L1 trigger is followed by the HLT, which is a software-based trigger that uses input from all detector sub-systems and full calorimeter granularity. The HLT utilizes multivariate analysis techniques to further decrease the event rates below 1.5 kHz. Recorded events are checked for data quality and those that recorded during periods of sub-detector malfunction are flagged for removal from analysis.



---

## Chapter 3

# Objects reconstruction and identification

In this chapter, details about the reconstruction and identification of the physics objects used in this thesis is presented.

Charged particle tracks constitute a key ingredient in the reconstruction of other physics objects such as leptons and jets. Since the identification of tracks is the step previous to the reconstruction of these objects, a brief description of this process is presented separately in Section 3.1. Then, the reconstruction and identification of electrons and muons is described in Section 3.2, which includes a dedicated discussion about the sources of fake and non-prompt<sup>1</sup> leptons. The jet reconstruction process is presented in Section 3.3 and the determination of the missing transverse energy ( $E_T^{miss}$ ) is discussed in Section 3.4. Finally, the procedure to resolve possible ambiguities in the object reconstruction process is presented in Section 3.5.

### 3.1 Tracks and primary vertex

The tracking algorithms discussed in this section are based on information provided by the ID [47, 48]. For the particular case of muons, track information from the ID and MS is combined, which will be discussed in more detail in Section 3.2.2.

Due to the presence of an axial magnetic field, charged particles that traverse the ID will have trajectories that are bent forming helices. As they interact with the different layers of the ID, they generate *hits* in the detector modules. Tracks are a combination of these hits that are found to best describe a candidate charged particle trajectory.

The track reconstruction begins with the assembly of hit clusters. This is done by adding together adjacent pixel (or strip) hits, in a given sensor, where the energy deposited by the traversing particle yields a charge above certain threshold. Once all the clusters are

---

<sup>1</sup>Non-prompt leptons are characterized by not being originated from the hard interaction.

constructed, track seeds are formed from sets of three clusters. Then, a pattern recognition algorithm (Kalman filter [49]) is used to build track candidates from the seeds. This is done by incorporating additional clusters from the remaining layers of the ID that are compatible with the predicted trajectory of the particle. The filter creates multiple track candidates per seed if more than one compatible cluster extension exists on the same layer. Furthermore, some track candidates may be reconstructed with overlapping or incorrectly assigned clusters. Therefore, an ambiguity-solving stage is applied. Finally, the track candidates undergo a high-resolution global  $\chi^2$  fit [50], allowing for additional energy loss when the standard track fit fails.

In the ID, five parameters are used to fully describe the tracks:  $\{d_0, z_0, \phi, \theta, q/|\vec{p}|\}$ . The first four are represented geometrically in Figure 3.1. The parameters  $d_0$  and  $z_0$  correspond to the track impact parameters in the transverse and longitudinal planes respectively;  $\phi$  and  $\theta$  represent the azimuthal and polar angles respectively, and  $q/|\vec{p}|$  is the electric charge of the particle divided by its momentum. The impact parameters are defined with respect to the primary vertex (PV) in the event.

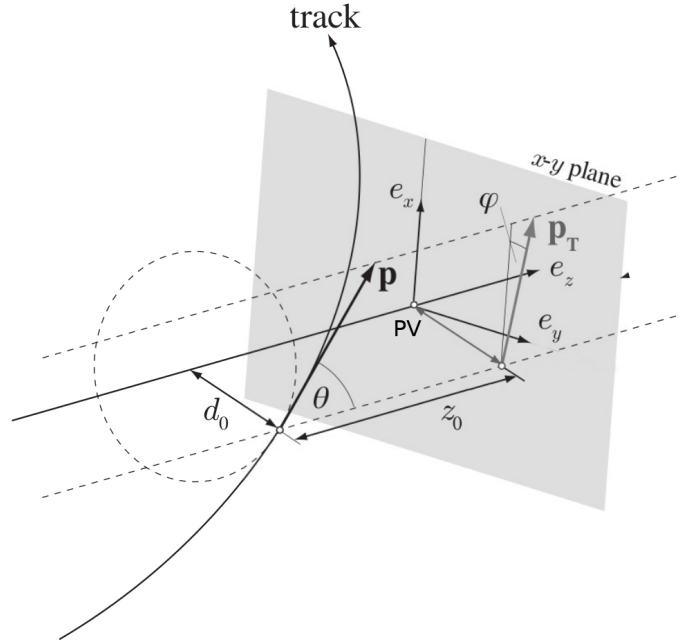


**Figure 3.1:** Illustration of the parameters used to describe a track with momentum  $\vec{p}$  in the ATLAS inner detector. The parameters  $d_0$  and  $z_0$  are defined with respect to the primary vertex (PV).

The PV is defined as the interaction vertex with the highest value of the sum of transverse momentum squared of its associated tracks ( $\sum_{trk} p_{T,trk}^2$ ). Only vertices that contain at least two tracks with  $p_T > 400$  MeV are considered as PV candidates. An example is shown in Figure 3.2, corresponding to a display of a  $Z \rightarrow \mu^- \mu^+$  candidate event recorded with the ATLAS detector at  $\sqrt{s} = 13$  TeV with 65 reconstructed pileup vertices. In this case, the PV contains the two muon tracks (yellow lines), which have the



highest  $p_T$  of all the tracks in the PV (61.5 GeV and 60 GeV). Tracks with lower  $p_T$  are represented in the image by light blue lines.

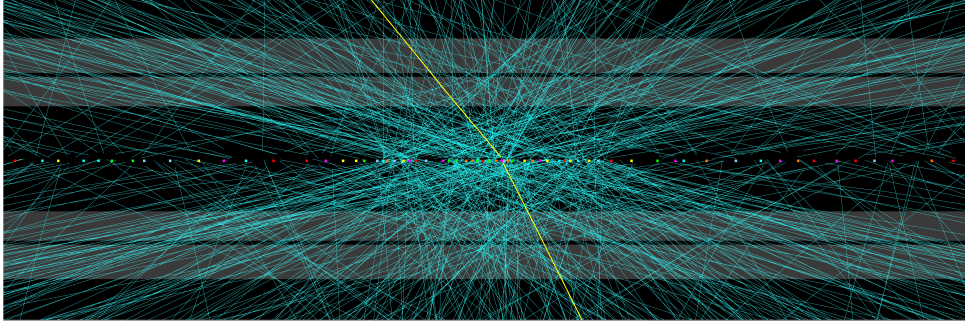


**Figure 3.2:** A display of a  $Z \rightarrow \mu^- \mu^+$  candidate event from proton-proton collisions recorded by ATLAS with LHC stable beams at  $\sqrt{s} = 13$  TeV [51]. The event contains 65 reconstructed pileup vertices. The selected PV includes the two muon tracks with  $p_T$  of 61.5 GeV and 60 GeV, which are represented by yellow lines. Light blue lines represent lower  $p_T$  tracks.

## 3.2 Leptons

The term *leptons* will be used throughout this thesis to refer only to electrons and muons. Likewise, the term *electron* will be used hereafter to refer to both electrons and positrons, unless a necessary distinction must be made between them.

### 3.2.1 Electrons

Electrons are reconstructed in the pseudorapidity region  $|\eta| < 2.5$  excluding the transition region between the barrel and the end-cap parts of the EMCal ( $1.37 < |\eta| < 1.52$ ), where there is a large amount of inactive material (cables, cooling pipes, etc). The reconstruction process exploits the main characteristic of the electron signature in the detector: localized cluster of energy deposits in the EMCal that matches to a charged particle track identified in the inner tracker system. Figure 3.3 shows a schematic illustration of the elements that conform the electron reconstruction and identification process. A typical electron candidate usually produces 12 hits in the inner tracker system: one in the IBL layer, three in the silicon pixel layers and eight in the SCT (4 double-sided silicon strips layers). In addition, approximately 35 straw hits are produced in the TRT system (for electrons with  $p_T^{track} > 500$  MeV). After that, the electron enters the EMCal, where most of its energy is collected in the second layer.

The first reconstruction step consists in building the EMCal clusters. For that purpose the  $\eta - \phi$  space is divided into small elements of dimensions  $\Delta\eta \times \Delta\phi = 0.025 \times 0.025$  called *towers*. The total energy per tower is determined by adding the energy deposited in the pre-sampler (only for  $|\eta| < 1.8$ ), first, second and third layers of the EMCal.

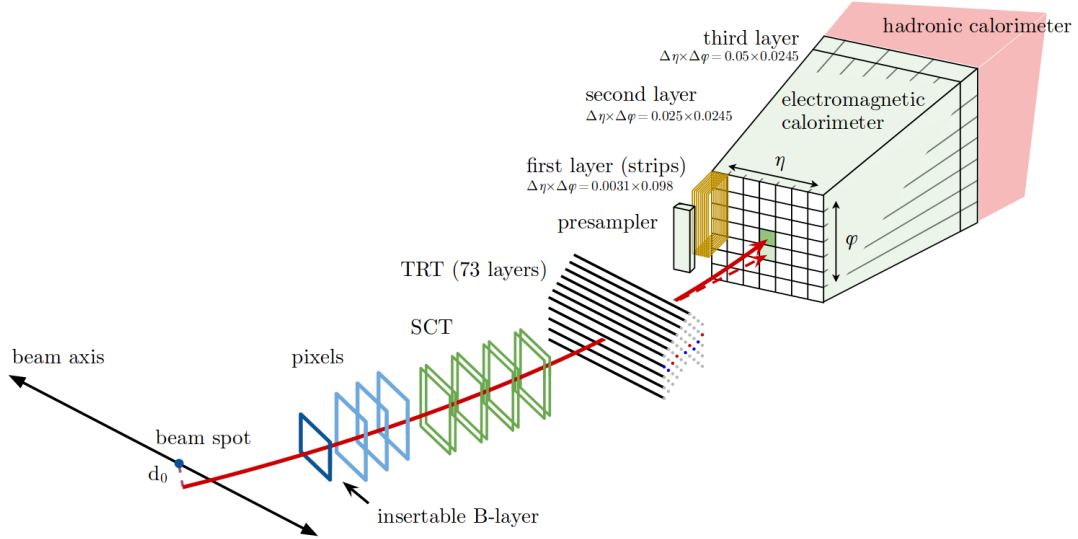


**Figure 3.3:** Illustration showing the path of an electron through the detector [52]. The red (solid) line represents the hypothetical trajectory of the electron. The red (dashed) line represents the trajectory of a bremsstrahlung photon produced in the tracking system material.

Energy cluster candidates are then seeded from localized energy deposits using a sliding-window algorithm [53]. With this method, the energy in a window of size  $3 \times 5$  towers is collected while the window moves in the  $\eta$  or  $\phi$  directions in steps of 0.025. The window energy is collected at each step until the entire  $\eta - \phi$  space is covered. A cluster candidate is selected if the sum of the transverse energy ( $E_T$ ) of the towers in a given window is a local maximum and is greater than 2.5 GeV. This threshold was chosen to optimize the reconstruction efficiency while minimizing the contribution from electronic or pileup noise.

If two candidate clusters overlap within an area of  $\Delta\eta \times \Delta\phi = 5 \times 9$  and their total  $E_T$  differs by more than 10%, then the cluster with the higher total  $E_T$  is kept. If the  $E_T$  differs in less than 10%, then the candidate containing the central tower with highest  $E_T$  is retained. Overall, the cluster algorithm has a reconstruction efficiency that ranges from 65% for  $E_T = 4.5$  GeV to 96% at  $E_T = 7$  GeV and more than 99% for  $E_T > 15$  GeV.

After the candidate clusters are defined, it is necessary to match them to tracks reconstructed in the inner detector as described in Section 3.1. The matching is done by extrapolating candidate tracks to the second layer of the EMCal and requiring that the distance (in the  $\eta - \phi$  plane) between the cluster barycenter and the extrapolated track satisfies the following conditions:  $|\Delta\eta| < 0.05$  and  $-0.1 < \Delta\phi < 0.05$ . The asymmetric condition for the matching in  $\phi$  mitigates the effects of energy loss due to bremsstrahlung where tracks with negative (positive) electric charge bend due to the magnetic field in the positive (negative)  $\phi$  direction.

If more than one track can be matched to a particular electromagnetic calorimeter cluster, then a *primary* electron track must be selected. This is done by an algorithm

that takes into account the  $\eta - \phi$  distance between the extrapolated tracks and the cluster barycenter (measured in the second layer of the electromagnetic calorimeter), the number of hits in the silicon detectors and the number of hits in the innermost silicon layers. If the matched or primary track is associated with a secondary vertex and has no pixel hits, the object is classified as a photon candidate (most likely photon conversion). However, if the primary track has at least four hits in the silicon layers and is not associated with a photon conversion, then the reconstructed object is considered an electron candidate.

As the final reconstruction step, the clusters from electron candidates are enlarged by extending the window size around the original cluster to  $3 \times 7$  towers in the barrel region ( $|\eta| < 1.37$ ) and  $5 \times 5$  towers in the end-cap ( $1.52 < |\eta| < 2.5$ ). In the transition region ( $1.37 < |\eta| < 1.52$ ), a method using both elements of extended-window sizes is used.

The electron reconstruction efficiency is calculated using tag-and-probe method in  $Z \rightarrow e^-e^+$  events from data, as described in Ref. [52]. The tag-and-probe method is a data-driven technique that uses well known resonances like  $Z \rightarrow e^-e^+$  and  $J/\Psi \rightarrow e^-e^+$  as a source of electron-positron pairs. It consists in selecting one of the electrons in the pair with tight requirements (*tag*) and then use the other (loosely selected) electron as the *probe* for the reconstruction efficiency. The tag/probe electron pair is required to have an invariant mass close to the  $Z$  boson or  $J/\Psi$  meson mass.

Figure 3.4 shows the reconstruction efficiency of electron candidates as a function of  $E_T$ . For transverse energies in the range 20 – 80 GeV the reconstruction efficiency is between 97% and 99%. This decrease is driven by cluster reconstruction inefficiencies at relatively low- $E_T$ . For higher  $E_T$ , the efficiency is found slightly above 99%.

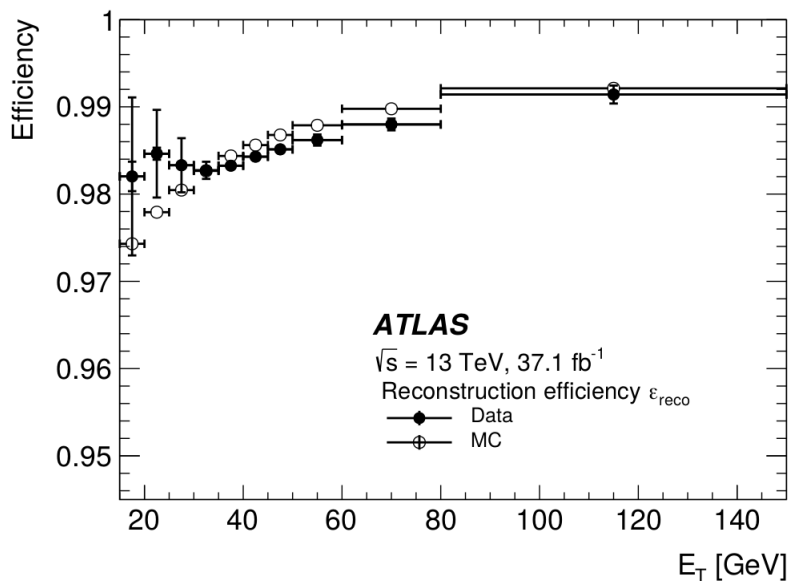


**Figure 3.4:** Electron reconstruction efficiency as a function of the  $E_T$  for  $Z \rightarrow e^-e^+$  events in data (closed circles) and simulations (open circles) [52].

After the reconstruction step, the electron identification is performed using a likelihood-based approach as described in Ref. [52]. From this method, several electron identification working points (WP) of decreasing efficiency are defined (i.e., as the identification requirements of each WP get more restrictive, the efficiency decreases). These WPs are constructed in such a way that electrons satisfying the requirements for a given WP also satisfy looser WP requirements.

Similar to the reconstruction efficiency determination, the electron identification efficiency is extracted using tag-and-probe method with  $Z \rightarrow e^-e^+$  and  $J/\Psi \rightarrow e^-e^+$  events from data. Only electron candidates reconstructed according to the criteria discussed in previous paragraphs are used for the identification efficiency determination. Figure 3.5 shows the electron identification efficiencies extracted from data (2015-2017 period) as a function of  $E_T$  and  $\eta$  for three different working points. The discontinuity at 15 GeV in the efficiency curve as a function of  $E_T$  (Figure 3.5–left) is caused by a known mis-modeling of the variables used in the estimation method of these efficiencies at low- $E_T$  [54].

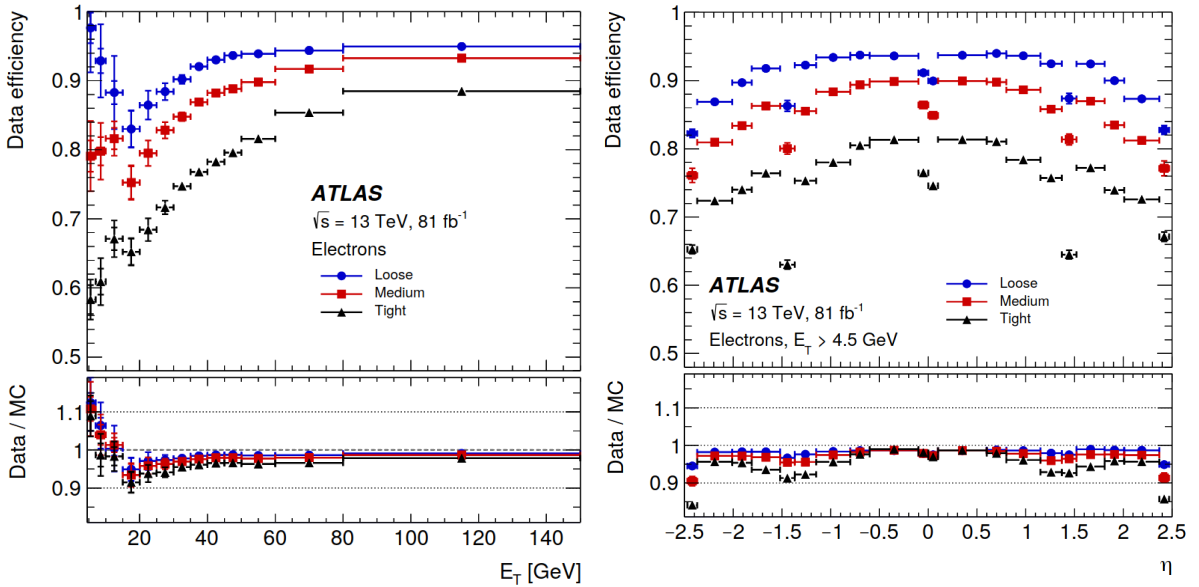


**Figure 3.5:** Electron identification efficiencies extracted from data using tag-and-probe method in  $Z \rightarrow e^-e^+$  events for Loose, Medium and Tight working points as a function of the electron  $E_T$  (left) and  $\eta$  (right) [54]. The bottom panel in each plot shows the efficiency ratio of data to simulation. For this thesis, the Tight working point is used.

Additionally, the identification efficiency shows lower values around  $1.37 < |\eta| < 1.52$  and  $|\eta| = 0$  (Figure 3.5–right). These regions correspond to the barrel/end-cap calorimeter transition and the central services gap, where reduced detector performance is expected.

For electrons produced in the hard interaction, little activity is expected in either the inner detector or the calorimeter system in a  $\Delta\phi \times \Delta\eta$  area surrounding them. Therefore, *isolation* requirements are used to identify them.

The amount of additional activity surrounding the electron is quantified by the sum of the transverse energy of calorimeter clusters or transverse momentum of tracks inside a cone of radius  $\Delta R = \sqrt{\Delta\phi^2 + \Delta\eta^2}$ , excluding the contribution of the electron itself. Using these two quantities, several “isolation working points” can be defined according to Ref. [52].

The isolation efficiency, similar to the reconstruction and identification efficiencies, is calculated using the tag-and-probe method in  $Z \rightarrow e^-e^+$  and  $J/\Psi \rightarrow e^-e^+$  events from data. Only electron candidates that pass the reconstruction and identification (for a given working point) requirements are used for the isolation efficiency determination. Figure 3.6 shows the isolation efficiency measured in data for different isolation working points as a function of the electron  $E_T$  (left) and  $\eta$  (right). As shown, the isolation efficiency does not show strong dependence of  $|\eta|$ , while its  $E_T$  dependence shows a drop for  $E_T < 25$  GeV. This is driven by the decrease in tracking efficiency at low- $E_T$ .

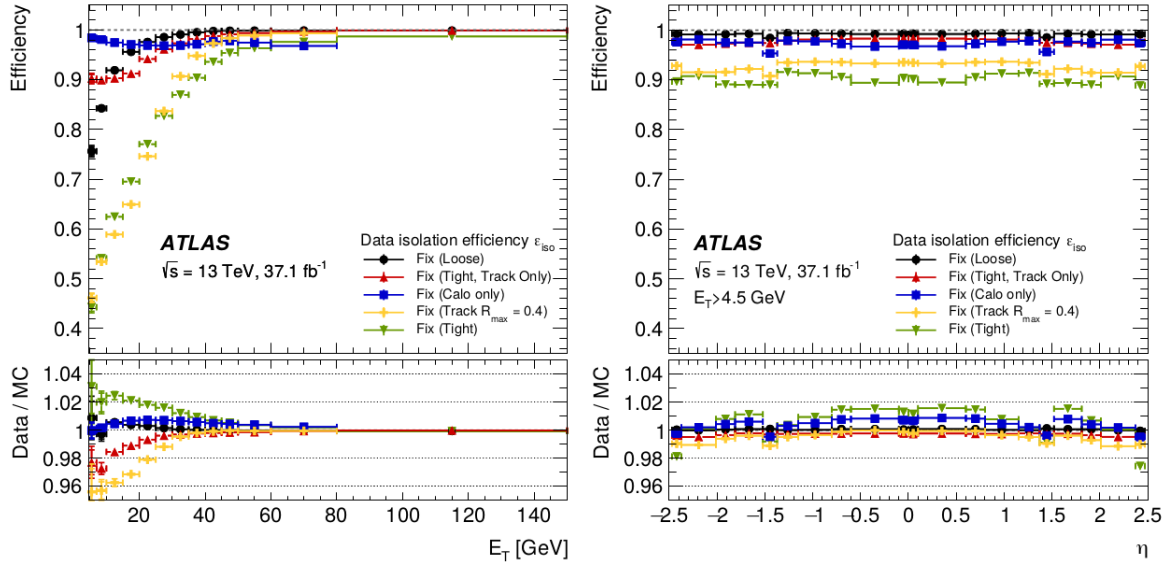


**Figure 3.6:** Electron isolation efficiencies extracted from data using tag-and-probe method in  $Z \rightarrow e^-e^+$  events for Fixed cut working points as a function of the electron  $E_T$  (left) and  $\eta$  (right) [52]. For this thesis, the *Fix(Loose)* working point is used. The bottom panel in each plot shows the efficiency ratio of data to simulation.

The electron energy scale and resolution are calibrated based on studies of EMCal energy deposits in  $Z \rightarrow e^-e^+$  and  $J/\Psi \rightarrow e^-e^+$  events [55]. The overall calorimeter energy scale is set from a large sample of  $Z \rightarrow e^-e^+$  events, comparing the invariant mass distribution in data and simulation. Differences between data and simulation are used to extract scale factors in order to correct the electrons energy scale in other simulated samples. The accuracy of the energy scale measurement varies from 0.03% to 0.2% depending on  $|\eta|$ . The calibrated energy resolution in data is less than 1% in the barrel calorimeter and typically 1-2% in the end-cap calorimeter.

### 3.2.2 Muons

Muons are reconstructed by combining information from the muon spectrometer and inner detector, supplemented in some cases by calorimeter information [56].

In the inner detector, the muon tracks are reconstructed as described in Section 3.1. The expected number of hits in each inner detector subsystem will be similar to what was described in Section 3.2.1 for electrons, except that muons will have, on average, less hits in the TRT due to their higher mass.

In the muon spectrometer, the muon reconstruction begins with a hit pattern search in each muon chamber to form track *segments*. Depending on  $|\eta|$ , each chamber provides between six and eight hits per segment. In the MDT chambers, a Hough transform [57] is used to search for hits aligned on a trajectory in the bending plane of the detector. Track segments in the MDT chambers are then reconstructed by performing a fit of the hits found in each layer. The RPC or TGC hits are used to determine the coordinate orthogonal to the bending plane. Segments in the CSC detectors are reconstructed using a separate combinatorial search in the  $\eta - \phi$  plane. Finally, muon tracks are built by fitting together hits from track segments in different layers. At least two matching track segments are necessary to build a muon track, except in the barrel-endcap transition region where a single high-quality segment is sufficient.

The combination of inner detector and muon spectrometer information for the muon track reconstruction is done in different ways depending on the specific analysis needs. In this thesis, the so called *Combined Muons* (CB)<sup>2</sup> are used. Combined muons are reconstructed using an outside-in pattern recognition algorithm, in which the muons are first reconstructed in the MS and then extrapolated inward and matched to an ID track. Then, a global fit is performed on hits from both detector subsystems to obtain the CB muon tracks. To guarantee a robust momentum measurement, additional requirements on the number of hits in the inner detector and muon spectrometer are used: at least one Pixel hit, at least five SCT hits, fewer than three Pixel or SCT holes and at least 10% of the TRT hits (for  $0.1 < |\eta| < 1.9$ ) originally assigned to the track are included in the fit.

The muon identification is done by applying quality requirements on the muon candidate tracks in order to reduce background from non-prompt muons while maintaining high identification efficiency for prompt muons.

For non-prompt muons that originate from an in-flight decay of charged hadrons, the reconstructed track candidate in the inner detector presents a distinctive "kink" in its shape. As a consequence, a poor quality in the inner detector track fit is expected. For this reason, the muon momentum measured from the track curvature in the inner detector may not match the muon spectrometer momentum measurement. These characteristics

---

<sup>2</sup>Other muon types include: *Segment-Tagged* (ST), *Calorimeter-Tagged* (CT) and *Extrapolated* (ME).



are exploited in order to identify non-prompt muons through several quantities that are sensitive to them (such as the normalized  $\chi^2$  of the combined track fit). By analogy with the electron identification process, several muon identification working points of decreasing efficiency are defined from these quantities and additional MS track quality requirements according to Ref. [56].

The reconstruction efficiency for CB muons is measured using the tag-and-probe method in data and simulated events of  $Z \rightarrow \mu^- \mu^+$  (for  $p_T^\mu > 15$  GeV) and  $J/\Psi \rightarrow \mu^- \mu^+$  (for  $5 \text{ GeV} < p_T^\mu < 20 \text{ GeV}$ ). Muons from all identification working points are correctly reconstructed with efficiencies that are higher than 98% and independent of the muon  $p_T$  within 2% [56]. As an example, Figure 3.7 shows the reconstruction efficiency of muons identified with a *Medium* working point as a function of  $p_T^\mu$ .

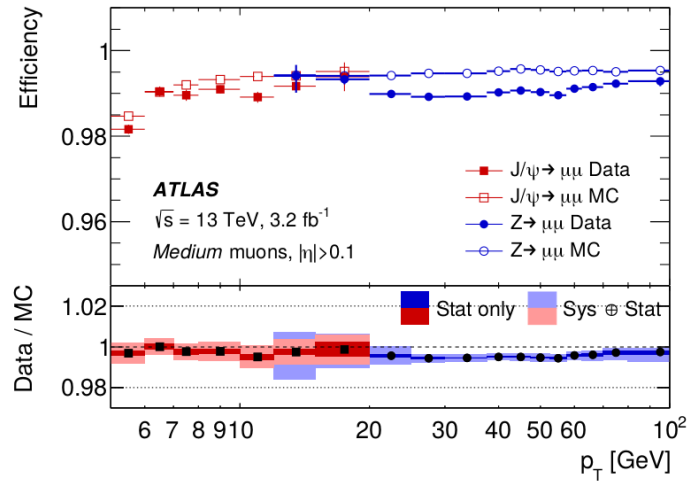


**Figure 3.7:** Reconstruction efficiency for *Medium* muons used in this thesis as a function of the measured  $p_T$  in data and simulated  $Z \rightarrow \mu^- \mu^+$  and  $J/\Psi \rightarrow \mu^- \mu^+$  events [56]. The bottom panel shows the efficiency ratio of data to simulation.

Furthermore, the reconstruction efficiencies as a function of  $\eta$  for Loose and Medium working points are found to be very similar with the exception of the region  $|\eta| < 0.1$ , as shown in Figure 3.8. In this region the Loose selection fills the MS acceptance gap using the calorimeter information. The plots also show efficiencies in excess of 98% for Loose and Medium muons, and between 90% and 98% for Tight muons.

Similar to electrons, the muon isolation requirements use calorimeter and track-based variables in order to quantify the amount of additional activity surrounding the muon. From these variables, several “isolation working points” are then defined according to Ref. [56].

The isolation efficiency for CB muons is derived using tag-and-probe method in data and simulated  $Z \rightarrow \mu^- \mu^+$  events. Figure 3.9 shows an example of the muon isolation efficiency as a function of  $p_T$  corresponding to the *Fix (Loose)* isolation working point.

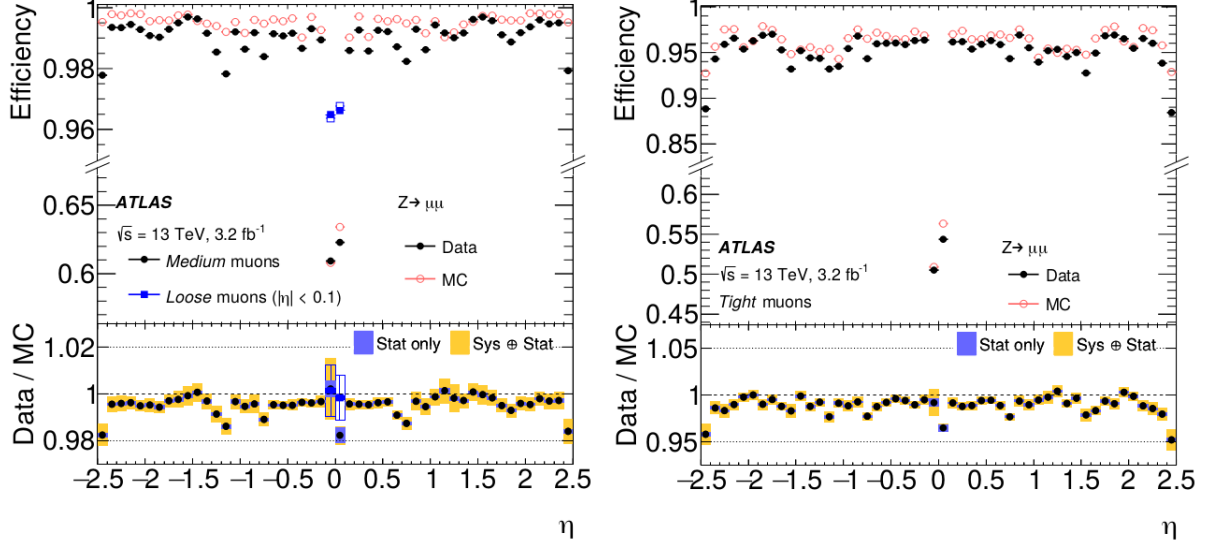


**Figure 3.8:** Reconstruction efficiency for Loose and Medium (left) and Tight (right) muons as a function of  $\eta$  in data and simulated  $Z \rightarrow \mu^- \mu^+$  events [56]. The bottom panel shows the efficiency ratio of data to simulation.

As shown, the isolation efficiency is  $>93\%$  for low- $p_T$  muons and close to 100% for  $p_T > 40$  GeV. The data/MC correction factors are  $>0.99$  (less than 1%) for the entire  $p_T$  range. Other isolation working points present efficiencies in excess of 95% across all  $p_T^\mu$  [56].

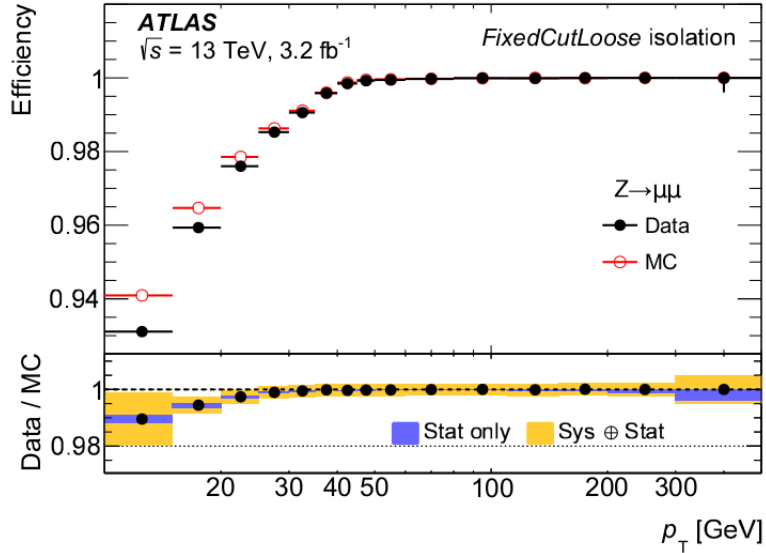


**Figure 3.9:** Efficiency for *Fix* (*Loose*) isolation criteria for muons used in this thesis as a function of the measured  $p_T^\mu$  [56].

The muon momentum magnitude and resolution are studied in  $Z \rightarrow \mu^- \mu^+$  and  $J/\Psi \rightarrow \mu^- \mu^+$  events. Correction factors, as a function of the muon  $p_T$  in various  $\eta$  regions, are derived and applied to the simulated muon  $p_T$  so that the  $\mu^- \mu^+$  invariant mass matches



the known value of the Z boson mass [56]. For  $Z \rightarrow \mu^- \mu^+$  decays, the uncertainty in the muon momentum magnitude varies from a minimum of 0.05% for  $|\eta| < 1$  to a maximum of 0.3% for  $|\eta| \sim 2.5$ . The muon  $p_T$  resolution is around 1.7% and 2.3% at small values of pseudorapidity and 2.3% and 2.9% in the end-caps for  $Z \rightarrow \mu^- \mu^+$  and  $J/\Psi \rightarrow \mu^- \mu^+$  decays, respectively.

### 3.2.3 Fake and non-prompt leptons

For the purposes of this thesis, only leptons directly produced in the hard interaction (prompt) are of particular interest. However, other objects such as converted photons or jets, can sometimes mimic the lepton signature in the detector and be wrongly identified as leptons (fakes). Leptons reconstructed with the wrong electric charge are also considered fakes. In addition, leptons that do not come from the hard interaction (non-prompt) can often be mis-identified as prompt.

In this thesis, three types of fake or non-prompt leptons are considered, whose specific characteristics are described in the following paragraphs. Both fake and non-prompt leptons will be referred to as *fake* leptons hereafter for simplicity.

- **Electrons with incorrectly assigned electric charge.** This type of fake electrons are produced via two main mechanisms: hard bremsstrahlung and mis-measurement of the electron track curvature (Figure 3.10).

In the hard bremsstrahlung scenario, the original electron radiates a high energy photon that splits into an  $e^+e^-$  pair, resulting in three electrons (original + pair). An electron can be reconstructed with the wrong electric charge if the opposite sign electron track is the one matched to the energy cluster in the EMCal instead of the original electron track.

The electron track curvature mis-measurement occurs mainly for high- $p_T$  electrons, where the track curvature radius is quite large and, therefore, more difficult for the track reconstruction algorithms to assign the correct curvature sign to the track.

Electrons produced in these two ways will be referred to as *Charge Flip Fake* (CFFake) electrons throughout this thesis. The presence of CFFake muons is negligible due to the long lever arm in the muon system and the fact that the charge measurement is performed (and cross-checked) by both the ID and the MS.

- **Leptons produced in hadron decays.** Non-prompt leptons produced in the in-flight decay of hadrons will be referred to as *Hadronic Decay Fake* (HDFake) leptons throughout this thesis. As opposed to prompt leptons, which come from the PV, HDFake leptons are characterized by being originated from the displaced secondary vertex (SV) created by the hadron decay. Additionally, they are generally not well

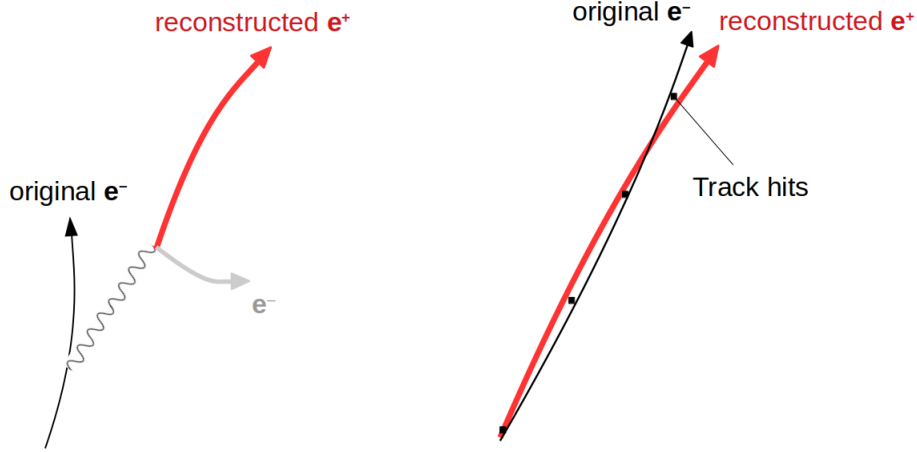


**Figure 3.10:** Mechanisms contributing to the charge electron mis-assignment: hard bremsstrahlung (left) and mis-measurement of electron track curvature (right). Black lines represent the original electron and red arrows correspond to the reconstructed opposite-sign electron.

isolated due to the presence of the other hadron decay products. An example of HDFake lepton production is depicted in Figure 3.11, where a  $b$ -hadron decays into a  $c$ -hadron and an electron-neutrino pair ( $B^- \rightarrow e^- + \bar{\nu}_e + \bar{D}^0$ ).

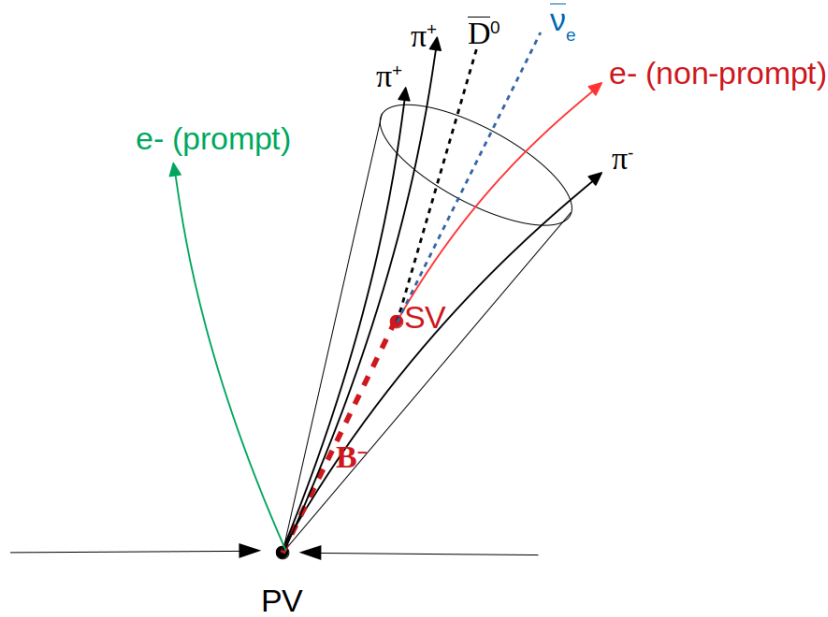


**Figure 3.11:** Schematic representation of jet containing a  $b$ -hadron ( $B^-$ ) that decays into a  $c$ -hadron ( $\bar{D}^0$ ), a neutrino and a non-prompt electron. The secondary vertex from which the non-prompt electron is originated is represented by a red dot labeled “SV”. In addition, a prompt electron originated at the primary vertex (PV) is represented in green color.

- **Electrons produced by photon conversion.** Two types of photon conversion can occur: conversion of *real* photons by interacting with the detector material, i.e., *Material Conversions Fake* (MCFake) electrons; conversion of *virtual* photons with

a (virtual) mass greater than 1.022 MeV ( $2m_e$ ) that intermediately converts to an  $e^-e^+$  pair, i.e., *Internal Conversions Fake* (ICFake) electrons. MCFakes can occur only by electromagnetic interaction with the detector material and, therefore, will be typically produced after the first Silicon layer of the inner detector. ICFakes, however, typically originates very close to the hard interaction point.

### 3.3 Jets

Color-charged partons produced in hard-scattering interactions are not directly observed in the detector due to color confinement (see Section 1.1.3). Instead, they shower and quickly recombine with other colored partons to form hadrons, whose momentum vector is very close to the original parton trajectory. These hadrons interact through nuclear reactions in the calorimeter systems, creating collimated sprays of particles called *jets*.

Jets are reconstructed using a clustering algorithm that runs on a set of input four-vectors typically obtained from topologically-associated energy deposits in the calorimeter systems (calorimeter-jets). In addition, jets can be reconstructed using inputs from charged particle track (track-jets) or simulated final state particles<sup>3</sup> (particle-jets). Track-jets and particle-jets are only used within the scope of this section in order to derive calorimeter-jet calibrations, which will be described in Section 3.3.1. Therefore, the term *jet* will be used in this thesis only in relation to calorimeter-jets.

The jet reconstruction process begins by constructing three-dimensional topological clusters of energy deposits in the calorimeters [58]. Calorimeter cells with an energy above four times the cell average (expected) noise,  $\sigma_{noise} = \sqrt{(\sigma_{noise}^{elec.})^2 + (\sigma_{noise}^{pileup})^2}$ , become topological clusters seeds. The  $\sigma_{noise}^{elec.}$  term corresponds to the electronic noise produced in the readout modules. The  $\sigma_{noise}^{pileup}$  term corresponds to the pileup noise, which is defined as the root mean square (RMS) of the energy cell distribution resulting from pileup particles for a given  $\langle\mu\rangle$ . All the neighboring<sup>4</sup> cells are added iteratively if their energy is greater than twice  $\sigma_{noise}$ . After no more cells fulfill this requirements, the adjacent cells are added, with no noise threshold requirement. The energy measurement in a topological cluster is assumed to be caused by a massless particle with four-vector of magnitude  $E = \sum E_{cell}$  and directed from the center of the detector towards the energy-weighted barycenter of the topological cluster.

---

<sup>3</sup>Candidate particles are required to have a lifetime of  $c\tau > 10$  mm and muons, neutrinos, and particles from pileup activity are excluded.

<sup>4</sup>Here *neighboring* is generally defined as two calorimeter cells being directly adjacent in a given sampling layer, or, if in adjacent layers, having at least partial overlap in the  $\eta - \phi$  plane.

After the topological clustering is complete, the four-vector collection of all topological clusters with positive total energy<sup>5</sup> are used as inputs for the anti- $k_t$  clustering algorithm [59, 60] with a radius parameter of  $R = 0.4$ . The output of this algorithm is a collection of jets whose four-vectors are determined by the combination of their corresponding topological clusters four-vector.

### 3.3.1 Jet energy scale calibration

Jets are initially reconstructed at the electromagnetic scale (EM-scale), which means that the calorimeter cell energy measurements correspond to the energy deposited by electromagnetically interacting particles only. Therefore, in order to recover the true jet energy (i.e. particle-jet energy), a jet energy scale (JES) calibration must be applied to the EM-scale jets. The calibrations addresses several different effects that include:

- **Calorimeter non-compensation:** differences between the electromagnetic and hadronic calorimeters energy measurements due to the fact that the EMCal response is different for hadrons and leptons (or photons) and it is initially calibrated to the EM-scale.
- **Dead material:** energy lost in inactive areas of the detector.
- **Energy deposits below noise thresholds:** some particles do not make it into any clusters due to the threshold cuts on energy to suppress background noise.
- **Leakage:** showers may not be completely contain within the calorimeters outer edge.
- **Pileup:** additional calorimeter energy deposits from pileup interactions.

In the following sections, a general description of the sequential JES calibration for jets used in this thesis is given [61].

#### Origin correction.

All reconstructed jets are initially assumed to originate from the geometrical center of the ATLAS detector. Therefore, the first correction step recalculates the four-momentum of the jets in such a way that they point to the hard scattering primary vertex instead. This correction maintains the jet energy constant and improves the  $\eta$  resolution of the jets (as measured from the difference between reconstructed and particle jets in MC simulations)

---

<sup>5</sup>Note that negative-energy cells are allowed as long as the total cluster energy is positive. A negative energy deposit can occur due to electronic noise or fluctuations from pileup events.

from roughly 0.06 to 0.045 at a jet  $p_T$  of 20 GeV and from 0.003 to below 0.006 for jets with  $p_T > 200$  GeV.

### Pileup correction.

Pileup contributions can modify the jet kinematics (e.g., by artificially increasing the jet  $p_T$ ). Since pileup particles are not used in particle-jets, the difference between the reconstructed jets  $p_T$  and the matched<sup>6</sup> particle-jets  $p_T$  is used to derive the pileup correction. This correction is parameterized as a function of the number of reconstructed vertices and the mean number of interaction per bunch crossing (Eq. 2.5). The jet pileup correction is applied in a per-event basis according to Ref. [62].

### Absolute jet energy scale and $\eta$ calibrations.

After the origin and pileup corrections, the next step consist in calibrate the reconstructed jet four-momentum to recover the actual particle-jet energy scale (EM+JES)<sup>7</sup> [63]. This calibration is derived from di-jet MC simulated samples where reconstructed EM-scale jets are geometrically matched to the corresponding particle-jet within  $\Delta R < 0.3$ . Only isolated<sup>8</sup> jets are used, in order to avoid ambiguities in the matching.

The absolute JES calibration is estimated from the EM-scale energy response ( $\mathcal{R}_{jet} = E_{jet}^{reco} / E_{jet}^{particle}$ ) of each pair of reconstructed/particle-jet and parameterized as a function of  $E_{jet}^{reco}$  and the calorimeter jet detector pseudorapidity,  $\eta_{det}$ <sup>9</sup>.

### Global sequential calibration.

The Global Sequential Calibration (GSC) is also derived from MC simulated samples and comprises five stages accounting for the jet response dependence on:

1. The fraction of energy deposited in the first layer of the tile calorimeter.
2. The fraction of energy deposited in the third layer of the electromagnetic calorimeter.
3. The number of tracks with  $p_T > 1$  GeV associated to the jet.
4. The  $p_T$ -weighted transverse width of the jet measured using tracks with  $p_T > 1$  GeV associated to the jet.

---

<sup>6</sup>Reconstructed jets with  $p_T > 10$  GeV are geometrically matched to particle jets within  $\Delta R = 0.3$ .

<sup>7</sup>After the absolute JES calibration, jets are commonly referred to as EM+JES jets.

<sup>8</sup>An isolated calorimeter jet is required to have no other calorimeter jet of  $p_T > 7$  GeV within  $\Delta R < 0.6$ , and only one particle jet of  $p_T^{particle} > 7$  GeV within  $\Delta R < 1.0$ .

<sup>9</sup>Here,  $\eta_{det}$  refers to the original reconstructed jet before the origin correction, which is defined from the geometrical center of the detector instead of from the interaction point.

5. The amount of activity behind the jet as measured in the muon spectrometer ("punch-through").

The first four corrections are derived as a function of jet  $p_T$ , while the punch-through correction is derived as a function of jet energy, being more correlated with the energy escaping the calorimeters. The dependence of the jet response on each effect is reduced to less than 2% after the full GSC is applied.

### ***In situ* calibrations.**

So far, all JES corrections have been derived using simulated samples. However, in order to account for possible MC mis-modelings, the final step in the JES calibration, known as *in situ* calibrations, attempts to correct the differences between data and MC simulations. The *in situ* techniques quantify these mis-modelings by balancing out the  $p_T$  of the jets against other well measured reference objects in the event such as photons, Z bosons or other jets. Three main calibration types are applied sequentially to the jet four-momentum in data:

- **$\eta$ -intercalibration:** For uniform  $p_T$  response across the full detector  $\eta$  coverage, forward jets ( $0.8 < |\eta| < 4.5$ ) are calibrated to the same scale of central jets ( $|\eta| < 0.8$ ) in di-jet events by requiring a  $p_T$  balance between them [64]. The aim is to remove any residual pseudorapidity difference in the jet response.
- **Z/ $\gamma$  + jets balance:** The balance of Z bosons and photons recoiling against jets is used to derive *in situ* JES corrections for jets with  $|\eta| < 0.8$  [65]. These measurements are carried out for jets with  $20 \leq p_T \leq 200$  GeV (Z+jet) and  $30 \leq p_T \leq 800$  GeV ( $\gamma$ +jet).
- **Multijet balance:** High- $p_T$  jets are calibrated using events in which a system of low- $p_T$  jets recoil against a single high- $p_T$  jet [64]. This method covers a range of  $300 \leq p_T \leq 1700$  GeV.

### **3.3.2 Jet energy resolution**

The precision of the jet energy measurement is known as Jet Energy Resolution (JER). Typically, the measured energy of a jet is spread around its true value due to noise (electronic and pileup), stochastic fluctuations in the calorimeter response (statistical

Poisson fluctuations due to sampling nature of calorimeter) or detector calibration effects. The JER is then parameterized as a function of the jet momentum as<sup>10</sup>:

$$\frac{\sigma(p_T^{jet})}{p_T^{jet}} = \frac{N}{p_T^{jet}} \oplus \frac{S}{\sqrt{p_T^{jet}}} \oplus C \quad (3.1)$$

where  $N$  and  $S$  are parameters that correspond to the noise and stochastic effects respectively, and  $C$  is an energy-independent constant term.

The JER is measured in data and MC samples as a function of  $p_T$  and  $|\eta|$  by computing the distribution width of the balance between jets and well measured photons or reconstructed  $Z$  bosons (decaying as  $Z \rightarrow \mu^- \mu^+ / e^- e^+$ ) [65]. Additionally, the balance between di-jet events can be used to extend these measurements to higher  $|\eta|$  and  $p_T$  [64]. The JER ranges from 20% for  $p_T^{jet} = 25$  GeV to less than 10% for  $p_T^{jet} > 100$  GeV with uncertainties below 3% for the entire kinematic range [66].

### 3.3.3 $b$ -jets identification

The analysis presented in this thesis crucially depends on the correct identification of jets induced by  $b$ -quarks ( $b$ -jets).

The algorithms that perform this identification of  $b$ -jets are called *b-tagging* algorithms. These algorithms exploit the long lifetime, high mass and high decay multiplicity of  $b$ -hadrons as well as the properties of the  $b$ -quark fragmentation to correctly identify  $b$ -jets. The  $b$ -hadrons have typical lifetimes on the order of 1.5 ps ( $\langle c\tau \rangle \approx 450 \mu m$ ) leading to significant mean flight length ( $\beta\gamma c\tau$ ) inside the detector before decaying. This means that jets containing  $b$ -hadrons will typically contain tracks that originates from at least one secondary vertex displaced from the hard-scatter collision point [67].

The  $b$ -jet identification process used in this thesis consists of a two-step approach that follows the methodology described in Ref. [68–70]. It begins with a reconstruction of the characteristic features of the  $b$ -jets, discussed in the previous paragraph. This is done using the individual properties of charged-particle tracks associated with a hadronic jet [69] or combining tracks to explicitly reconstruct displaced vertices [68, 70]. After that, the results are combined into a multivariate classifier algorithm, called *MV2c10* [71], in order to maximize the  $b$ -tagging performance.

The MV2c10 algorithm performance is characterized by the efficiency with which a  $b$ -jet is correctly tagged ( $\epsilon_b$ ) and the efficiencies at which  $c$ - or *light*-jets are incorrectly tagged as  $b$ -jets ( $\epsilon_c$  and  $\epsilon_{light}$ ). These efficiencies are estimated for different  $b$ -tagging *Working Points* (WP) defined by fixed cuts of the MV2c10 discriminant. Table 3.1 shows

<sup>10</sup>At fixed rapidity this is equivalent to the fractional jet energy resolution,  $\frac{\sigma(E)}{E}$ .

the different  $b$ -tagging WP available and the corresponding  $\epsilon_b$  together with the  $c$ /light rejection factors, defined as  $1/\epsilon_c$  and  $1/\epsilon_{light}$ , respectively. Figure 3.12 shows the MV2v10 BDT output for  $b$ -,  $c$ - and  $light$ -jets evaluated in  $t\bar{t}$  simulated events.

**Table 3.1:** MV2c10 fixed Operating Points and corresponding  $b$ -tagging efficiencies and  $c$ /light rejection factors. The “Cut” column indicates the MV2c10 score (Figure 3.12) cut applied to the jets to get the corresponding efficiency WP in column “ $\epsilon_b$ ”.

$\epsilon_b$	Cut	Rejection factor	
		$c$ -jet	$light$ -jet
60%	$> 0.94$	23	1200
70%	$> 0.83$	8.9	300
77%	$> 0.64$	4.9	110
85%	$> 0.11$	2.7	25

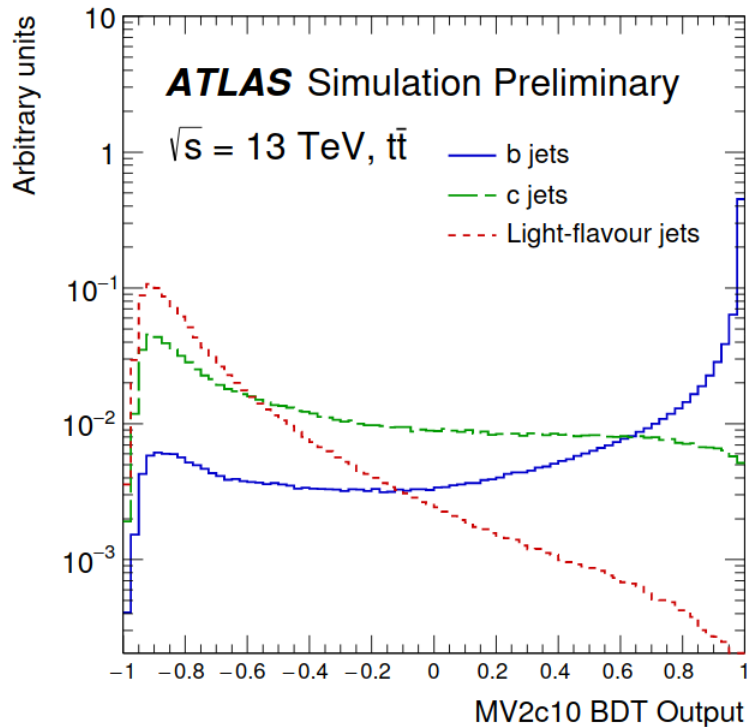


**Figure 3.12:** MV2c10 BDT output for  $b/c/light$ -jets evaluated in  $t\bar{t}$  simulated events [71].

### 3.4 Missing transverse energy

In all measurements, it is expected that the vectorial sum of all the transverse momentum contributions per event is zero, i.e. momentum must be conserved. Any imbalance is therefore associated to missing transverse energy or  $E_T^{miss}$ . This imbalance is expected to come from neutrinos, since they do not interact with the detector material.



The  $E_T^{miss}$  reconstruction is characterized by two contributions. The first one comes from hard-scatter event signals comprising fully reconstructed and calibrated particles and jets (hard objects). The second contribution to  $E_T^{miss}$  comes from reconstructed charged-particle tracks (soft signals) associated with the hard-scatter vertex but not with any hard objects [72]. Therefore, the  $x$  and  $y$ -coordinates of the  $E_T^{miss}$  vector are given by:

$$E_{x(y)}^{miss} = - \sum_{i \in \text{hard objects}} p_{x(y),i} - \sum_{j \in \text{soft signals}} p_{x(y),j} \quad (3.2)$$

where:

$$\sum_{i \in \text{hard objects}} p_{x(y),i} = \sum p_{x(y)}^e + \sum p_{x(y)}^\gamma + \sum p_{x(y)}^\mu + \sum p_{x(y)}^{\tau_{had}} + \sum p_{x(y)}^{jets} \quad (3.3)$$

$$\sum_{j \in \text{soft signals}} p_{x(y),j} = \sum_{\text{unused tracks}} p_{x(y)}^{soft} \quad (3.4)$$

From the components of  $E_T^{miss}$  obtained with Eq. 3.2, the magnitude of  $E_T^{miss}$  is calculated as:

$$|E_T^{miss}| = \sqrt{(E_x^{miss})^2 + (E_y^{miss})^2} \quad (3.5)$$

In this thesis, no explicit event requirement based on  $E_T^{miss}$  is applied. However, given the targeted final states, which will be discussed in Chapter 4, a sizable  $E_T^{miss}$  component is expected due to the presence of leptonic decays producing neutrinos.

### 3.5 Ambiguity resolution in objects selection

Ambiguities can arise when two different objects are reconstructed using the same calorimeter cluster, track or MS signal, which can lead to double counting or fake objects. In order to resolve such ambiguities a procedure called *overlap removal* (OR) is used. The OR procedure used in this thesis resolves any ambiguity between object candidates in the following order: any electron within  $\Delta R = 0.1$  of another electron with higher  $p_T$  is removed; any electron within  $\Delta R = 0.1$  of a muon is removed; any jet within  $\Delta R = 0.3$  of an electron is removed; if a muon and a jet lie within  $\Delta R = \min(0.4, 0.04 + 10 [GeV]/p_T^{\mu on})$ <sup>11</sup> of each other, the jet is kept and the muon is removed; any hadronically decaying tau ( $\tau_{had}$ ) within  $\Delta R = 0.2$  of an electron or muon is removed; any jet within  $\Delta R = 0.3$  of a

<sup>11</sup>Note that this is not the same  $\Delta R$  as the ones used before, which are defined by 2.8. The cut value is optimized to maximize the acceptance of real muons at a fixed rejection factor for non-prompt muon originating from hadron decays within the jet.

$\tau_{had}$  is considered only as a  $\tau_{had}$  in events with two light leptons. A summary of the OR used in this thesis is presented in Table 3.2.

**Table 3.2:** Summary of the overlap removal procedure between electrons, muons, hadronically decaying taus, and jets.

Keep	Remove	Cone size ( $\Delta R$ )
electron	electron (low- $p_T$ )	0.1
muon	electron	0.1
electron	jet	0.3
jet	muon	$\min(0.4, 0.04 + 10 [GeV]/p_T^{muon})$
electron	$\tau_{had}$	0.2
muon	$\tau_{had}$	0.2
$\tau_{had}$	jet	0.3

---

## Chapter 4

# Search for Higgs bosons produced in association with top-quark pairs in multilepton final states

This chapter is dedicated to describe the analysis of the search for Higgs bosons produced in association with top-quark pairs in multilepton final states ( $t\bar{t}HML$ ).

The  $t\bar{t}HML$  process is characterized by final state topologies containing several prompt leptons and jets produced by the decay of the top-quark pair and the Higgs boson. Top-quarks decay almost exclusively into a bottom-quark and a W boson ( $t \rightarrow bW$ ), while the Higgs boson can decay via several channels, as shown in Table 1.2. However, when prompt leptons are required from the Higgs decay chain,  $t\bar{t}HML$  is most sensitive to  $H \rightarrow WW^*$ , with small contributions from  $H \rightarrow \tau^-\tau^+$  and  $H \rightarrow ZZ^*$  decays. Figure 4.1 shows examples of lower order Feynman diagrams for the different  $t\bar{t}HML$  processes considered in this thesis.

The collected datasets and Monte Carlo (MC) samples used in this analysis are described in Section 4.1. The analysis-specific physics object selections used in this thesis are detailed in Section 4.2, with special focus on the suppression of fake leptons. These object definitions are then used in Section 4.3 to define event selections that uniquely identify the  $t\bar{t}HML$  final states. In particular, my work focuses on two specific  $t\bar{t}HML$  channels: two same-sign lepton channel ( $2\ell SS$ ) and three lepton channel ( $3\ell$ ). These are expected to be the most sensitive channels due to distinctive signature, that allows for higher background suppression, and sufficient statistic due to the relatively high Higgs branching ratios [25].

Once the event selections are defined, the sources of background for each channel and their estimation is presented in Section 4.4. After that, all events are categorized as described in Section 4.5 using cuts on different event properties, i.e. using a *cut-based* approach. The goal is to define regions of phase-space enriched in signal and specific

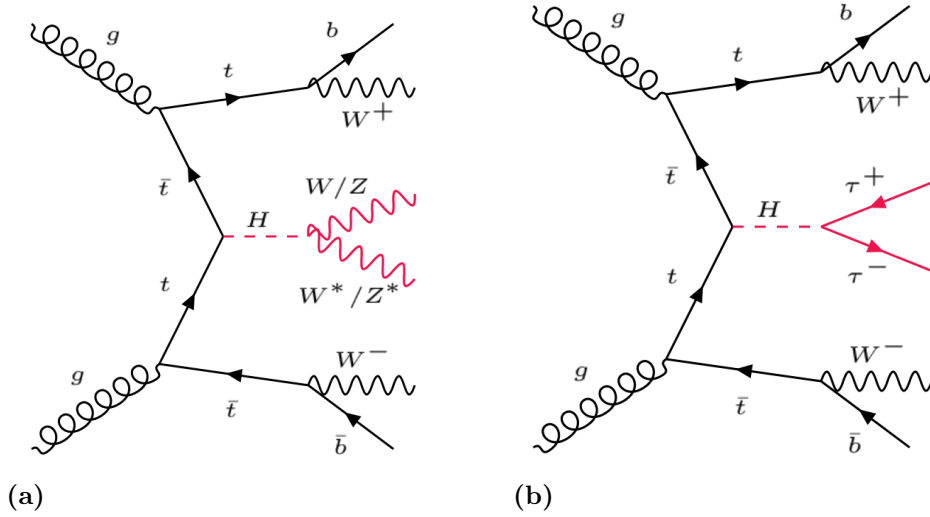


**Figure 4.1:** Feynman diagrams showing examples of Higgs decay modes (highlighted in red) that contribute to the  $t\bar{t}HML$  final states considered in this analysis: (a) the Higgs boson decays to a pair of  $W$  or  $Z$  bosons; (b) the Higgs boson decays to a pair of tau leptons. Only  $H \rightarrow \tau^-\tau^+$  events where both taus decay leptonically are considered in the analysis presented in this thesis. Note that the  $W$  bosons from the Higgs decay represented in (a) have opposite-sign. Off-shell bosons are marked with a star.

backgrounds, where  $\mu_{t\bar{t}H}$  (see Eq. 1.35) and normalization factors for those backgrounds can be simultaneously determined from a likelihood fit to data. The statistical model used in the fit and its results are presented in Sections 4.6 and 4.7.

## 4.1 Data and Monte Carlo samples

### 4.1.1 Data taking

The data used in the analysis presented in this thesis consists of proton-proton collision events collected by the ATLAS detector during the 2015-2017 period at a center-of-mass energy of 13 TeV.

Only recorded data that is certified to be good quality is used in this analysis, which correspond to an integrated luminosity of  $80 \text{ fb}^{-1}$  (blue cumulative distribution in Figure 2.2). The quality assessment requires all the detector subsystems to be in a good operating condition and all the physics objects to have good reconstruction quality. These requirements reduced the integrated luminosity that can be used for physics analysis to about 86% of the total integrated luminosity delivered by the LHC during the 2015-2017 data-taking campaign.

### 4.1.2 Triggered data events

Data events recorded by the ATLAS detector are only used in this analysis if a lepton pair with  $p_T$  above certain threshold triggered the event, according to the procedure described in Section 2.2.4. Table 4.1 shows the specific combination of di-lepton HLT triggers used in this analysis for each year period. On top of the  $p_T$  thresholds corresponding to each trigger, strict lepton identification criteria are imposed in some cases, in order to ensure high trigger efficiency. In order to cope with the increase in instantaneous luminosity for the 2016 and 2017 data-taking periods (see Figure 2.2), the trigger  $p_T$  thresholds are increased. The data events used in this thesis are required to pass the logical OR of the di-lepton triggers listed in Table 4.1.

**Table 4.1:** List of di-lepton triggers used in this analysis depending on the year that the data was recorded. The column “lepton pair” corresponds to the specific combination of the triggered object; the “ $p_T$  threshold” column contains the  $p_T$  threshold for each triggered object: a single value means that both leptons have the same cut.

Year	Lepton pair	$p_T$ threshold (GeV)	Identification WP
2015	$ee$	$\geq 12$	Loose
	$\mu\mu$	$\geq 18$ and $\geq 8$	-
	$e\mu/\mu e$	$\geq 17(e)$ and $\geq 14(\mu)$	Loose ( $e$ )
2016	$ee$	$\geq 17$	Very Loose
	$\mu\mu$	$\geq 22$ and $\geq 8$	-
	$e\mu/\mu e$	$\geq 17(e)$ and $\geq 14(\mu)$	Loose ( $e$ )
2017	$ee$	$\geq 24$	Very Loose
	$\mu\mu$	$\geq 22$ and $\geq 8$	-
	$e\mu/\mu e$	$\geq 17(e)$ and $\geq 14(\mu)$	Loose ( $e$ )

### 4.1.3 Monte Carlo samples

Monte Carlo simulated samples are used in this analysis in order to estimate the contribution of the  $t\bar{t}H$  signal and the background processes. The hard scatter  $pp$  collision is generated for each process of interest using different generators, which will be discussed in the following paragraphs. Pileup interactions are generated using PYTHIA 8.186 (referred to in the following as PYTHIA8) [73] with the A3 set of tuned parameters [74] (referred to as “tune”), and are overlaid to the simulated hard scattering event. The pileup distribution is then reweighed to reflect the mean number of interactions per bunch crossing observed in data (see Figure 2.3).

All generated events are processed through a simulation of the ATLAS detector using GEANT4 [75] in order to model the detector geometry and response [76]. After that, all simulated events are processed using the same reconstruction algorithms and analysis chain as the data.

The simulated events are corrected so that the objects reconstruction, identification and isolation efficiencies match those determined from data by applying multiplicative scale factors. A similar approach is used to correct for energy scale and resolution. All events are also normalized to their corresponding cross-sections, calculated to the highest available order in perturbation theory.

Table 4.2 shows a summary of the MC samples used in this thesis. Further details on specific simulated samples for different processes are presented in the following subsections.

### $t\bar{t}H$ simulation

The sample used to model the  $t\bar{t}H$  process was generated using POWHEG-BOX version 2 (referred to in the following as POWHEG) [77, 78] with a next-to-leading-order (NLO) matrix element (ME) and the NNPDF3.0 NLO parton distribution function (PDF) set [79]. The renormalization and factorization scales,  $\mu_R$  and  $\mu_F$ , are set equal to the geometric mean of the transverse energies of the top quark, the anti-top quark, and the Higgs boson, whose masses are taken as  $m_{top} = 172.5$  GeV and  $m_H = 125$  GeV respectively. The Higgs boson decay branching ratios are calculated using HDECAY [20, 80].

The ME calculation is then interfaced to the PYTHIA8 [81] generator with the A14 tune [82] to model the parton shower (PS), hadronization and multi-parton interactions. The POWHEG model parameter  $h_{damp}$ , which controls the ME to PS matching and effectively regulates the amount of high- $p_T$  radiation, is set to  $1.5 \times (2m_{top} + m_H)/2 = 352.5$  GeV.

The simulated sample is normalized using a cross-section of 507 fb, which is computed at NLO in QCD with the leading order (LO) electroweak corrections [83–88].

### $t\bar{t}W$ simulation

The  $t\bar{t}W$  process was modeled using the SHERPA 2.2.1 [89] generator with the NNPDF3.0 NLO PDF set. The ME calculation was performed for up to one additional parton at NLO and up to two partons at LO using COMIX [90] and OPENLOOPS [91]. These two calculations were then merged with the SHERPA parton shower [92] using the MEPS@NLO prescription [93] with a merging scale of 30 GeV. The scales  $\mu_R$  and  $\mu_F$  are set both equal to  $H_T/2$ , where  $H_T$  is defined as the scalar sum of the transverse masses ( $\sqrt{p_T^2 + m^2}$ ) of all final state partons.

The  $t\bar{t}W$  sample is normalized using a cross-section value of 601 fb, which is computed at NLO in QCD with LO electroweak corrections [20, 94, 95]. However, additional inclusive cross-section scale factors are used to account for observed mis-modeling of the QCD and electroweak corrections. It has been shown by [96] that the NLO QCD corrections to  $t\bar{t}W$

with one additional jet can be quite large. Therefore, an inclusive scale factor of 1.11 was estimated using dedicated samples generated by SHERPA 2.2.5 with the MEPS@NLO prescription and cross-checked with the NLO generator MADGRAPH5\_AMC@NLO 2.2.1 (referred to in the following as MG5\_AMC@NLO) [96] using the FxFx prescription [97]. In addition, recent work done by [98] has shown that NLO electroweak corrections for  $t\bar{t}W$  production are larger than expected. To account for this, an additional 1.09 inclusive scale factor is used. In total, an extra scale factor correction of 1.2 is applied to the  $t\bar{t}W$  inclusive cross-section. Thus, a corrected  $t\bar{t}W$  cross-section of 721 fb is used for normalization.

### $t\bar{t}(Z/\gamma^*)$ simulation

The  $t\bar{t}(Z/\gamma^*)$  process is simulated using MADGRAPH5\_AMC@NLO with the NNPDF3.0 NLO PDF set. The renormalization and factorization scales are both set to  $H_T/2$ . The ME calculations are then interfaced to the PYTHIA8 generator with the A14 tune.

This  $t\bar{t}(Z/\gamma^*)$  sample only contains on-shell  $Z$  and off-shell  $Z/\gamma^*$  contributions, where the produced lepton pair ( $Z/\gamma^* \rightarrow \ell^+\ell^-$ ) has an invariant mass above 5 GeV. These processes will be called “high-mass”  $t\bar{t}\ell^+\ell^-$  hereafter. The modeling of  $t\bar{t}(Z/\gamma^*)$  with  $1 \text{ GeV} < m_{\ell^+\ell^-} < 5 \text{ GeV}$  is accounted for by using an additional “low-mass”  $t\bar{t}\ell^+\ell^-$  sample produced with the same generators and tune set. Both  $t\bar{t}\ell^+\ell^-$  samples model the production of the virtual photon only from initial state radiation (as depicted in Figure 4.2 (a)) in the ME with NLO precision. The cross-sections used for normalization of the “high-mass” and “low-mass” samples are 881 fb and 39 fb respectively, which were computed at NLO with QCD and electroweak corrections [20, 95, 96].

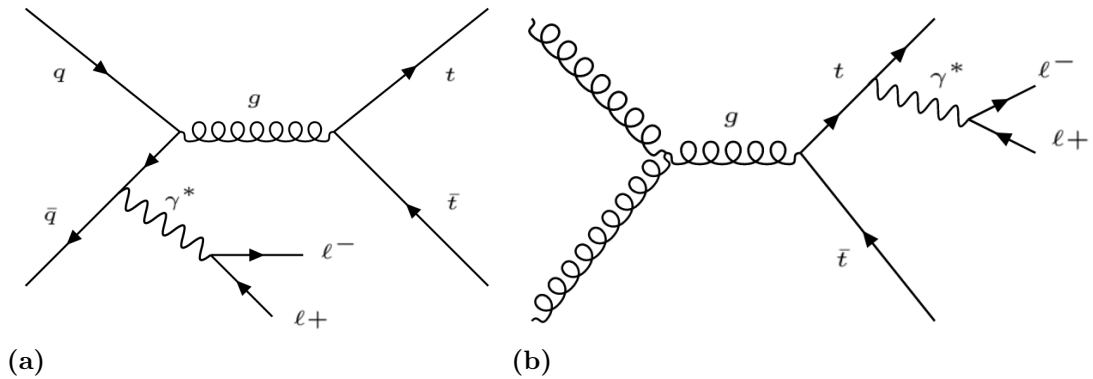


**Figure 4.2:** Examples of lowest order Feynman diagrams for virtual photons that are included in the ME modeling of (a) initial state radiation in  $t\bar{t}\ell^+\ell^-$  processes and (b) final state radiation “rare- $t\bar{t}$ ” processes.

Furthermore, a dedicated  $t\bar{t}\gamma^*$  sample that contains the so called “rare- $t\bar{t}$ ” decay ( $t\bar{t} \rightarrow W^+bW^-\bar{b}\gamma^*(\gamma^* \rightarrow \ell^+\ell^-)$ ) is used. This sample models the production of a virtual photon only from final state radiation (e.g. Figure 4.2 (b)) with  $m_{\ell^+\ell^-} > 1 \text{ GeV}$  in the ME at

leading order. The cross-section used for the normalization of this sample is 394 fb and was scaled by a factor of 1.54 according to Ref. [99–103] to account for higher order EW corrections.

## $t\bar{t}$ simulation

The estimation of the fake lepton background coming from hadron decays and photon conversions is done primarily using an inclusive  $t\bar{t}$  sample. It was generated using POWHEG and interfaced with PYTHIA8 for the parton showering and fragmentation. The CT10/CTEQ6L1 PDF set [104, 105] and Perugia 2012 [106] tune were used in the generation of this sample. An inclusive cross-section of 832 pb, calculated at NNLO QCD, is used for the  $t\bar{t}$  normalization [107].

Virtual photons production is also included in the  $t\bar{t}$  sample and modeled by QED multi-photon radiation via the PS. However, this introduces potential overlap with “rare- $t\bar{t}$ ” and  $t\bar{t}\ell^+\ell^-$ . Since these samples have a lower  $m_{\ell^+\ell^-}$  cutoff at 1 GeV, the  $t\bar{t}$  sample described here is used only for photon conversions ( $\gamma^* \rightarrow \ell^+\ell^-$ ) with  $m_{\ell^+\ell^-} < 1$  GeV.

## Other simulated samples

Diboson and Triboson processes are generated with SHERPA 2.2.2 at NLO precision using NNPDF3.0 NLO PDF set with up to 3 extra partons included at LO using the default PS tune.

Other processes, such as  $tH$ ,  $t(Z/\gamma^*)$ ,  $tHW$ ,  $tW(Z/\gamma^*)$ ,  $t\bar{t}t$ ,  $t\bar{t}t\bar{t}$ ,  $t\bar{t}W^+W^-$ , and single-top are only expected to contribute very little to the total background. The generator settings used for those processes are included in Table 4.2.

Alternative samples were also produced in order to compute some of the systematic uncertainties. The uncertainty related to the choice of parton shower and hadronization models in  $t\bar{t}H$  is estimated by comparing the nominal POWHEG+PYTHIA8 to a sample generated with POWHEG+HERWIG7 using the H7-UE-MMHT tune [108]. Furthermore, the uncertainty on the ME calculations in  $t\bar{t}W$  is determined from the comparison of SHERPA 2.2.1 (nominal) and an alternative sample generated with MG5\_AMC@NLO + PYTHIA8 using the A14 tune. Similarly, a  $t\bar{t}(Z/\gamma^*)$  sample generated using SHERPA 2.2.0 is used to estimate the uncertainty in the ME calculation by comparing to the nominal MG5\_AMC@NLO+PYTHIA8 sample.



**Table 4.2:** Summary of the nominal configurations used for the event generation of the signal and background processes using Monte Carlo simulations. The alternative samples used to estimate the systematic uncertainties are indicated in parenthesis. The inclusive cross-sections used in the normalization of each simulated sample is presented in the  $\sigma$  column. In the ME generator column the “order” in the strong coupling constant of the perturbative calculation is indicated in parenthesis. The (“PDF set”) column indicates the Parton Distribution Function set used in the ME/PS. All samples include leading-logarithm photon emission, either modeled by the parton shower generator or by PHOTOS [109]. The masses of the top quark and SM Higgs boson are set to 172.5 GeV and 125 GeV respectively.

Process	$\sigma$ [pb]	ME Generator (order)	PS generator	PDF set (ME/PS)	Tune (PS)
$t\bar{t}H$	0.507 (0.507)	POWHEG (NLO) (POWHEG (NLO))	PYTHIA8 (HERWIG7)	NNPDF3.0 NLO/NNPDF2.3 LO (NNPDF3.0 NLO/MMHT2014 LO [110])	A14 (H7-UE-MMHT)
$t\bar{t}W$	0.721 (0.603)	SHERPA 2.2.1 (MEPs@NLO) (MG5_AMC@NLO (NLO))	SHERPA (PYTHIA8)	NNPDF3.0 NLO (NNPDF3.0 NLO/NNPDF2.3 LO)	Sherpa default (A14)
$t\bar{t}(Z/\gamma^*)$ (high-mass)	0.881	MG5_AMC@NLO (NLO)	PYTHIA8	NNPDF3.0 NLO/NNPDF2.3 LO	A14
$t\bar{t}(Z/\gamma^*)$ (low-mass)	0.039	MG5_AMC@NLO (NLO)	PYTHIA8	NNPDF3.0 NLO/NNPDF2.3 LO	A14
$t\bar{t} \rightarrow W^+bW^-\bar{b}\gamma^*$	0.394	MG5_AMC@NLO (LO)	PYTHIA8	NNPDF3.0 LO	A14
rare- $t\bar{t}$	(0.880)	(SHERPA 2.2.0 (LO))	(SHERPA)	(NNPDF3.0 NLO)	(Sherpa default)
$t\bar{t}$	832	POWHEG (NLO)	PYTHIA8	CT10/CTEQ6L1	Perugia2012
Diboson, Triboson	99, 0.014	SHERPA 2.2.2 (NLO)	SHERPA	NNPDF3.0 NLO	Sherpa default
$tH$	0.074	MG5_AMC@NLO (LO)	PYTHIA8	CT10 [111]	A14
$tHW$	0.015	MG5_AMC@NLO (NLO)	HERWIG++ [112]	CT10/CTEQ6L1 [104, 105]	UE-EE-5
$tt\bar{t}\bar{t}, t\bar{t}t$	0.009, 0.002	MG5_AMC@NLO (LO)	PYTHIA8	NNPDF3.0 LO	A14
$t\bar{t}W^+W^-$	0.01	MG5_AMC@NLO (LO)	PYTHIA8	NNPDF3.0 LO	A14
Single-top	70, 79, 3	POWHEG (NLO)	PYTHIA8	NNPDF3.0 NLO/NNPDF2.3 LO	A14
$t-$ , $Wt$ , $s$ -channel					
$t(Z/\gamma^*)$	0.24	MG5_AMC@NLO (LO)	PYTHIA6 [113]	CTEQ6L1	Perugia2012
$tW(Z/\gamma^*)$	0.016	MG5_AMC@NLO (NLO)	PYTHIA8	NNPDF3.0 LO	A14

## 4.2 Physics objects selections

The object selections used in this analysis are discussed in this section. These selections are applied to the surviving objects after the overlap removal procedure described in Section 3.5.

### 4.2.1 Lepton selection

For the analysis presented in this thesis, reconstructed electrons candidates are required to be identified with a *Tight* working point and satisfy the *Fix(Loose)* isolation criteria, described in Section 3.2.1. Reconstructed muon candidates are required to be identified with a *Medium* working point and satisfy the *Fix(Loose)* isolation criteria, described in Section 3.2.2.

In addition to these requirements, several selection criteria are imposed in order to suppress fake leptons originating from the sources discussed in Section 3.2.3. A detailed description of these criteria is given in the next sections.

### Suppression of CFFake electrons

Electrons with incorrectly assigned electric charge are suppressed using a multivariate discriminant in the form of a boosted decision tree (BDT) called **chargeIDBDTTight** [52].

The training of the BDT was done using several electron observables as input, of which  $p_T$  and  $\eta$  are the most sensitive. This is due to the fact that CFFake electrons are expected to concentrate at higher  $p_T$  and higher  $|\eta|$  (for higher  $|\eta|$  values, the electron track traverses more detector material, i.e. more  $X_0$  for bremsstrahlung). Additional variables cover the quality of the chosen primary electron track, combined tracking-calorimeter quantities and shower shape in the EMCal (i.e. a narrower cluster is expected for electrons that do not undergo bremsstrahlung).

The BDT output values are assigned in the range  $-1 \leq \text{chargeIDBDTTight} \leq +1$ . Values close to  $-1$  indicate “fake-like” electrons, while values closer  $+1$  correspond to electrons whose charge is most probably assigned correctly. In this thesis, only electrons with a **chargeIDBDTTight** score above 0.7 are used. This value corresponds to a factor 14 background rejection for a 95% signal acceptance. The **chargeIDBDTTight** cut was optimized together with the HDFake rejection BDT, which will be discussed in the next section.

Moreover, it was found that the efficiency at which electrons were selected for the analysis decreased rapidly as  $|\eta|$  increased. This efficiency loss is driven by the charge flip BDT requirement since, as  $|\eta|$  approaches the boundary of the inner detector coverage,

the correct charge assignment worsens. Therefore, an additional cut on  $|\eta| < 2.0$  is applied for all electrons. This requirement has a small impact on the signal acceptance ( $< 4\%$ ).

## Suppression of HDFake leptons

To suppress leptons originated in the in-flight decay of hadrons, strict requirements are applied to the longitudinal and transverse impact parameters associated with the lepton tracks. This is done in order to increase the chances of selecting only prompt leptons originated at the primary vertex. For electron tracks it is required that  $|z_0 \cdot \sin(\theta)| < 0.5 \text{ mm}$  and  $|d_0|/\sigma(d_0) < 5$ , while muon tracks must satisfy  $|z_0 \cdot \sin(\theta)| < 0.5 \text{ mm}$  and  $|d_0|/\sigma(d_0) < 3$ . These requirements are complemented by using a boosted decision tree (BDT) discriminant called **PromptLeptonVeto** (PLV) [114].

The PLV discriminant exploits the fact that HDFake leptons come mainly from heavy  $b$ - or  $c$ -hadron decays. These particles have relatively large lifetime compared to other hadrons and will present a characteristic displaced decay vertex (see Section 3.3.3). Therefore, a lepton associated with the displaced vertex corresponding to one of such hadrons is most probably fake. Hence, PLV uses a similar approach to the ATLAS flavor tagging algorithms. It uses tracking information in order to correctly identify the displaced vertex and evaluate the likelihood of the lepton track to originate from it. In addition, calorimeter and track-based isolation criteria are used, due to the fact that HDFake leptons are typically not well isolated.

The combination of displaced vertex and isolation requirements offer an advantage over fixed-cut isolation working points, which may fail to reject HDFake leptons mainly because of two reasons:

- The HDFake lepton can have a significant energy fraction of the initial hadron energy and, therefore, it would appear to be isolated due to small calorimeter activity surrounding it.
- The decay direction of the HDFake lepton may be separated from the rest of the decay products and does not fall inside the isolation variable cone.

The PLV BDT training is performed on a set of leptons selected from a simulated  $t\bar{t}$  sample where both  $W$  bosons from top decay hadronically ( $t\bar{t} \rightarrow b\bar{b}W^+W^- \rightarrow b\bar{b}q\bar{q}'q''\bar{q}'''$ ). This means that the selected leptons will most probably correspond to a HDFake lepton. Similar to the charge flip discriminant, a PLV score in the range  $-1 \leq \text{PLV} \leq +1$  is assigned. Values close to  $-1$  indicate more “prompt-like” leptons, while values closer  $+1$  correspond to “fake-like” leptons.

In this thesis, a PLV score cut below  $-0.7$  ( $-0.5$ ) is used for electrons (muons). These values were optimized to yield the best  $t\bar{t}HML$  analysis sensitivity in terms of  $t\bar{t}H$  signal over HDFakes background ratio [115].

The PLV efficiency, at the chosen working point, for electrons (muons) satisfying the calorimeter and track-based isolation criteria is about 65% (80%) for  $p_T \sim 20$  GeV and reaches a plateau of 90% (95%) at  $p_T \sim 45$  GeV. The corresponding rejection factor against HDFake electrons (muons) is about 10 (3.5) [115].

## Suppression of ICFake/MCFake electrons

In order to reject ICFake/MCFake electrons, additional requirements that improve the recognition of electrons versus photon candidates are used. These requirements are centrally provided by the ATLAS  $e/\gamma$  performance group through a tool called  *$e/\gamma$ -ambiguity resolution* [54]. It uses track and calorimeter observables to evaluate the likelihood of a certain electron/photon candidate to be originated from a reconstructed conversion vertex. For this analysis, the most strict  $e/\gamma$ -ambiguity resolution criteria is applied. As a result, “higher quality” electrons are selected, i.e. reconstructed from EMCal clusters matched to a single good-quality track and not associated with any reconstructed photon conversion vertex.

However, in the case of ICFake electrons, two features of the ATLAS reconstruction scheme have been identified that allow them to pass this requirement:

- Conversion vertices with two associated Silicon tracks with a radius<sup>1</sup> of less than 20 mm are not reconstructed.
- Converted photon candidates<sup>2</sup> where one track has a hit on the innermost Silicon layer and the other does not (where a hit is expected) are considered electrons.

In those cases, the following variables have been found to have a powerful discrimination between ICFake, MCFake, and prompt electrons: the conversion radius, the invariant mass of the track associated to the electron and its closest track (originating from the conversion) calculated at conversion vertex ( $m_{trk-trk, CV}$ ), and the same invariant mass calculated at the primary vertex ( $m_{trk-trk, PV}$ ).

It has found by [115] that ICFake electrons are characterized by a conversion radius smaller than 20 mm. Furthermore, if an electron candidate (with two associated opposite-sign tracks) does not come from a conversion vertex reconstructed within a radius of 20 mm, the invariant mass of the tracks is calculated with respect to the PV instead. In those cases, candidates with  $0 < m_{trk-trk, PV} < 100$  MeV are mostly ICFakes. On the other hand, MCFake electron candidates are associated with opposite sign tracks corresponding to conversion vertices with  $r > 20$  mm and are concentrated in the region

---

<sup>1</sup>The vertex radius is defined as the distance of the vertex in the  $x-y$  plane from the origin of the ATLAS coordinate system.

<sup>2</sup>A converted photon is defined as a EMCal cluster matched to a conversion vertex (or vertices).

$0 < m_{trk-trk, CV} < 100$  MeV. Therefore, in addition to the identification and isolation criteria described so far (including the additional PLV and charge flip discriminant cuts), all electron candidates must *not* fulfill any of the following definitions:

- **Material conversion candidate:** when a conversion vertex is found with radius  $r > 20$  mm, and the mass of the vertex is  $0 < m_{trk-trk, CV} < 100$  MeV.
- **Internal conversion candidate:** when it is not an Material conversion candidate and  $0 < m_{trk-trk, PV} < 100$  MeV.

A summary of all lepton selections used in this analysis is presented in Table 4.3. Throughout the rest of this thesis, these requirements will be referred to as *strict lepton definitions*.

**Table 4.3:** Strict lepton definitions used in this analysis. The isolation and identification working points used are defined in Section 3.2.

Selection criteria	$e$	$\mu$
Identification	<i>Tight</i>	<i>Medium</i>
Isolation	<i>Fix (Loose)</i>	
charge flip BDT cut	$> 0.7$	-Not required-
PLV BDT cut	$< -0.7$	$< -0.5$
$e/\gamma$ ambiguity resolution	Yes	-Not required-
$d_0/\sigma(d_0)$	$< 5$	$< 3$
$ z_0 \cdot \sin(\theta) $	$< 0.5$ mm	
$\gamma$ conversion suppression	Neither ICFake nor MCFake candidate (see Section 4.2.1)	-Not required-

## 4.2.2 Jet selection

In order to suppress the contamination of jets originating from pileup interactions, an algorithm based on association of jet tracks to the hard-scattering vertex known as Jet Vertex Tagger (JVT) [116] is used for all reconstructed jets with  $p_T < 60$  GeV and  $|\eta| < 2.4$ . The efficiency of the JVT algorithm is 92% (i.e., 92% of non-pileup jets survive the cut). This efficiency is determined as a function of the jet  $p_T$  in data and simulated  $Z \rightarrow \mu^- \mu^+ + jets$  events and the ratio is used as a correction scale factor for simulations. In this analysis, correction scale factors in the order of 1 – 5% are used.

In terms of  $b$ -tagging, this analysis uses only  $b$ -jets that have been selected by a fixed cut in the MV2c10 discriminant corresponding to a  $b$ -tagging efficiency of 70% (see Table 3.1).

## 4.3 Selection of $t\bar{t}H$ signal events

The following event selections are commonly applied to both  $2\ell SS$  and  $3\ell$  channels in this analysis. Further channel-specific selections targeting each individual channel phase-space will be detailed in Sections 4.3.1 and 4.3.2.

All selected events are required to have at least one reconstructed hard scattering vertex, from which the PV is identified as described in Section 3.1. Data events are required to pass the di-lepton trigger criteria discussed in Section 4.1.2 and the leptons that triggered the event must have been correctly reconstructed and identified. Events containing hadronically decaying taus ( $\tau_{had}$ ) are vetoed.

### 4.3.1 Signal selection in the $2\ell SS$ channel

Events in the  $2\ell SS$  channel are required to have exactly two same-sign leptons, each within  $|\eta| < 2.5$  ( $|\eta| < 2.0$  for electrons) and having  $p_T > 20$  GeV. Both leptons are required to pass the strict lepton definition requirements summarized in Table 4.3.

The same-sign requirement is used to ensure that the selection picks one lepton from the Higgs decay chain and the other from the  $t\bar{t}$  system. This way, background events such as di-leptonic  $t\bar{t}$  (i.e.  $t\bar{t} \rightarrow W^+bW^+\bar{b} \rightarrow b\bar{b}\ell^+\ell^-\nu\bar{\nu}$ ) and events containing leptonically decaying resonances (e.g.  $Z \rightarrow \ell^+\ell^-$ ,  $J/\Psi \rightarrow \ell^+\ell^-$ ) can be suppressed.

An example of a typical  $2\ell SS$  channel final state is depicted in Figure 4.3 (a). Note that at least six jets are expected in this final state (two  $b$ -jets from the decay of the  $t\bar{t}$  system and four additional jets initiated by the quarks produced in the decay of W bosons from Higgs and top decay). However, at least four jets are required in the  $2\ell SS$  channel (including  $b$ -jets) in order to account for possible acceptance effects. For example, it may happen that three W bosons decay leptonically and one of the leptons is not reconstructed. In such case, the  $t\bar{t}H$  final state would have only four jets.

Similarly, at least two  $b$ -jets are expected from this final state. However, the  $b$ -tagging algorithm can mis-identify one of them as a jet with different flavor. Thus, only one of the selected jets is required to be  $b$ -tagged. All jets are required to have  $p_T > 25$  GeV and  $|\eta| < 2.5$ . A summary of the  $2\ell SS$  channel selections is presented in Table 4.4.

### 4.3.2 Signal selection in the $3\ell$ channel

Events in the  $3\ell$  channel are required to have exactly three leptons within  $|\eta| < 2.5$  ( $|\eta| < 2.0$  for electrons). The total charge in the event must be  $\pm 1$ , which means that one of the leptons must have an electric charge of opposite-sign to the other two. This lepton will be referred to as  $lep0$  in the following. The remaining two (same-sign) leptons will be called  $lep1$  and  $lep2$ , where  $lep1$  is closer to  $lep0$ , i.e.  $\Delta R[lep0, lep1] < \Delta R[lep0, lep2]$ .

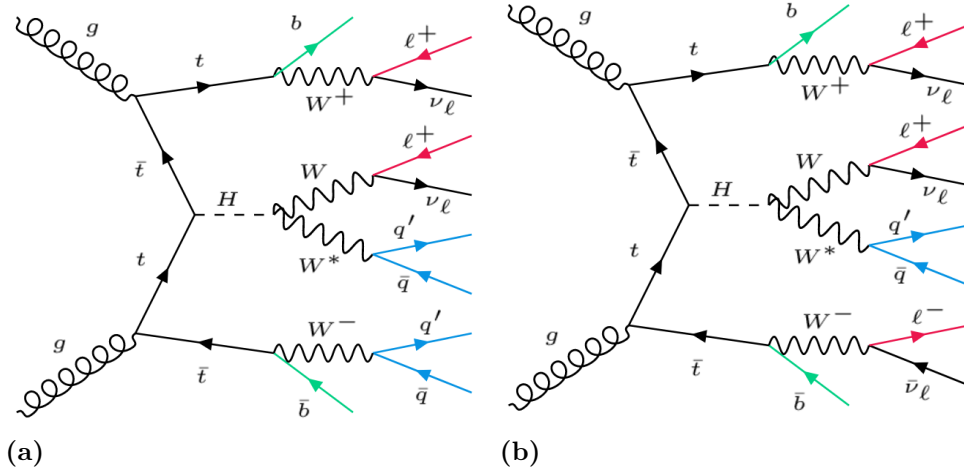


**Figure 4.3:** Feynman diagram representing typical  $2\ell SS$  (a) and  $3\ell$  (b) channel final states with  $H \rightarrow WW^*$ . The letters  $q$  and  $\ell$  are used to represent quarks and leptons respectively. The selected leptons in each channel are highlighted in red. Bottom quarks from top decay that originate  $b$ -jets are colored in green, while quarks of any flavor (in the case of the  $Z$  boson decay,  $q$  can be a  $b$ -quark) are colored in blue.

Both  $lep1$  and  $lep2$  must satisfy the strict lepton definition requirements of Table 4.3 and have  $p_T > 15$  GeV. On the other hand,  $lep0$  only has to pass the *Fix* (*Loose*) isolation criteria and  $p_T > 10$  GeV. The reason for this difference is that, for events where  $lep1$  and  $lep2$  pass the strict lepton definition requirements,  $lep0$  is rarely a fake. Figure 4.3 (b) shows an example of a typical  $3\ell$  channel final state.

In order to suppress background from resonances that can decay into a pair of opposite-sign leptons with same flavor (e.g.  $J/\Psi \rightarrow \ell^+\ell^-$ ), all events where the invariant mass of such pairs is below 12 GeV are vetoed. Furthermore, to avoid potential background from events with  $Z \rightarrow \ell^+\ell^-\gamma^* \rightarrow \ell^+\ell^-\ell'^+\ell'^-$ , where one lepton (e.g.  $\ell'^-$ ) has low momentum and is not reconstructed, the invariant mass of the three remaining leptons must satisfy  $|m_{3\ell} - 91.2| > 10$  GeV. Events where any pair of opposite-sign same flavor leptons have  $|m_{\ell+\ell^-} - 91.2| > 10$  GeV are removed in order to reject  $t\bar{t}Z$  background. Similarly, events containing converted photons are further rejected by requiring that  $\Delta R_{\ell+\ell^-} < 0.5$ , since it is expected that converted photons will produce same flavor electrons that are close to each other.

The jet multiplicity selection follows the same argument presented for the  $2\ell SS$  channel except that now, since three leptons are required, one more  $Z/W$  boson has to decay leptonically, leading to two jets less in the event. Therefore, the number of jets per event is required to be at least two, of which at least one must have been identified as a  $b$ -jet. All jets must have  $p_T > 25$  GeV and  $|\eta| < 2.5$ .

A summary of the  $3\ell$  channel selections is presented in Table 4.4. When applying these selections to simulated  $t\bar{t}H$  events, the contribution fraction from the three Higgs



decay modes used in this analysis is shown in Figure 4.4.

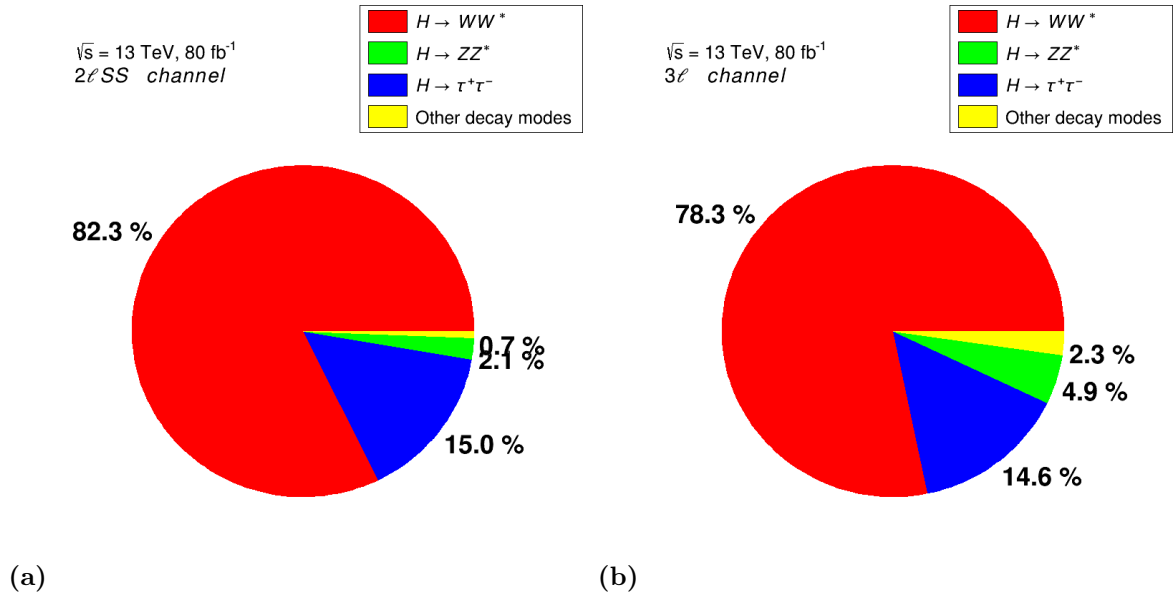


**Figure 4.4:** Contribution of each Higgs decay mode after applying the selections for (a)  $2\ell SS$  and (b)  $3\ell$  channels in  $t\bar{t}H$  simulated events.

**Table 4.4:** Summary of the event selection for the  $2\ell SS$  and  $3\ell$  channels used in this analysis.

Channel	Events selection
$2\ell SS$	– Exactly 2 same-sign leptons with $p_T > 20$ GeV, within $ \eta  < 2.5$ ( $ \eta  < 2.0$ for electrons) and passing the strict lepton definitions of Table 4.3.
	– At least 4 jets with $ \eta  < 2.5$ and $p_T > 25$ GeV, of which at least 1 must be a $b$ -jet with 70% efficiency working point
	– Events with $\tau_{had}$ are vetoed
$3\ell$	– Exactly 3 leptons (two of them with same-sign) within $ \eta  < 2.5$ ( $ \eta  < 2.0$ for electrons) <ul style="list-style-type: none"> <li>◦ The same-sign leptons must have <math>p_T &gt; 15</math> GeV and satisfy strict lepton definitions of Table 4.3</li> <li>◦ The opposite-sign lepton must have <math>p_T &gt; 10</math> GeV and pass only the <i>Fix (Loose)</i> isolation criteria</li> </ul>
	– At least 2 jets with $ \eta  < 2.5$ and $p_T > 25$ GeV, of which at least 1 must be a $b$ -jet with 70% efficiency working point
	– $ m_{\ell^+\ell^-} - 91.2  > 10$ GeV, $\Delta R_{\ell^+\ell^-} < 0.5$ and $m_{\ell^+\ell^-} < 12$ GeV for any opposite-sign same flavor lepton pair and $ m_{3\ell} - 91.2  > 10$ GeV
	– Events with $\tau_{had}$ are vetoed

## 4.4 Background processes

In this analysis, two distinctive types of backgrounds can be identified:

- (i) *Backgrounds containing fake leptons*: This type of background is characterized by the presence of fake leptons that are mis-identified as prompt, allowing the event to



pass the  $t\bar{t}H$  signal selections. The estimation of background events containing fake leptons is presented in Section 4.4.1.

- (ii) *Background from other physics processes*: A background event of this type stems from a different physics process than  $t\bar{t}H$  but contains real prompt leptons in the final state. This characteristic makes them difficult to reject without a significant loss in signal events. A description of this type of background and its estimation is discussed in Section 4.4.2.

### 4.4.1 Backgrounds containing fake leptons

The Backgrounds containing fake leptons are estimated separately depending on the type of fake lepton they contain, as described in Section 3.2.3. In the following paragraphs, the procedure used to estimate the contribution from these type of events is described.

#### HDFake ( $e/\mu$ ), MCFake and ICFake events.

Events containing fake leptons coming from hadron decays or photon conversions are estimated using a novel semi-data-driven technique that uses simulated samples to build background categories for each fake type. The information about the origin of the fake leptons, available in the simulated sample records, allows to allocate each events into a particular category. Once this is done, the size of the contribution for each fake category is adjusted using a normalization factor extracted from a likelihood fit to data (these factors are extracted simultaneously with the  $t\bar{t}W$  and  $t\bar{t}H$  normalization).

Given the event selections defined in Sections 4.3.1 and 4.3.2, the  $t\bar{t}$  process produces most of the fake events in each of these categories. In this process, HDFake electrons and muons are primarily produced in the decay of  $b$ -hadrons, while MCFake/ICFake electrons are produced by photons coming from initial or final state radiation (modeled by the parton shower as described in Section 4.1.3). Additional contributions to these fake event categories come from *single-top*,  $Z/W + jets$  and  $Z/W + \gamma$  events with additional QCD radiation. The HDFake ( $e/\mu$ ) and MCFake categories are constructed by combining the contributions from all these processes. The ICFake category is estimated only with  $t\bar{t}$  events since the contribution from other processes was found to be negligible. Table 4.5 shows the contribution of each process considered for the fake background modeling per channel.

**Table 4.5:** Event yields for HDFake ( $e/\mu$ ), MCFake and ICFake events estimated from simulated  $t\bar{t}$ , *single-top*,  $Z/W + jets$  and  $Z/W + \gamma$  processes in each channel.

$t\bar{t}HML$ channel	Fake type	Processes contributing				
		$t\bar{t}$	<i>single-top</i>	$Z/W + jets$	$Z/W + \gamma$	Total
$2\ell SS$	HDFake ( $e$ )	38.6	1.1	0.8	0	40.5
	HDFake ( $\mu$ )	91.0	1.6	1.5	0	94.1
	MCFake	7.2	0.1	0.2	2.0	9.5
	ICFake	12.4	—	—	—	12.4
$3\ell$	HDFake ( $e$ )	16.8	1.0	0.2	0	18.0
	HDFake ( $\mu$ )	45.1	2.0	4.8	0	51.9
	MCFake	4.4	0.3	1.4	0.6	6.7
	ICFake	8.1	—	—	—	8.1

### CFFake events.

Background events containing electrons with wrong reconstructed charge in the  $2\ell SS$  channel come mostly from dilepton  $t\bar{t}$  events ( $t\bar{t} \rightarrow bW^+\bar{b}W^- \rightarrow b\nu_e e^+ \bar{b}\bar{\nu}_e e^-$ ), where one of the electrons flips charge. In the  $3\ell$  channel, a charge flip that does not modify the  $\pm 1$  total charge requirement has no impact on the selection of the event. Thus, by construction, CFFake events are not present in the  $3\ell$  channel.

The CFFake background contribution in  $2\ell SS$  is estimated in a two-step process, purely data-driven. In the first step, the relationship between the number of same-sign and opposite-sign electron pairs ( $\frac{N_{SS}}{N_{OS}} = \omega_{CFFake}$ ) in a  $Z \rightarrow e^-e^+$  data sample is determined. This is done by first computing the fraction of events containing two same-sign and same-flavor (SSSF) electrons with invariant mass close to the mass of the Z boson:

$$\frac{N_{SS}}{N_{SS} + N_{OS}} = \epsilon_i(1 - \epsilon_j) + \epsilon_j(1 - \epsilon_i) = \epsilon_i + \epsilon_j - 2\epsilon_i\epsilon_j \quad (4.1)$$

where  $N_{SS}$  ( $N_{OS}$ ) is the number of same-sign (opposite-sign) electron pairs in  $Z \rightarrow e^-e^+$  events and  $\epsilon_i$  ( $\epsilon_j$ ) is the probability of the leading (sub-leading) lepton being the one with flipped charge. The rates  $\epsilon_i$  and  $\epsilon_j$  are determined from a likelihood fit on a binned distribution of the invariant mass of the  $e^-e^+$  pair assuming that this fraction follows a Poisson distribution with an expectation value of  $(N_{SS} + N_{OS}) \cdot (\epsilon_i + \epsilon_j - 2\epsilon_i\epsilon_j)$ . From Equation 4.1, the number of same-sign events can be calculated by solving for  $N_{SS}$ , which leads to:

$$N_{SS} = \left( \frac{\epsilon_i + \epsilon_j - 2\epsilon_i\epsilon_j}{1 - \epsilon_i - \epsilon_j + 2\epsilon_i\epsilon_j} \right) \cdot N_{OS} \quad (4.2)$$

where  $\left( \frac{\epsilon_i + \epsilon_j - 2\epsilon_i\epsilon_j}{1 - \epsilon_i - \epsilon_j + 2\epsilon_i\epsilon_j} \right) = \omega_{CFFake}$ .

The second step consists in obtaining the number of CFFake background events for

the analysis, which is done by applying  $\omega_{CFFake}$  as a per-event weight to a special data sample. This sample is constructed using the same selection of the  $2\ell SS$  channel, but inverting the charge requirement, i.e. only opposite-sign leptons ( $2\ell OS$ ) are selected. For events where only one of the two leptons is an electron, the CFFake event weight is recalculated by setting  $\epsilon_j$  or  $\epsilon_i$  to zero (depending on whether the leading or sub-leading lepton is an electron) and apply it to  $2\ell OS$  data events.

#### 4.4.2 Background from other physics processes

The biggest background contribution from other physics processes in both  $2\ell SS$  and  $3\ell$  channels come from  $t\bar{t}W$ ,  $t\bar{t}(Z/\gamma^*)$  and Diboson processes. The  $t\bar{t}W$  and  $t\bar{t}(Z/\gamma^*)$  events have similar final state to  $t\bar{t}H$ . Moreover, they have bigger inclusive cross-sections [117, 118], which leads to large background contributions from these processes in both channels. In the case of Diboson processes, the inclusive production cross-section is a couple of orders of magnitude higher than  $t\bar{t}H$  [119–122]. However, due to the requirement of at least 4 (2) jets in the  $2\ell SS$  ( $3\ell$ ) channel, additional QCD radiation (i.e.  $g \rightarrow q\bar{q}$ ) would be necessary in Diboson processes. This effectively reduces the impact of the high inclusive cross-section.

Smaller contributions originate from the following processes:  $tZ$ ,  $tW$ ,  $tWZ$ ,  $t\bar{t}WW$ , Triboson, three tops ( $t\bar{t}t$ ), and four tops ( $t\bar{t}t\bar{t}$ ). The associated production of single top quarks with a Higgs boson,  $tH$ , contributes with at most 2% and other Higgs boson production mechanisms, such as  $WH$ ,  $ZH$ , and  $tWH$ , contribute negligibly ( $< 0.2\%$ ). In the following, these processes are combined in a single category called *Other*.

The contribution from all background processes discussed so far is estimated from MC simulation using the corresponding samples described in Section 4.1.3. In particular, the  $t\bar{t}W$  background is adjusted using a normalization factor derived from a fit to data.

A summary of the event yields for the data, signal and backgrounds in the  $2\ell SS$  and  $3\ell$  channels is presented in Table 4.6. As shown, there is over 30% more data in the  $2\ell SS$  channel with respect to the  $3\ell$ . However, both channels have similar signal over background ratio (S/B) of  $\sim 12\%$ . The dominant background process in the  $2\ell SS$  channel is  $t\bar{t}W$  with 45% of the total background prediction. In the case of the  $3\ell$  channel, both  $t\bar{t}W$  and  $t\bar{t}(Z/\gamma^*)$  dominate with 27% and 28% of the total background prediction respectively. In both channels, the most significant contribution from events containing fake leptons are those with muons produced in hadron decays (HDFake ( $\mu$ )).

### 4.5 Event categorization

In order to simultaneously extract the  $t\bar{t}H$  signal strength and normalization factors for selected backgrounds (i.e.  $t\bar{t}W$ , HDFakes ( $e/\mu$ ), MCFakes and ICFakes) from the

**Table 4.6:** Event yields for the data,  $t\bar{t}H$  and background processes selected in the  $2\ell SS$  and  $3\ell$  channels. The contribution from all physics processes, except  $CFFake$  (data-driven), has been estimated using MC simulated samples (see Table 4.2).

Process	$2\ell SS$	$3\ell$
$t\bar{t}W$	261.2	90.9
$t\bar{t}(Z/\gamma^*)$	91.3	93.0
<i>Diboson</i>	31.0	35.7
<i>HDFake</i> ( $e$ )	40.5	18.0
<i>HDFake</i> ( $\mu$ )	94.1	51.7
<i>MCFake</i>	9.5	6.7
<i>ICFake</i>	12.4	8.1
<i>CFFake</i>	2.8	—
<i>Other</i>	35.5	30.0
Total background	578.6	334.3
$t\bar{t}H$	83.1	46.0
Total prediction	661.7	380.3
<i>Data</i>	742.0	442.0

likelihood fit, all selected events are further split into different categories. Each event can only enter a single category. The goal is to define phase-space regions with high  $t\bar{t}H$  signal purity, called *Signal Regions* (SR), and regions where a specific background process of interest dominates, called *Control Regions* (CR). Signal regions are defined as those regions where the ratio of signal to background events is above 15%. Each region must contain enough events to be statistically significant in the fit.

The categorization is implemented as cuts on observables that offer the best discrimination power for the signal or background of interest against the rest of the processes (i.e. using a *cut-based* approach). This constitutes the focus of this thesis and my main contribution to the published  $t\bar{t}HML$  search. Alternatively, a multivariate-based categorization analysis has been performed in ATLAS using  $80 \text{ fb}^{-1}$  [115].

By using the cut-based approach, the results derived from this analysis could be cross-checked and reproduced easily by other groups (e.g., theorists or other experiment collaborations). This offers an advantage over the highly complex multivariate-based categorization. In the previously published  $t\bar{t}HML$  analysis, the precision of the cut-based method was limited by the amount of available events corresponding to  $36.1 \text{ fb}^{-1}$  of collected data [123]. However, with the  $80 \text{ fb}^{-1}$  used in this analysis, the cut-based precision is expected to improve significantly. Nevertheless, the overall cut-based analysis sensitivity is still expected to be reduced in comparison to the multivariate-based categorization analysis.

For the  $2\ell SS$  and  $3\ell$  channels, the categorization is done in such a way that the entire phase-space in each channel is covered. In addition, six CR enriched in events containing fake leptons are used. Events populating these regions are not originally included in the

phase-space defined by the selection of Table 4.4. Instead, they are selected by modifying some of the requirements described there in order to increase the contribution of each fake event type in these dedicated regions. This is done in such a way that each new region phase-space is kept orthogonal to the rest. In the following sections, a more detailed description of the region definitions used in this analysis will be given.

### 4.5.1 Fake-dominated event categories.

Two of the six fake-dominated CRs are defined in such way that the largest fraction of events correspond to those containing a HDFake electron or muon respectively. In order to enhance the acceptance for such events, the selections applied in those regions correspond to the  $2\ell SS$  channel cuts but requiring only two or three jets instead of four. This is motivated by the fact that most of the HDFake events are originated by  $t\bar{t}$  events where a fake lepton is produced in the in-flight decay of  $b$ -hadrons. The  $t\bar{t}$  events have, on average, lower jet multiplicity than  $t\bar{t}H$ , which contain additional W or Z bosons that may decay hadronically. These two CRs will be referred to as “ $low-N_{jets}(e)$ ” and “ $low-N_{jets}(\mu)$ ” in the following.

The  $low-N_{jets}(e)$  CR will contain those events where the subleading lepton is an electron, while the  $low-N_{jets}(\mu)$  CR will contain those with subleading muons. The event composition of these two regions is shown in the first two bins of Figure 4.5. Events containing HDFake electrons in the  $low-N_{jets}(e)$  region represent almost 30%, while the events containing HDFake muons represent approximately the 40% in the  $low-N_{jets}(\mu)$  region.

The high event yields of the  $low-N_{jets}$  CRs allow to fit differential distributions in them instead the total event yields. Effectively, this means that those bins are subdivided into finer bins of a given observable in order to profit from the additional separation power. The selected observable was the scalar sum of the leptons  $p_T$  ( $HT_{lep}$ ), which has very good separation power between HDFake ( $e/\mu$ ) and the rest of the backgrounds, specially  $t\bar{t}W$  (see Figure 4.6).

The remaining four fake-dominated CRs are defined to be enriched in events containing ICFake or MCFake electrons for both the  $2\ell SS$  and  $3\ell$  channels. In order to do this, the fake suppression criteria based on  $m_{trk-trk, CV}$ ,  $m_{trk-trk, PV}$  and the conversion radius of the fake electrons (discussed in Section 4.2.1), are removed. The event composition in each of these regions is shown in the last four bins of Figure 4.5. In the  $2\ell SS$  material (internal) conversion CR, events containing MCFake (ICFake) electrons represent a 32% (63%). In the  $3\ell$  channel these events represent a 29% (85%). Furthermore, the  $2\ell SS$  material conversion CR also presents a large fraction of CFFake events ( $\sim 42\%$ ). This is caused by an increased acceptance of  $t\bar{t}$  events (which is the main source of CFFakes) due to the low jet multiplicity requirement.

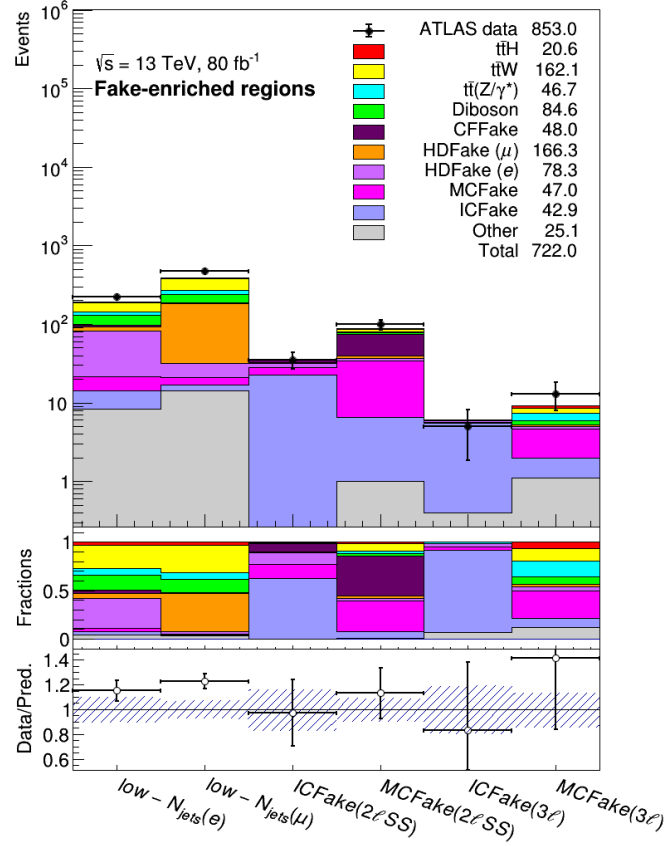


**Figure 4.5:** Fake-dominated control regions used in the analysis. The first ratio pad contains the event fractions for each process according to predictions. The second ratio pad contains the comparison of signal and background predictions to data, and the error band correspond to the total (stat.+syst.) uncertainty on the predictions. The sources of systematic uncertainty used here will be discussed in detail in Section 4.6.3.

### 4.5.2 $2\ell SS$ channel categories.

For the  $2\ell SS$  channel additional requirements are imposed on the standard selection described in Section 4.3.1 in order to define 8 event categories (regions) based on the following observables:

**Total number of jets ( $N_{jets}$ ).** Two categories are defined: events with  $N_{jets} = 4$  or events with  $N_{jets} \geq 5$ . This separation exploits the large jet multiplicity of the signal events with respect to other backgrounds, in particular,  $t\bar{t}W$ .

**Total number of  $b$ -jets ( $N_{b-jets}$ ).** Each category defined using the  $N_{jets}$  is subdivided into two additional categories with  $N_{b-jets} = 1$  or  $N_{b-jets} \geq 2$ . This requirement offers good separation between  $t\bar{t}$  processes (fakes) and  $t\bar{t}W$ .

**Total charge of the event.** All categories defined using  $N_{jets}$  and  $N_{b-jets}$  are further split into “++” or “--” events, according to both leptons being positively

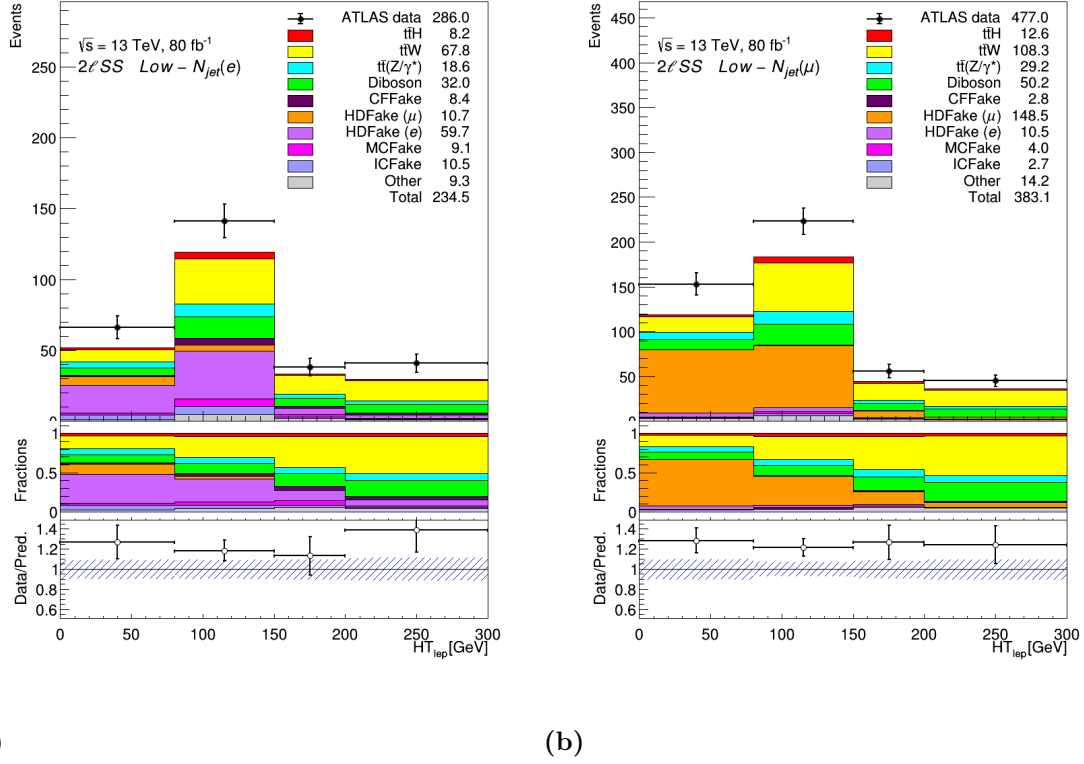


**Figure 4.6:** Scalar sum of the leptons  $p_T$  ( $HT_{lep}$ ) distributions used in the (a)  $low-N_{jets}(e)$  and (b)  $low-N_{jets}(\mu)$  regions. Events containing a HDFake electrons or muons are concentrated towards low  $HT_{lep}$ . The uncertainty band in the ratio plot includes the total systematic uncertainties. The errors on the data points correspond to the statistical uncertainty.

or negatively charged respectively. Regions defined in this way exploit the charge asymmetry of the  $t\bar{t}W$  process (i.e.  $t\bar{t}W^+$  cross-section is approximately twice as big as the  $t\bar{t}W^-$  cross-section) in order to better separate it from other backgrounds and the  $t\bar{t}H$  signal.

Figure 4.7 shows the data and MC contributions in the eight  $2\ell SS$  event categories, where the relative fractions of the different backgrounds can be seen in the first ratio pad. The comparison between data and predictions for each region is shown in the second ratio pad.

The region with highest signal purity is  $5j2b(--)$  with  $S/B = 28\%$ . Furthermore, regions containing the highest fraction of fake events are found with only one  $b$ -jet. One possible reason for this is that the fake lepton in these events actually corresponds to a HDFake coming from the decay of a  $b$ -hadron that produces a jet which is not  $b$ -tagged. In order to survive the strict lepton definitions, such HDFake lepton would have to be well isolated, which means that it would have to be outside the jet cone.

Regions with at least two  $b$ -jets are dominated by  $t\bar{t}W$  events. Similarly,  $t\bar{t}W$  events are enhanced in regions where both leptons are selected with positive charge with respect to those where they are selected with negative charge, reflecting the charge asymmetry of

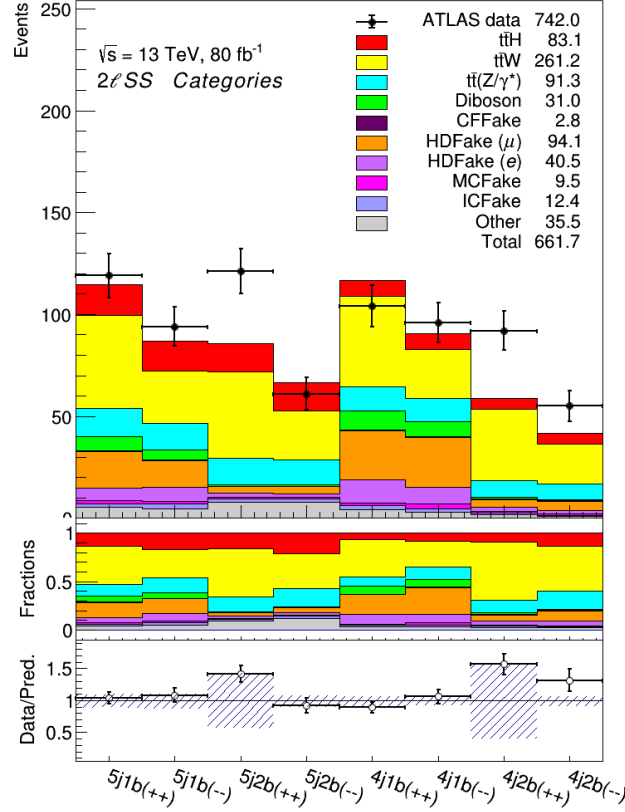


**Figure 4.7:** Events observed in the  $2\ell SS$  channel in different categories. The first ratio pad contains the event fractions for each process according to predictions. The second ratio pad contains the comparison of signal and background predictions to data and, the error band correspond to the total (stat.+syst.) uncertainty on the predictions.

the  $t\bar{t}W$  process. The  $t\bar{t}W$  background is found to be large across all regions, with relative fractions that range from  $\sim 27\%$  in  $4j1b(--)$  up to approximately 63% in  $4j2b(++)$ .

Moreover, predictions are found to underestimate data by  $>40\%$  in the regions containing  $2\ell SS$  events with at least two  $b$ -jets and both leptons being positively charged ( $4j2b(++)$  and  $5j2b(++)$ ). In fact, for the entire  $2b(++)$  phase-space (i.e. merging  $4j2b(++)$  and  $5j2b(++)$ ), the data was found to be slightly more than  $3\sigma$  away from the MC predictions. This motivated further studies to try to determine the origin of such discrepancies, which will be discussed in the following paragraphs.

## Study of the $2b(++)$ discrepancy

The first study was dedicated to see whether or not this difference depends on the lepton flavor, which may indicate an effect related to the lepton reconstruction. For this purpose, events were further split into “ $ee$ ” (both leptons in the event are electrons), “ $\mu\mu$ ” (both leptons are muons) or “ $OF$ ” (the selected leptons have opposite flavor, e.g.  $e\mu$ ). As shown



in Figure 4.8, the disagreement between data and MC predictions is independent of the lepton pair flavor.

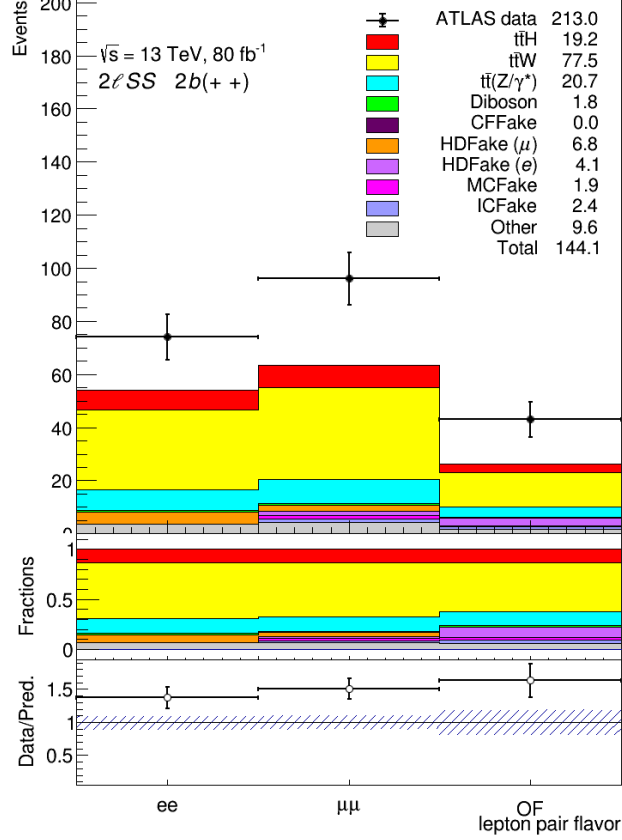


**Figure 4.8:** Number of  $2\ell SS$  events as a function of the flavor composition of the lepton pair in  $2\ell SS$  events selected with positively charged leptons, at least 4 jets and at least 2  $b$ -jets.

An additional study was performed to determine whether there was any mis-modeling of the fake background that would explain the observed  $2b(++)$  difference. This was done by comparing the number of selected events for data, signal and backgrounds in a fake-enriched phase-space as a function of the number of  $b$ -jets. Only events containing at least two  $b$ -jets and positively charged leptons are used. The fake-enriched phase-space is defined by eliminating the PLV requirement of Table 4.3 and, thus, relaxing the strict lepton isolation requirements. As shown in Figure 4.9, no significant discrepancies are found that could contribute to the observed discrepancy, given the small relative contributions of the fake background to the  $4j2b(++)$  and  $5j2b(++)$  regions.

The events containing only two or three jets ( $low-N_{jets}$ ), used in the HDFake control regions, were also investigated. In these events, differences between  $\mu\mu$  and  $ee$  events were observed when analyzing the longitudinal impact parameters of the tracks associated with both leptons. As shown in Figure 4.10 (a), for data events with at least two  $b$ -jets and

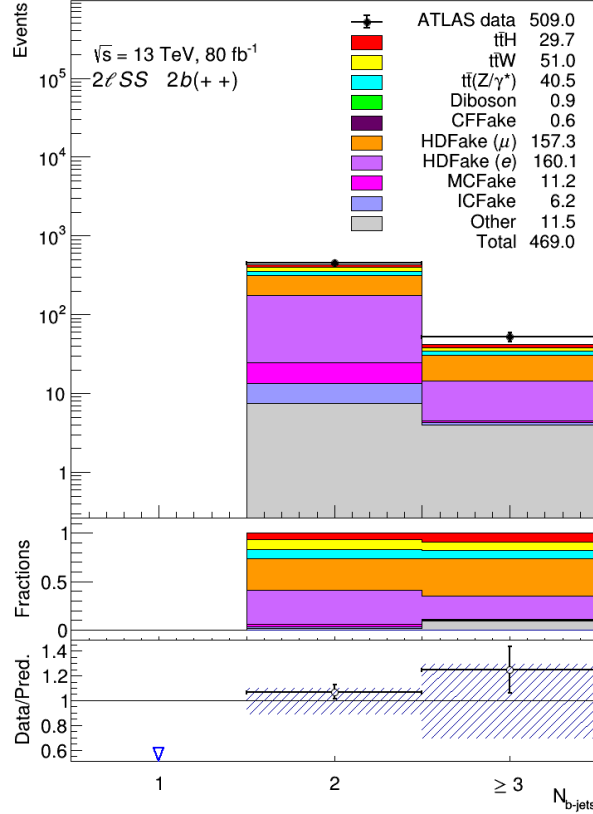


**Figure 4.9:** Number of  $2\ell SS$  events selected with at least 2  $b$ -jets and positively charged leptons as a function of the number of  $b$ -tagged jets. The PLV cut has been completely removed for these events.

two positively charged muons,  $\Delta z_0$  between the two muons presents a double-peak shape. This means that they do not originate from the same vertex, as it would be expected in the case of prompt muons. However,  $\Delta z_0$  in the MC predictions show the expected shape. This effect is not observed in data events containing negatively charged muons or electrons (Figure 4.10 (b) and (c)). Due to the low statistics observed in these studies, it cannot be excluded that the effect in Figure 4.10 (a) is due to a statistical fluctuation and hence, it was not possible to draw definitive conclusion on this particular effect.

The possibility of a missing background was also considered. However, no viable candidates with these characteristics were identified, that could produce high enough contribution in the  $4j2b(++)$  and  $5j2b(++)$  regions of the  $2\ell SS$  channel. Another possibility, is a large mis-modeling of backgrounds (other than fakes) already considered in the  $2b(++)$  phase-space. Since these regions are dominated mainly by  $t\bar{t}W$  events, a potential mis-modeling of this background might drive these observed discrepancies. However, this does not explain the fact that other  $2\ell SS$  regions with high relative fraction of  $t\bar{t}W$  events are very well described (e.g.  $5j1b(++)$ ). Nevertheless, the extraction of the  $t\bar{t}W$

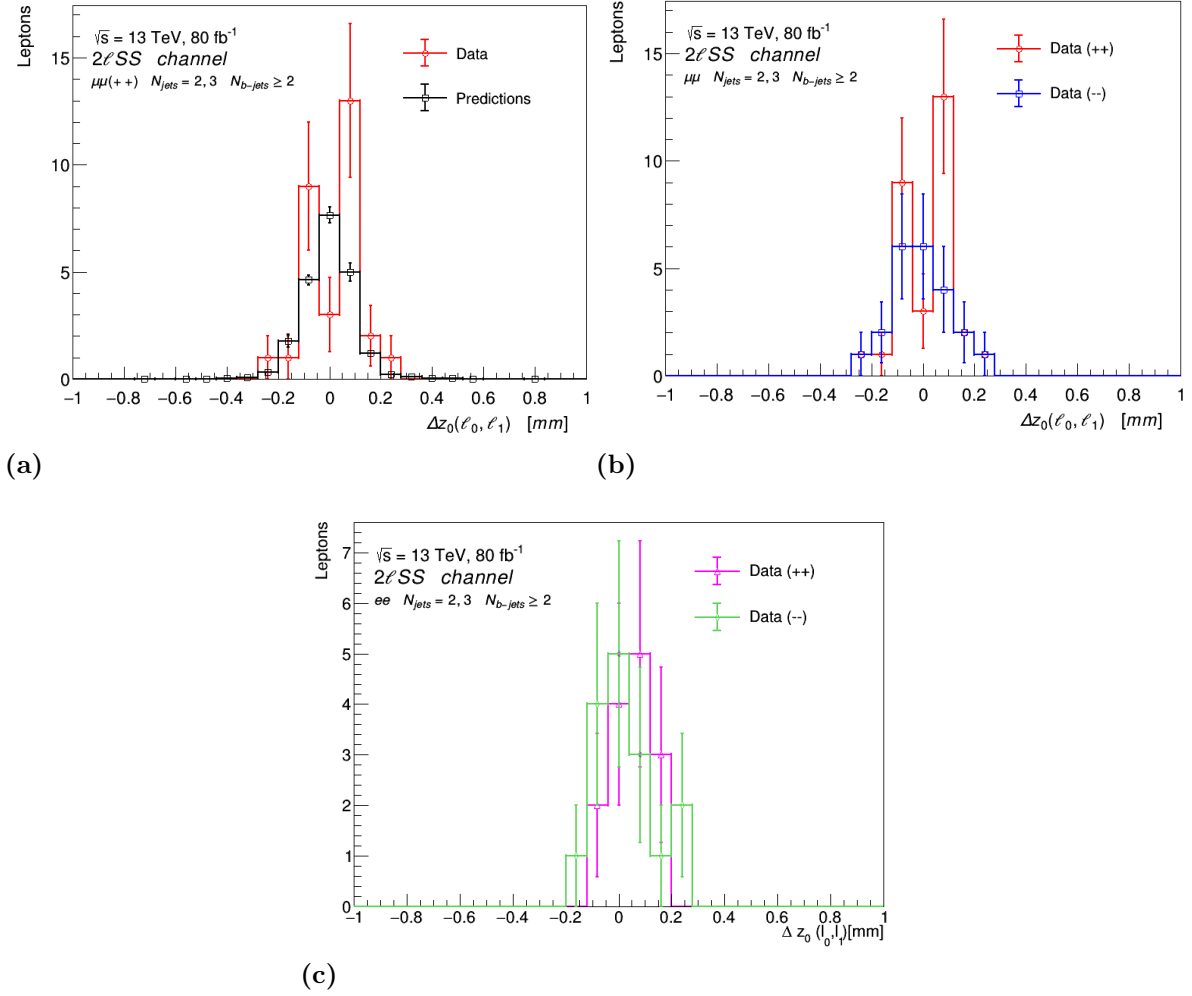


**Figure 4.10:** Number of  $2\ell SS$  events as a function of the longitudinal impact parameter difference ( $\Delta z_0$ ) of the two selected leptons. The distributions show (a) the comparison of data and MC predictions for events with two positively charged muons, (b) the comparison of data events selected with “++” or “--” muon pairs and (c) the comparison of data events selected with “++” or “--” electron pairs. All events are selected with only two or three jets.

normalization factor from the likelihood fit is expected to be influenced by the  $2b(++)$  discrepancy.

The potential influence of this effect on the final result will be discussed in the context of the fit in Sections 4.6.3 and 4.7.

### 4.5.3 $3\ell$ channel categories.

In the  $3\ell$  channel, 10 event categories are defined by applying cuts based on several observables. These categories are not formed by applying one cut on top of the previous one, as was the case in the  $2\ell SS$  channel. Instead, these cuts are applied in such a way that not all of the observables are used to define all categories. However, similar to the  $2\ell SS$  channel, the entire  $3\ell$  phase-space is covered without overlaps. The following observables

are used in the definition of the  $3\ell$  categories:

**Total number of jets ( $N_{jets}$ ).** The event categories that contain the  $N_{jets}$  cut are separated into two groups: a “Lj” (*low- $N_{jets}$* ) group with  $N_{jets} = \{2, 3, 4, 5\}$  and a “Hj” (*high- $N_{jets}$* ) group containing events with  $N_{jets} \geq 6$  to reduce the contribution from  $t\bar{t}W$  background.

**Invariant mass of  $lep0$  and  $lep1$ .** A cut on  $m_{l_0, l_1}$  is used in two groups of categories: a “Lm” (*low-mass*) group with  $m_{l_0, l_1} < 70$  GeV and a “Hm” (*high-mass*) group with  $m_{l_0, l_1} \geq 70$  GeV. This cut suppresses the  $t\bar{t}Z$  background in regions where the “Lm” is used.

**Total number of  $b$ -jets ( $N_{b-jets}$ ).** Two category groups are defined to separate  $t\bar{t}H$  from events containing fake leptons. A group of categories contain events with only one  $b$ -jet while another group contain those with at least two  $b$ -jets.

**Z-peak definition.** This defines two category groups: the “Zenr” (Z-enriched) categories contain events with opposite-sign same flavor (OSSF) lepton pairs with  $|m_{\ell\ell} - m_Z| > 10$  GeV; the “Zdep” (Z-depleted) categories contain events where no OSSF lepton pair is present. This categories are used to separate  $t\bar{t}H$  from  $t\bar{t}Z$  events.

**Electric charge sign of  $lep1$  and  $lep2$ .** This separation is only used on “Hm” and “Zdep” events to classify them as “++” or “--” (analogous to  $2\ell SS$ ), to reduce the  $t\bar{t}W$  background.

Figure 4.11 shows the data and MC contributions in the ten  $3\ell$  event categories, where the relative fractions of the different backgrounds can be seen in the first ratio pad. The comparison between data and predictions for each region is shown in the second ratio pad. High signal purity is obtained in some of the regions (up to  $S/B = 77\%$ ). However, the three regions with higher  $t\bar{t}H$  event fraction ( $HjLmZdep$ ,  $LjLm2bZdep$  and  $LjLm1bZdep$ ) suffer from limited statistics.

## 4.6 Statistical model description

The main goal of the analysis is to simultaneously extract the  $t\bar{t}H$  signal strength and several background normalization factors ( $t\bar{t}W$ , HDFakes ( $e/\mu$ ), MCFakes and ICFakes). This is done by performing a *profile likelihood fit* (PLF) to data across all the event categories defined in the previous sections. The PLF is based on the *maximum likelihood* (ML) method of parameter estimation for binned data, which will be discussed in Section 4.6.1. After that, a brief description of the statistical significance estimation method

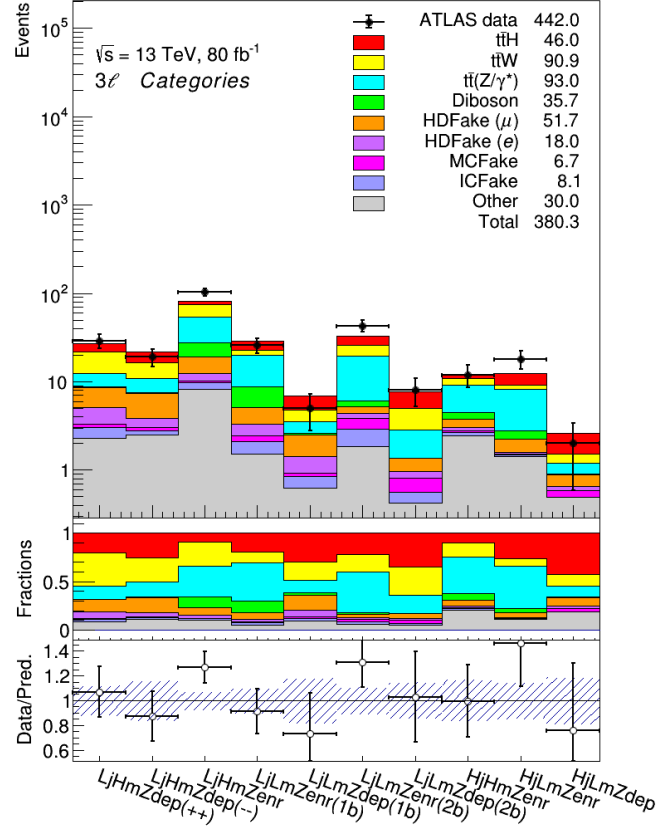


**Figure 4.11:** Events observed in the  $3\ell$  channel in different categories. The first ratio pad contains the event fractions for each process according to predictions. The second ratio pad contains the comparison of signal and background predictions to data and, the error band correspond to the total (stat.+syst.) uncertainty on the predictions.

will be given in Section 4.6.2. The treatment of systematic uncertainties in this analysis is discussed in Section 4.6.3. For the implementation of the PLF in this analysis, the `TRExFitter` [124] package was used.

### 4.6.1 The maximum likelihood method

Let  $\vec{x} = \{x_1, x_2, \dots, x_i, \dots, x_N\}$  be a set of  $N$  finite measurements of an observable  $x$  that are independently distributed with the same probability density function (pdf) given by  $f(x_i; \vec{\Theta})$ , where  $\vec{\Theta} = \{\theta_1, \theta_2, \dots, \theta_M\}$  is an ensemble of  $M$  parameters with unknown values. The method of maximum likelihood can be used to determine the values of the parameters  $\vec{\Theta}$  that best describe the observed  $\vec{x}$ . In order to achieve this, a so called *likelihood function* is defined as:

$$L(\vec{\Theta}) = \prod_{i=1}^N f(x_i | \vec{\Theta}) \quad (4.3)$$

The likelihood function can only be written as the product of the individual pdfs for  $x_i$  if they are independent of each other [125]. The set of parameters  $\vec{\Theta}$  that best describe the observed data are those that maximize the likelihood function:

$$\frac{\partial L(\vec{\Theta})}{\partial \theta_k} = 0, \quad k = 1, 2, \dots, M \quad (4.4)$$

These values are called *Maximum Likelihood Estimators* (MLE) of the set  $\vec{\Theta}$  and are denoted by hats,  $\hat{\vec{\Theta}} = \{\hat{\theta}_1, \hat{\theta}_2, \dots, \hat{\theta}_M\}$ , to differentiate them from the true but unknown parameters.

Very often the natural logarithm of likelihood function is used instead. This has the advantage that the product of pdfs in Equation 4.3 becomes a sum after the logarithm is taken, which is easier to work with. Furthermore, the logarithm turns any exponent into a simple factor and, since the natural logarithm is a monotonically increasing function, the parameter values that maximize the likelihood function will also maximize its logarithm. Thus, the *log-likelihood function* (LLF) is defined as:

$$\ln L(\vec{\Theta}) = \sum_{i=1}^N \ln f(x_i|\vec{\Theta}) \quad (4.5)$$

For this analysis, a variant of the ML method for binned data is used. It is particularly useful for large data samples where one would have to evaluate a large amount of sum terms from Equation 4.5. Instead, the data can be presented in a histogram with  $N$  bins, each of which contain a certain number of entries  $\{n_1, n_2, \dots, n_N\}$ . Then, the sum of Equation 4.5 runs over the number of bins.

For the fit model used in this analysis, the number entries in each bin,  $n_i$ , is expected to be distributed following a Poisson pdf with a mean value  $\nu_i$ :

$$f(n_i|\nu_i) = \text{Poisson}(n_i|\mu_{t\bar{t}H}, \vec{\lambda}, \vec{\theta}) = \frac{\nu_i(\mu_{t\bar{t}H}, \vec{\lambda}, \vec{\theta})^{n_i}}{n_i!} e^{-\nu_i(\mu_{t\bar{t}H}, \vec{\lambda}, \vec{\theta})} \quad (4.6)$$

where  $\nu_i$  has been parameterized as [126]:

$$\nu_i(\mu_{t\bar{t}H}, \vec{\lambda}, \vec{\theta}) = \mu_{t\bar{t}H} S_i(\vec{\theta}) + B_i(\vec{\lambda}, \vec{\theta}) \quad (4.7)$$

The vector  $\vec{\lambda}$  represents the set of normalization factors for  $t\bar{t}W$  and the background events that contain fake leptons, as described in Section 4.4.1. The vector  $\vec{\theta}$  corresponds to a set of additional parameters called *nuisance parameters* (NP). They are used to encode all the systematic uncertainties considered in the analysis, which can affect the experimental data and the modeling of the signal and backgrounds. The quantity  $S_i(\vec{\theta})$  represents the mean number of signal ( $t\bar{t}H$ ) events in each bin and  $B_i(\vec{\lambda}, \vec{\theta})$  is the mean

number of background events per bin, which is given by:

$$B_i(\vec{\lambda}, \vec{\theta}) = \sum_j \lambda_j b_j(\vec{\theta}) + \sum_k b_k(\vec{\theta}) \quad (j \neq k) \quad (4.8)$$

where  $b_j(\vec{\theta})$  is the subset of all the backgrounds that will be corrected by a normalization factor  $\lambda_j$  and  $b_k(\vec{\theta})$  corresponds to the rest of the backgrounds that are fixed to their SM predictions.

The NP probability distributions are typically constrained the auxiliary measurements or theoretical predictions. This previous estimations of the NP are called *priors* and they will be also distributed according to specific pdfs. The type the prior pdf will depend on the type of NP. Two cases can be distinguished here:

1. All NPs affecting the relative contribution of the signal and/or the backgrounds in different bins (i.e. *shape* of the distributions) are denoted by  $\vec{\theta}^\alpha$ . They can take either positive or negative values and their priors are expected to be described by a Gaussian pdf:

$$Gauss(\theta_j^\alpha | \alpha_j^0, \sigma_{\alpha_j^0}) = \frac{1}{\sqrt{2\pi}\sigma_{\alpha_j^0}} \exp \left[ -\frac{(\theta_j^\alpha - \alpha_j^0)^2}{2\sigma_{\alpha_j^0}^2} \right] \quad (4.9)$$

where  $\alpha_j^0$  and  $\sigma_{\alpha_j^0}$  indicate the prior estimate of the NP and its uncertainty respectively.

2. NPs associated to the systematic uncertainty of quantities that affect the signal and/or background *normalization* (denoted by  $\vec{\theta}^\beta$ ) should not take negative values. In such cases, the prior pdf is taken to be a log-normal distribution with variance  $\kappa(\beta_k^0, \sigma_{\beta_k^0})$ :

$$LogN(\theta_k^\beta | \beta_k^0, \sigma_{\beta_k^0}) = \frac{1}{\sqrt{2\pi \ln(\kappa)}} \frac{1}{\theta_k^\beta} \exp \left[ -\frac{\ln^2(\theta_k^\beta / \beta_k^0)}{2 \ln^2(\kappa)} \right] \quad (4.10)$$

where  $\beta_k^0$  and  $\sigma_{\beta_k^0}$  are the prior estimate of the NP and its uncertainty respectively and  $\kappa = \kappa(\beta_k^0, \sigma_{\beta_k^0}) = \exp(2\beta_k^0 + \sigma_{\beta_k^0}^2) [\exp(\sigma_{\beta_k^0}^2) - 1]$ .

Furthermore, the statistical uncertainties in each bin,  $\gamma_i$ , due to the limited size of the simulated samples, are taken into account by using dedicated NPs (denoted by  $\vec{\theta}^\gamma$ ), which are assumed to be described by a Gamma pdf with the form:

$$Gamma(\theta_i^\gamma | \gamma_i) = \frac{(\theta_i^\gamma)^{\gamma_i}}{\Gamma(\gamma_i + 1)} e^{-(\theta_i^\gamma)} \quad (4.11)$$

In order to account for NP prior constraints and the bins statistical uncertainties, the LLF used in this analysis is generalized by including Equations 4.9, 4.10 and 4.11. Thus, by substituting Eq. 4.6 in Eq. 4.5 and adding the pdfs corresponding to the prior constraints and bins statistical uncertainties, the final LLF used in this analysis can be expressed as:

$$\begin{aligned}
 \ln L(\mu_{t\bar{t}H}, \vec{\lambda}, \vec{\theta}) &= \sum_{i=1}^N \ln \text{Poisson}(n_i | \mu_{t\bar{t}H}, \vec{\lambda}, \vec{\theta}) \\
 &+ \sum_{\theta_j^\alpha \in \vec{\theta}^\alpha} \ln \text{Gauss}(\theta_j^\alpha | \alpha_j^0, \sigma_{\alpha_j^0}) \\
 &+ \sum_{\theta_k^\beta \in \vec{\theta}^\beta} \ln \text{LogN}(\theta_k^\beta | \beta_k^0, \sigma_{\beta_k^0}) \\
 &+ \sum_{i=1}^N \ln \text{Gamma}(\theta_i^\gamma | \gamma_i)
 \end{aligned} \tag{4.12}$$

where:  $\vec{\theta} = \{\vec{\theta}^\alpha, \vec{\theta}^\beta, \vec{\theta}^\gamma\}$ .

The construction of the LLF is performed by the **HistFactory** software [127] of the RooFit/RooStat framework [128, 129]. The minimization is done by the MINUIT2 package [130], also from the RooFit/RooStat framework.

## 4.6.2 Definition of the test statistic and the fit significance

The ML method provides a way of estimating the unknown parameters  $\vec{\theta}$ , however, it does not directly provide a method to test the goodness of fit. In order to test a hypothesized value of  $\mu_{t\bar{t}H}$ , the *profile likelihood ratio* (PLR) is used, which is defined as:

$$\lambda(\mu_{t\bar{t}H}) = \frac{L(\mu_{t\bar{t}H}, \hat{\vec{\theta}}(\mu_{t\bar{t}H}))}{L(\hat{\mu}_{t\bar{t}H}, \hat{\vec{\theta}})} \tag{4.13}$$

Here  $\hat{\vec{\theta}}(\mu_{t\bar{t}H})$  denotes the value of  $\vec{\theta}$  that maximizes the LLF for the specified  $\mu_{t\bar{t}H}$ , i.e., it is the conditional<sup>3</sup> MLE of  $\vec{\theta}$ . The denominator correspond to the maximized likelihood function, i.e.,  $\hat{\mu}_{t\bar{t}H}$  and  $\hat{\vec{\theta}}$  are their MLE. The presence of the NP broadens the profile likelihood as a function of  $\mu_{t\bar{t}H}$  relative to what one would have if their values were fixed. This reflects the loss of information about  $\mu_{t\bar{t}H}$  due to the systematic uncertainties [126].

In this analysis, it is assumed  $\mu_{t\bar{t}H} \geq 0$ . This implies that any *physical* estimator for  $\mu_{t\bar{t}H}$  must also be non-negative, i.e., signal yields are expected to be either zero or

---

<sup>3</sup>The *conditional* MLE are related to the concept of conditional probability. They stem from a likelihood function constructed from conditional probability density functions.



positive. However, it should be noted that the ML method can produce a negative  $\hat{\mu}_{t\bar{t}H}$ . That would reflect the case when a downward fluctuation in data results in less observed events than even the background alone would predict. This is allowed, as long as the expectation value for the number of events in each bin,  $\nu_i(\mu_{t\bar{t}H}, \vec{\lambda}, \vec{\theta})$ , is non-negative. Therefore, for a model where  $\mu_{t\bar{t}H} \geq 0$ , if one finds data such that  $\hat{\mu}_{t\bar{t}H} < 0$ , then the best level of agreement between the data and any physical value of  $\mu_{t\bar{t}H}$  occurs for  $\mu_{t\bar{t}H} = 0$ . To reflect this particular case, Equation 4.13 can be transformed into:

$$\tilde{\lambda}(\mu_{t\bar{t}H}) = \begin{cases} \frac{L(\mu_{t\bar{t}H}, \hat{\vec{\theta}}(\mu_{t\bar{t}H}))}{L(\hat{\mu}_{t\bar{t}H}, \hat{\vec{\theta}})} & \hat{\mu}_{t\bar{t}H} \geq 0 \\ \frac{L(\mu_{t\bar{t}H}, \hat{\vec{\theta}}(\mu_{t\bar{t}H}))}{L(0, \hat{\vec{\theta}}(0))} & \hat{\mu}_{t\bar{t}H} < 0 \end{cases} \quad (4.14)$$

Here  $\hat{\vec{\theta}}(0)$  and  $\hat{\vec{\theta}}(\mu_{t\bar{t}H})$  refer to the conditional MLE of  $\vec{\theta}$  given a strength parameter of 0 or  $\mu_{t\bar{t}H}$ , respectively. The PLR  $\tilde{\lambda}(\mu_{t\bar{t}H})$  takes values between 0 and 1, where  $\tilde{\lambda}(\mu_{t\bar{t}H}) \sim 1$  implies a good agreement of the data with the value of  $\mu_{t\bar{t}H}$  being tested.

Furthermore, it has been shown by Wilks [131] and Wald [132] that, in the asymptotic limit of a large data sample, the pdf of  $-2 \ln [\tilde{\lambda}(\mu_{t\bar{t}H})]$  approaches a chi-square distribution. Therefore, without loss of generality, it is often more convenient to use an equivalent definition for the test statistic in the form:

$$\tilde{t}_{\mu_{t\bar{t}H}} = -2 \ln [\tilde{\lambda}(\mu_{t\bar{t}H})] = \begin{cases} -2 \ln \frac{L(\mu_{t\bar{t}H}, \hat{\vec{\theta}}(\mu_{t\bar{t}H}))}{L(\hat{\mu}_{t\bar{t}H}, \hat{\vec{\theta}})} & \hat{\mu}_{t\bar{t}H} \geq 0 \\ -2 \ln \frac{L(\mu_{t\bar{t}H}, \hat{\vec{\theta}}(\mu_{t\bar{t}H}))}{L(0, \hat{\vec{\theta}}(0))} & \hat{\mu}_{t\bar{t}H} < 0 \end{cases} \quad (4.15)$$

In this case, the values of  $\tilde{t}_{\mu_{t\bar{t}H}}$  are found between 0 and  $+\infty$ , corresponding to the  $\tilde{\lambda}(\mu_{t\bar{t}H})$  values of 1 and 0 respectively. Thus, higher values of  $\tilde{t}_{\mu_{t\bar{t}H}}$  indicate increasing incompatibility of the data with  $\mu_{t\bar{t}H}$ .

To quantify the level of disagreement between the hypothesized  $\mu_{t\bar{t}H}$  and the observed in data, the  $p$ -value is computed as:

$$\tilde{p}_{\mu_{t\bar{t}H}} = \int_{\tilde{t}_{\mu_{t\bar{t}H}, obs}}^{+\infty} f(\tilde{t}_{\mu_{t\bar{t}H}} | \mu_{t\bar{t}H}) d\tilde{t}_{\mu_{t\bar{t}H}} \quad (4.16)$$

where  $\tilde{t}_{\mu_{t\bar{t}H}, obs}$  is the value of the statistic  $\tilde{t}_{\mu_{t\bar{t}H}}$  observed from the data and  $f(\tilde{t}_{\mu_{t\bar{t}H}} | \mu_{t\bar{t}H})$  denotes the pdf of  $\tilde{t}_{\mu_{t\bar{t}H}}$  under the assumption of the signal strength  $\mu_{t\bar{t}H}$ .

In particle physics, however, it is often customary to use an equivalent quantity called *significance* ( $Z$ ). The significance is defined such that a Gaussian distributed variable found  $Z$  standard deviations above its mean has an upper-tail probability equal to the

$p$ -value:

$$Z = \Phi^{-1}(1 - \tilde{p}_{\mu_{t\bar{t}H}}) \quad (4.17)$$

Here  $\Phi^{-1}$  is the quantile (inverse of the cumulative distribution) of the Gaussian distribution.

In this analysis, a special case of Equation 4.15 is used to test the *background-only* hypothesis ( $\mu_{t\bar{t}H}=0$ ). For this, the special notation  $q_0 = \tilde{t}_0$  is used:

$$q_0 = \tilde{t}_0 = \begin{cases} -2 \ln [\lambda(0)] & \hat{\mu}_{t\bar{t}H} \geq 0 \\ 0 & \hat{\mu}_{t\bar{t}H} < 0 \end{cases} \quad (4.18)$$

where  $\lambda(0)$  is the PLR for  $\mu_{t\bar{t}H}=0$  as defined in Equation 4.13.

If the data fluctuates in such way fewer events than predicted by background processes alone are observed, then  $\hat{\mu}_{t\bar{t}H} < 0$ , which leads to  $q_0 = 0$ . As the number of signal events increases above the expected background (i.e.,  $\hat{\mu}_{t\bar{t}H}$  increases), the values of  $q_0$  also increase, corresponding to higher level of incompatibility between the data and the  $\mu_{t\bar{t}H}=0$  hypothesis.

Analogously to the  $\tilde{t}_{\mu_{t\bar{t}H}}$  case, the level of disagreement corresponding to the observed  $q_0$  is computed by evaluating the corresponding  $p$ -value ( $p_0$ ):

$$p_0 = \int_{q_{0,obs}}^{+\infty} f(q_0|0) dq_0 \quad (4.19)$$

And the significance is obtained as:

$$Z_0 = \Phi^{-1}(1 - p_0) \quad (4.20)$$

Traditionally, the particle physics community has tended to regard rejection of the *background-only* hypothesis with a significance of at least  $Z_0 = 5$  as an appropriate level to constitute an *observation*. This corresponds to a  $p$ -value of  $2.87 \times 10^{-7}$ . If  $Z_0 \geq 3$  then *evidence* of the presence of the signal process is claimed.

It is also interesting to estimate the the significance one can *expect* if the data would correspond to a  $\mu_{t\bar{t}H}=1$ . For this purpose, a so called *Asimov* dataset is defined in such way that all the parameter MLE are equal to the true parameter values and all statistical fluctuations are suppressed. Thus, the Asimov dataset is constructed using all the MC processes (including the signal) and the *expected significance* is estimated by assuming a  $\mu_{t\bar{t}H}=1$ .

### 4.6.3 Treatment of systematic uncertainties

In this analysis, the systematic uncertainties can be classified in two major groups: “experimental” and “theoretical” (modeling) systematics. They are, as discussed in Section 4.6.1, included in the analysis in the form of NPs of the ML method with prior constraints given by Equations 4.9 and 4.10 for *shape* and *normalization* systematics respectively.

The experimental systematics are related to the luminosity, trigger efficiency, lepton reconstruction, identification and isolation efficiencies, jet calibration, *b*-tagging efficiency and pileup events. They are evaluated in dedicated studies by the ATLAS performance groups and are used in this analysis either as an overall per-event re-weighting or as a re-scaling of the energy or momentum of the reconstructed objects. The theoretical systematics, on the other hand, stem from uncertainties in the cross-section and the modeling of the signal and background processes. Cross-section uncertainties affect the event normalization and are taken from the latest available theoretical calculations. The other modeling uncertainties are estimated by comparing different MC samples and can affect both the normalization and/or shape.

The effect of the systematics on the resulting yields is evaluated by assuming a  $\pm 1\sigma$  variation around their nominal value. In the following, a description of the systematics used in this analysis is presented. In Section 4.7, the fit results as well as the impact of the systematics on the  $\mu_{t\bar{t}H}$  estimation, will be thoroughly discussed.

#### Experimental systematic uncertainties.

- **Luminosity:** The integrated luminosity uncertainty for the data taken in the 2015-2017 period, corresponding to  $80 \text{ fb}^{-1}$ , is 2.0%. This uncertainty only affects the overall event normalization and it is encoded in a single nuisance parameter.
- **Pileup re-weighting:** This uncertainty is below 1% and is associated to the per-event pileup re-weighting of the MC simulations in order to correct for the differences in the pileup distributions with respect to the data. It can affect both the event normalization and the shape of the kinematic properties. This systematic is encoded in one nuisance parameter.
- **Physics objects (leptons, jets &  $E_T^{miss}$ ):** These uncertainties are related to the efficiencies and calibrations of the reconstructed physics objects.

Electrons and muons contribute with 18 nuisance parameters. The size of the systematic uncertainties for leptons in this analysis is in the order of 1% or less for each nuisance parameter.

Jets add another 47 nuisance parameters. The combined size of these uncertainties is below 6% for individual jets [61]. However, due to the high jet multiplicity of the

targeted final state, the size of these systematics per event is amplified.

Finally, missing transverse energy contribute with 3 more nuisance parameters. Note that, even though  $E_T^{miss}$  is not explicitly used for the event selection, it can still impact the measurement of energy scales and resolution of tracks associated with reconstructed leptons and jets. Therefore, its related uncertainties are also considered, with an overall size bellow 1%.

- **Charge flip:** The charge flip systematic uncertainty is estimated from the uncertainties in the determination of the charge flip rates defined in Section 4.4.1. Since these rates depend on the lepton  $p_T$  and  $|\eta|$ , this systematic affects both the normalization and shape of kinematic properties in this type of events. The charge flip systematic uncertainty is encoded in a single nuisance parameter and its size is bellow 1%.

## Theoretical systematic uncertainties.

- **Signal modeling:** The  $t\bar{t}H$  signal modeling systematics are encoded in 41 nuisance parameters that account for:

Cross-section normalization uncertainties related to the choice of QCD scale ( $+5.8\%$  to  $-9.2\%$ ) and PDF+ $\alpha_S$  ( $\pm 3.6\%$ ) [20]. Since the choice of a given PDF set determines the value of  $\alpha_S$  used in the ME calculations, their effect on the cross-section normalization is taken as the sum in quadrature of both uncertainties.

Uncertainties in the modeling of the acceptance and event kinematics (shape). To account for this, the renormalization and factorization scales are varied up and down simultaneously by a factor of 0.5 and 2.0 with respect to their central values. This is done in a way that keeps the cross-section normalization constant, to avoid double counting with respect to the uncertainty from the previous paragraph.

Uncertainties on the Higgs decay branching ratios relevant for this analysis:  $H \rightarrow WW^*$  ( $+1.6\%$  to  $-1.5\%$ ),  $H \rightarrow ZZ^*$  ( $+1.6\%$  to  $-1.5\%$ ),  $H \rightarrow \tau^-\tau^+$  ( $\pm 1.7\%$ ) and *Others* ( $\pm 5\%$ ) [20]. These also apply to the processes where a single top quark is produced in association with a Higgs boson (see Section 4.4.2).

Uncertainty related to the choice of parton shower and hadronization models. It is estimated by comparing the nominal prediction, POWHEG+PYTHIA8 (see Section 4.1.3), with that obtained using an alternative sample generated with POWHEG+HERWIG7 [133].

Uncertainty from the choice of the shower tune used for the nominal  $t\bar{t}H$  sample (A14 tune), which can alter the acceptance through modifications of the jet multi-

plicity and kinematics. It is estimated by considering the Var3c A14 tune variation according to the procedure described in Ref. [82].

PDF uncertainty using the PDF4LHC error set as recommended in [134]. These affect only the acceptance and event kinematics (shape).

- **$t\bar{t}W$  modeling:** The  $t\bar{t}W$  systematic uncertainties are included in 34 nuisance parameters that account for:

Uncertainty due to the generator choice for matrix-element calculations by comparing the prediction from SHERPA2.2.1 (nominal) to the one from MG5\_AMC@NLO.

Uncertainty due to the variation of the renormalization and factorization scales and PDF uncertainty. These PDF nuisance parameters are correlated with the ones used in  $t\bar{t}H$ .

- **$t\bar{t}(Z/\gamma^*)$  modeling:** Seven nuisance parameters are included in order to account for:

Cross-section normalization uncertainties related to the choice of QCD scale ( $+9.6\%$  and  $-11.3\%$ ) and PDF+ $\alpha_S$  ( $\pm 4\%$ ).

Uncertainty due to the choice of renormalization and factorization scales.

Uncertainty on the generator choice (by comparing the predictions of MG5\_AMC@NLO +PYTHIA8 versus SHERPA2.2.0) and the shower tune.

- **Fakes modeling:** A total of 18 nuisance parameters encode the uncertainties associated with the estimation of the background events containing HDFake( $e/\mu$ ), ICFake or MCFake leptons using the semi data-driven technique described in Section 4.4.1.

The fake modeling uncertainties were calculated as the shape difference, in several differential distribution, between a given fake background contribution and its estimation from data:

$$\frac{data - (allMC - fake_i)}{fake_i} \quad i = HDFake(e/\mu), ICFake, MCFake \quad (4.21)$$

The chosen distributions are those that offer the best separation power between a given fake background type and the rest of the MC predictions. For example, the uncertainty estimation for HDFakes is done using the  $HT_{lep}$  distribution, which is the shape used in the fit regions that are enriched on HDFake leptons (see Section 4.5.1).

The shape difference is derived for all control and signal regions. In particular, for the  $2\ell SS$  and  $3\ell$  channel regions, the strict lepton definitions are relaxed by

removing PLV or conversion-related requirements in order to enhance the acceptance of HDFake or ICFake/MCFake leptons respectively. This is done in order to reduce possible the bias from statistical fluctuations in those regions.

Using this method, uncertainties on the HDFake( $e/\mu$ ), ICFake or MCFake estimation were found in the range of  $\pm 5\%$  up to  $\pm 20\%$  across all fitting regions.

- **Other background modeling:** For the rest of the (less contributing) MC simulated samples, a 50% normalization uncertainty on the cross-section is assigned conservatively. This accounts for 18 nuisance parameters. However, for the  $t\bar{t}$  samples used to estimate the fake leptons component, an additional nuisance parameter is used to account for the uncertainty in the generator modeling of the initial and final state QCD/QED radiation.

Moreover, given the large discrepancy observed in the  $2\ell SS$  channel regions with at least two  $b$ -jets and positively charged leptons ( $2b(++)$ ), an additional nuisance parameter is added to the fit in order to account for it. The motivation for this can be summarized in two main points:

1. After performing extensive tests in order to determine the origin of the  $2b(++)$  discrepancy, it has not been possible to definitely identify it.
2. The p-value for the plot in Figure 4.7 (before adding this systematic uncertainty) was found to be below 0.001. This indicates an incompatibility of the background and signal predictions with data that cannot be attributed to statistical fluctuations. Such incompatibility could lead to unphysical results in the determination of background normalization factors. This is particularly important for  $t\bar{t}W$  due to its large relative fraction in those regions.

This systematic uncertainty was added to the  $5j2b(++)$  and  $4j2b(++)$  regions according to the size of the data/MC discrepancy in each of them, i.e.  $\pm 42\%$  and  $\pm 58\%$  respectively, assuming full correlation.

- **Simulation samples size (gammas):** A total of 24 nuisance parameters (one for each bin in the fit model) encodes the statistical uncertainties in each bin,  $\gamma_i$ , due to the limited size of the simulated samples, as described in Section 4.6.1.

A summary of the systematic uncertainties used in this thesis is shown in Table 4.7. The number of NP associated to each systematic type is indicated together with the type of systematic: “N” means that the uncertainty is taken as normalization-only for all processes and regions affected, whereas “S” denotes systematics that are considered shape-only.

**Table 4.7:** Sources of systematic uncertainty considered in the analysis. “SN” means that the uncertainty is taken as both shape and normalization.

Systematic uncertainty	Number of NP	Type
<b>Experimental</b>		
Luminosity	1	N
Pileup re-weighting	1	SN
<i>Physics objects</i>		
Electrons (efficiencies+resolution)	6	SN
Muons (efficiencies+resolution)	12	SN
Jet energy scale and resolution	29	SN
Jet vertex tagging	1	SN
Jet flavor tagging	17	SN
$E_T^{miss}$	3	SN
Electron charge flip	1	SN
Total (Experimental)	71	
<b>Theoretical</b>		
<i>Signal (<math>t\bar{t}H</math>) modeling</i>		
Cross-section (QCD, PDF+ $\alpha_s$ )	2	N
Factorization and re-normalization scales	1	S
Higgs branching ratios	4	N
Parton shower and hadronization modeling	1	SN
Parton shower tune (A14)	1	SN
PDF	32	S
<i><math>t\bar{t}W</math> modeling</i>		
Generator	1	SN
Factorization and re-normalization scales	1	S
PDF	32	S
<i><math>t\bar{t}(Z/\gamma^*)</math> modeling</i>		
Cross-section (QCD, PDF+ $\alpha_s$ )	2	N
Factorization and re-normalization scales	3	S
Generator	1	SN
Parton shower tune (A14)	1	SN
<i>Fakes modeling</i>		
MCFakes	1	S
ICFakes	1	S
HDFakes ( $e$ )	4	S
HDFakes ( $\mu$ )	5	S
<i>Other background modeling</i>		
Cross-section	19	N
$t\bar{t}$ extra radiation modeling	1	S
$2b(++)$ modeling in $2\ell SS$	1	S
Simulation samples size (gammas)	24	N
Total (Theoretical)	138	
Total (Overall)	209	

## 4.7 Fit results

The likelihood fit performed in this analysis is done using the combination of all the event categories defined in Section 4.5. This means that the regions represented in Figures 4.5, 4.7 and 4.11 are all fitted simultaneously. In total, 24 regions are used for the fit, which are represented in the summary plot of Figure 4.12. The plot shows the post-fit signal and background comparison with data, while the pre-fit comparison is represented by the dashed blue line in the ratio pad. The measured data is found to be compatible with the MC predictions within statistical and systematic uncertainties.

The size of the  $t\bar{t}H$  signal,  $t\bar{t}W$ , HDFake( $e/\mu$ ), ICFake and MCFake displayed in the summary plot are already scaled by their respective normalization factors, which are presented in Table 4.8. The MLE for the signal strength and the normalization factors for HDFakes( $e/\mu$ ) and ICFakes are found to be compatible with 1 within their respective total uncertainties. The  $t\bar{t}W$  and MCFakes normalization factors, however, are found to be approximately  $1\sigma$  above their MC predictions. These results were found to be consistent with the latest published multivariate-based multilepton analysis in Ref. [115]. Moreover, the observed  $t\bar{t}W$  normalization factor is compatible with the most recent dedicated  $t\bar{t}W$  measurement in ATLAS [123], where a normalization factor  $\hat{\lambda}_{t\bar{t}W} = 1.41 \pm 0.33$  was obtained.

**Table 4.8:** MLE for the signal strength ( $\hat{\mu}_{t\bar{t}H}$ ) and the normalization factors for  $t\bar{t}W$  ( $\hat{\lambda}_{t\bar{t}W}$ ) and the Fakes ( $\hat{\lambda}_{ICFakes}$ ,  $\hat{\lambda}_{MCFakes}$ ,  $\hat{\lambda}_{HDFakes(e)}$  and  $\hat{\lambda}_{HDFakes(\mu)}$ ).

$\hat{\mu}_{t\bar{t}H}$	$\hat{\lambda}_{t\bar{t}W}$	$\hat{\lambda}_{ICFakes}$	$\hat{\lambda}_{MCFakes}$	$\hat{\lambda}_{HDFakes(e)}$	$\hat{\lambda}_{HDFakes(\mu)}$
$0.88^{+0.54}_{-0.51}$	$1.25^{+0.23}_{-0.22}$	$0.79^{+0.28}_{-0.28}$	$1.50^{+0.46}_{-0.46}$	$1.02^{+0.31}_{-0.31}$	$1.10^{+0.18}_{-0.18}$

$$\hat{\mu}_{t\bar{t}H} = 0.88^{+0.54}_{-0.51} = 0.88^{+0.37}_{-0.36}(stat)^{+0.39}_{-0.36}(syst) \quad (4.22)$$

The total statistical-plus-systematic  $\pm 1\sigma$  variation of  $\hat{\mu}_{t\bar{t}H}$  ( $\Delta\hat{\mu}_{t\bar{t}H}$ ) is obtained by minimizing the LLF with respect to all the parameters but  $\mu_{t\bar{t}H}$ , as described in Ref. [126]. A similar approach is used also for the other normalization factors. Then, an estimate of the total systematic uncertainty for the signal strength is computed by subtracting in quadrature from  $\Delta\hat{\mu}_{t\bar{t}H}$  the total statistical uncertainty, which is determined by re-doing the fit fixing all NPs to their MLE values. Note that, since the background normalization factors are not NPs, the total statistical uncertainty quoted in Eq. 4.22 includes the uncertainty on the background normalization factors. In order to obtain the “true” statistical uncertainty on  $\mu_{t\bar{t}H}$ , called *intrinsic statistical uncertainty*, the fit is repeated while fixing all the NPs *together* with the background normalization factors.

The observed significance for the *signal+background* hypothesis, as described in Sec-



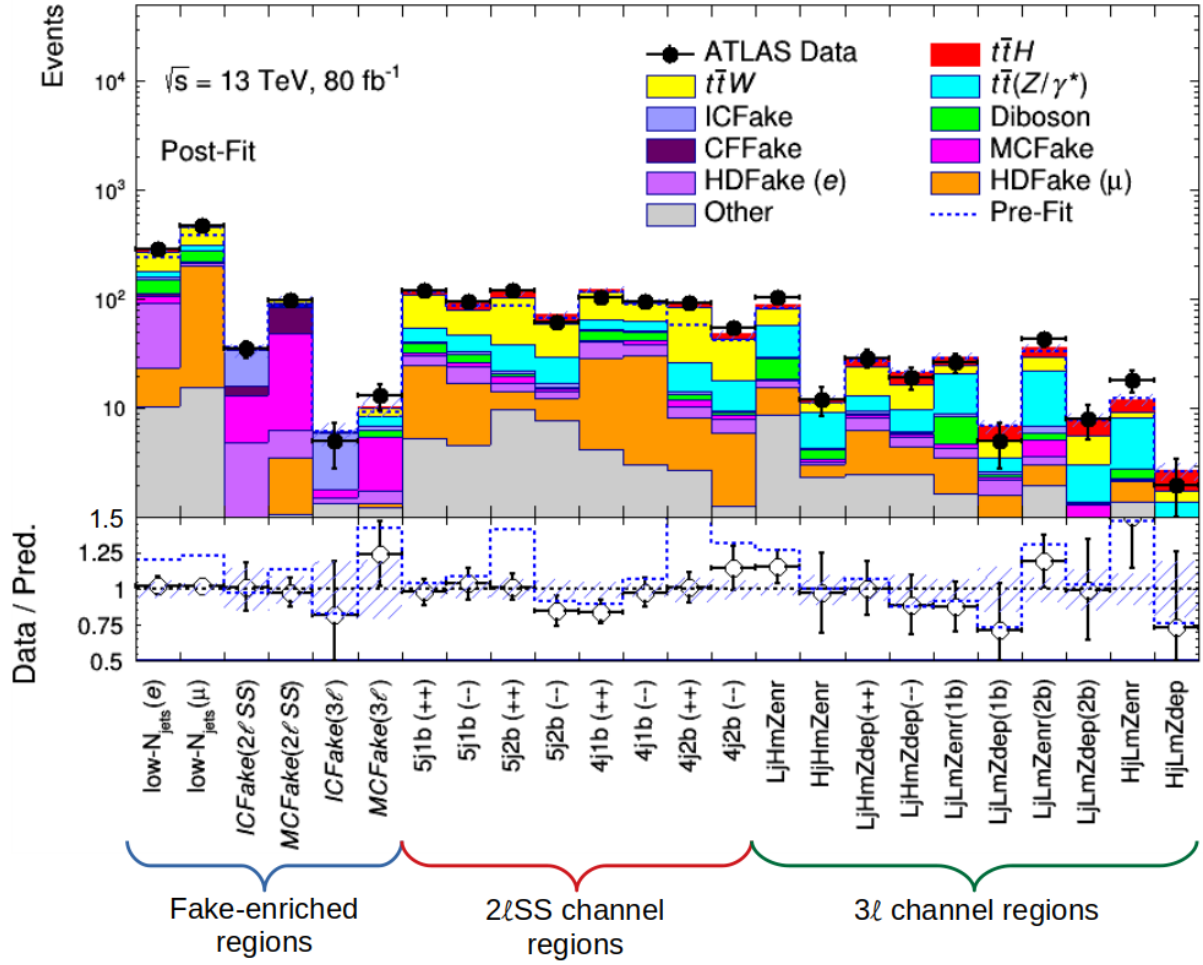


**Figure 4.12:** Post-fit summary plot of all the regions used in the fit. Note that the  $2\ell SS$   $low-N_{jets}$  regions are represented here as a single bin. However, they consist on several bins of the  $HT_{lep}$  distribution (see Figure 4.6). The dashed blue line in the ratio plot corresponds to the pre-fit MC predictions. The uncertainty band in the ratio plot includes the total systematic uncertainties.

tion 4.6.2, was estimated to be  $Z_0^{obs} = 1.80\sigma$ , while the expected significance was found to be  $Z_0^{exp} = 2.52\sigma$ . This expected significance was estimated using an Asimov fit assuming a  $\mu_{t\bar{t}H} = 1$  and fixing all the NPs and background normalization factors to their MLE.

From Eq. 4.22 it can be seen that both the statistical and systematic uncertainties have similar impact on the analysis precision. In order to find out which systematic uncertainties that impact the most the  $t\bar{t}H$  signal strength, a procedure similar to the one used to extract the total systematic uncertainty is used. Instead of determining the individual impact of each parameter, some NPs and the normalization factors are grouped in categories trying to follow a similar scheme as the one presented in Table 4.7. For each parameter group, their combined systematic uncertainty is evaluated by repeating the fit (after fixing all the parameters in the group to their MLE values) and subtracting in quadrature the obtained uncertainty from the total uncertainty of the original fit.

Table 4.9 contains a summary of the impact of all the grouped sources of uncertainty

considered in this analysis. The biggest impact corresponds to the  $t\bar{t}W$  normalization ( $^{+0.28}_{-0.23}$ ), followed by the JES/JER uncertainty ( $^{+0.23}_{-0.19}$ ) and the  $t\bar{t}(Z/\gamma^*)$  cross-section modeling ( $^{+0.14}_{-0.13}$ ).

It is also interesting to see which individual parameters in the fit affect the most the uncertainty of the signal strength. This is shown in the “ranking” plot in Figure 4.13, where the 20 fit parameters with highest impact on  $\Delta\hat{\mu}_{t\bar{t}H}$  are ordered from biggest (top) to smallest (bottom) impact.

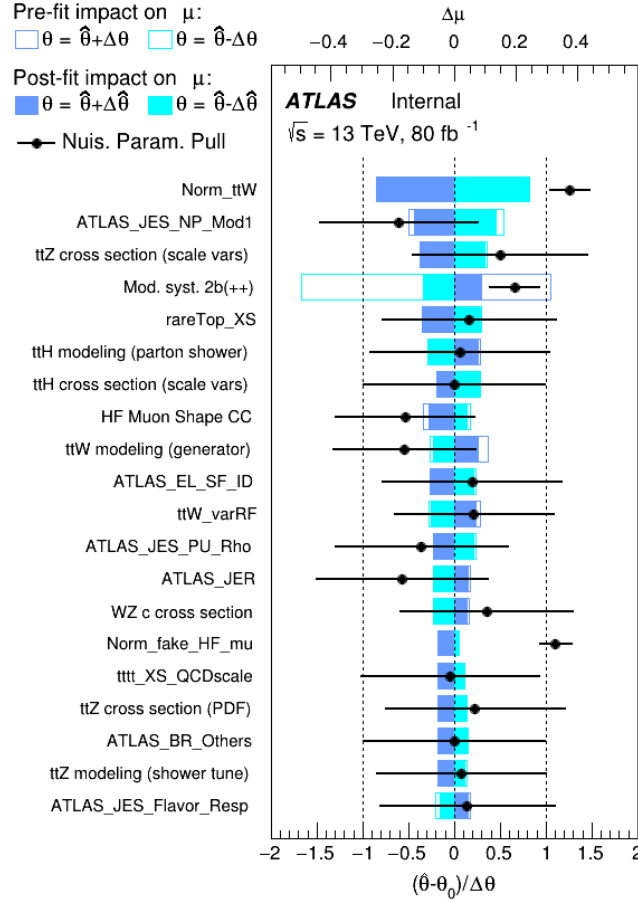


**Figure 4.13:** Summary of the 20 most important parameters ranked according to their impact on the uncertainty of the signal strength ( $\Delta\hat{\mu}_{t\bar{t}H}$ ). Systematic uncertainties are ranked from top to bottom on the left axis according to the post-fit impact shown in solid blue/cyan. The pre-fit impact on  $\mu_{t\bar{t}H}$  is indicated by the empty blue/cyan boxes. The upper axis represents the scale of  $\Delta\hat{\mu}_{t\bar{t}H}$ . The plot also includes the values of the NP pull (shown as black dots) and of its uncertainty (black lines). The nominal ( $\pm 1\sigma$ ) pre-fit bound on each nuisance parameter is represented by the area between the vertical dashed lines. The scale of the pull magnitude is shown in the lower axis.

This figure also shows the “pulls” of each of those parameters and their uncertainty. The fitted nuisance parameters are expected to be distributed according to a Gaussian model (or log-normal). Given the value of the prior for that nuisance parameter ( $\theta_0$ ), its

uncertainty ( $\sigma_{\theta_0}$ ) and their MLE estimators ( $\hat{\theta}_0, \hat{\sigma}_{\theta_0}$ ), the *pull* is defined as:

$$\Delta\theta = \frac{\hat{\theta} - \theta_0}{\sigma_{\theta_0}} \quad (4.23)$$

and it is also expected to be Gaussian-distributed with zero mean and a standard deviation of  $\sigma_{\Delta\theta} = 1$ . Since  $\theta_0 = 0$  for all NPs, any deviation from this value indicates that the fit is trying to correct (or *pulling*) for a biased initial prediction of the parameter corresponding to that particular NP. Furthermore, the fit can constrain the estimated uncertainty associated to the NP itself if it has more statistical sensitivity to that NP than the auxiliary measurement used to determine its prior constrain. Thus, a post-fit uncertainty smaller than  $1\sigma_{\theta_0}$  is observed in some cases (e.g. *Mod. syst.  $2b(++)$* ). Note that Eq. 4.23 only applies to nuisance parameters. Therefore, in order to represent normalization factors (e.g. *Norm. $ttW$* ) in the ranking plot, they have been accommodated with respect to the (bottom)  $x$ -axis using their MLE values.

Form the ranking plot, it can be seen that the parameter with larger impact in  $\Delta\hat{\mu}_{t\bar{t}H}$  is the  $t\bar{t}W$  normalization factor. This parameter appear high in this ranking due to large correlations between them and the signal strength. This is checked by looking at the correlation coefficients:

$$\rho_{ij} = \frac{\text{Cov}(\theta_i, \theta_j)}{\sigma_{\theta_i}\sigma_{\theta_j}} \quad (4.24)$$

where  $\text{Cov}(\theta_i, \theta_j)$  are the coefficients of the covariance matrix of the parameters  $\theta_i$  and  $\theta_j$ .

These coefficients are represented graphically in the correlation matrix of Figure 4.14. If the fit model contains no significant bias, it is expected that the fit result for one NP does not impact the result for another NPs, specially, the signal strength. However, these large correlations between  $\hat{\mu}_{t\bar{t}H}$  and the  $t\bar{t}W$  normalization factor arise from the large contamination of  $t\bar{t}W$  events in the signal regions of the fit. Despite all efforts to try to create regions with the highest purity of  $t\bar{t}H$  and  $t\bar{t}W$ , it is not possible to separate them well enough so that the fit can effectively decorrelate them. The large correlation between the  $2b(++)$  systematic NP and the  $t\bar{t}W$  normalization factor was also expected, since the  $2b(++)$  regions in  $2\ell SS$  are dominated by  $t\bar{t}W$ .

For the estimation of the  $t\bar{t}H$  cross-section, the MLE of the signal strength and the SM cross-section prediction can be used, which leads to:

$$\hat{\sigma}_{t\bar{t}H} = \hat{\mu}_{t\bar{t}H} \times \sigma_{t\bar{t}H}^{SM} = 446_{-227}^{+241} fb \quad (4.25)$$

This result is in agreement with the SM prediction of  $507_{-50}^{+35} fb$ , which is computed at NLO in QCD with the leading order (LO) electroweak corrections [83–88]..

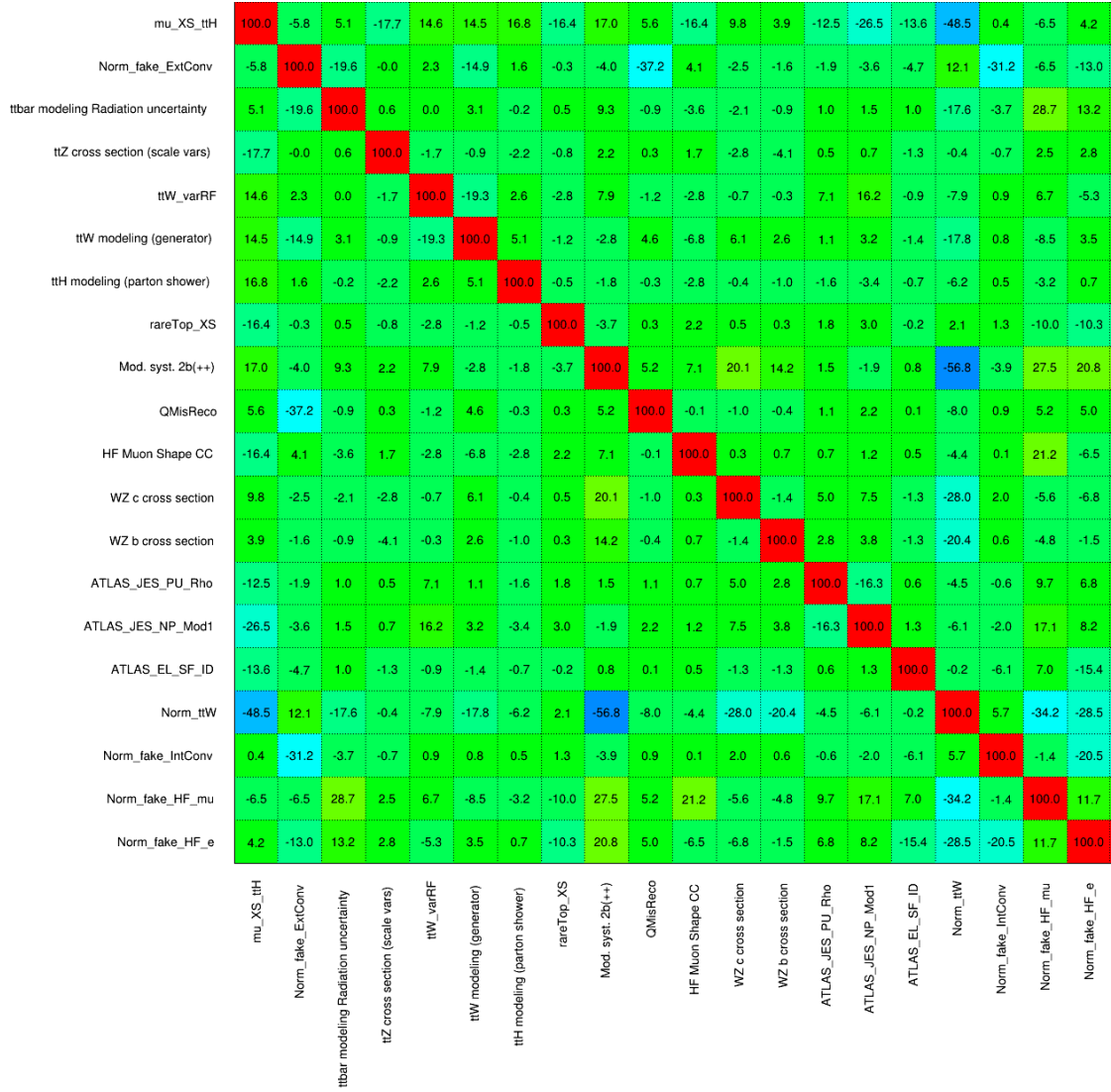


**Figure 4.14:** Post-fit correlation matrix for the nuisance parameters and the signal strength. Only the parameter pairs with correlations above 15% are plotted here.

**Table 4.9:** Breakdown of the contributions to the total uncertainty of  $\hat{\mu}_{t\bar{t}H}$ . Values below 0.01 are rounded to 0.00. Due to rounding effects and correlations between the different sources of uncertainty, the total systematic uncertainty is different from the sum in quadrature of the individual sources.

Uncertainty source	$\Delta\hat{\mu}$	
Luminosity	+0.06	-0.04
Pileup re-weighting	+0.03	-0.03
Electrons (efficiencies + resolution)	+0.08	-0.06
Muons (efficiencies + resolution)	+0.03	-0.03
Jet energy scale and resolution	+0.23	-0.19
Jet vertex tagging	+0.02	-0.02
Jet flavor tagging	+0.06	-0.05
Missing transverse energy	+0.00	-0.00
Electron charge flip	+0.03	-0.03
$t\bar{t}H$ modeling (cross-section)	+0.13	-0.03
$t\bar{t}H$ modeling (fact. & had. scales)	+0.02	-0.01
Higgs branching ratios	+0.08	-0.02
$t\bar{t}H$ modeling (parton shower)	+0.12	-0.05
$t\bar{t}H$ modeling (shower tune)	+0.00	-0.00
$t\bar{t}H$ modeling (PDF)	+0.04	-0.01
$t\bar{t}W$ modeling (generator)	+0.08	-0.07
$t\bar{t}W$ modeling (fact. & had. scales)	+0.07	-0.08
$t\bar{t}W$ modeling (PDF)	+0.02	-0.03
$t\bar{t}(Z/\gamma^*)$ modeling (cross-section)	+0.14	-0.13
$t\bar{t}(Z/\gamma^*)$ modeling (fact. & had. scales)	+0.02	-0.02
$t\bar{t}(Z/\gamma^*)$ modeling (generator)	+0.01	-0.00
$t\bar{t}(Z/\gamma^*)$ modeling (shower tune)	+0.05	-0.04
Fakes modeling (MCFake)	+0.02	-0.02
Fakes modeling (ICFake)	+0.02	-0.01
Fakes modeling (HDFake e)	+0.00	-0.00
Fakes modeling (HDFake $\mu$ )	+0.08	-0.09
Other background modeling (cross-section)	+0.08	-0.07
Other background modeling ( $2b + +$ syst.)	+0.08	-0.09
$t\bar{t}$ extra radiation modeling	+0.03	-0.03
Simulation sample size (gammas)	+0.07	-0.08
Total systematic uncertainty	+0.39	-0.36
Intrinsic statistical uncertainty	+0.23	-0.27
Normalization factor (HDFake leptons)	+0.05	-0.04
Normalization factor (ICFake/MCFake electrons)	+0.03	-0.04
Normalization factor ( $t\bar{t}W$ )	+0.28	-0.23
Total statistical uncertainty	+0.37	-0.36
Total uncertainty	+0.54	-0.51

---

---

# Conclusions and Outlook

The discovery of the Higgs boson and the measurement of some of its properties with great precision constituted a major success for the Standard Model of particle physics in the past decade. However, some important properties such as its coupling to fermions are still not measured precisely. Since the top-quark is the heaviest fermion, its coupling to the Higgs boson is expected to be the largest. Therefore, the production of a Standard Model Higgs boson in association with a pair of top-quarks,  $t\bar{t}H$ , is of particular interest, specially since it allows a direct measurement of this coupling at the LHC.

This thesis presented a search for the associated production of Higgs bosons and a top-quark pairs in multilepton final states based on  $80 \text{ fb}^{-1}$  of data collected by the ATLAS detector at the LHC during 2015-2017 at  $\sqrt{s}=13 \text{ TeV}$ . The search is sensitive to the  $H \rightarrow WW^*$ ,  $H \rightarrow ZZ^*$  and  $H \rightarrow \tau^-\tau^+$  decay modes and was performed in the two most sensitive multilepton channels:  $2\ell SS$  and  $3\ell$ .

An important source of background for both channels in this analysis corresponded to events containing fake leptons coming from hadron decays and photon conversions. In order to estimate the size of their contribution, a novel semi-data-driven method was implemented. It consisted in creating different categories for each fake event type using simulated samples. The size of the contribution of each fake category was then adjusted by applying normalization factors extracted in a likelihood fit to data. From the same fit, the  $t\bar{t}H$  signal strength,  $\mu_{t\bar{t}H} = \sigma_{t\bar{t}H}/\sigma_{t\bar{t}H}^{SM}$ , and normalization for the  $t\bar{t}W$  background were simultaneously extracted.

The  $t\bar{t}H$  signal strength was found to be  $\hat{\mu}_{t\bar{t}H} = 0.88_{-0.36}^{+0.37}(\text{stat})_{-0.36}^{+0.39}(\text{syst})$ , which corresponds to  $\hat{\sigma}_{t\bar{t}H} = 446_{-227}^{+241} \text{ fb}$ , in agreement with the SM prediction of  $507_{-50}^{+35} \text{ fb}$ . Similar results have been obtained by the multivariate-based  $t\bar{t}HML$  analysis recently published in [115]. The statistical significance of the observed signal corresponds to a  $1.80\sigma$  excess of over the background-only hypothesis. This value is below the one reported in the  $t\bar{t}HML$  combination with 2015-2016 data [25] for the  $2\ell SS$  and  $3\ell$ , where both channels show more than  $2\sigma$  excess. This difference is primarily caused by the fact that the  $t\bar{t}W$  normalization is extracted from the likelihood fit (instead of being fixed to its SM theoretical prediction). The  $t\bar{t}W$  normalization uncertainty has the biggest impact on the total  $\mu_{t\bar{t}H}$  uncertainty and, thus, the statistical significance. Moreover, the  $t\bar{t}W$  normalization uncertainty was found to be heavily impacted by the data/MC discrepancy observed in

---

$2\ell SS$  regions with more than one  $b$ -jet and positively charged leptons ( $2b(++)$ ). This discrepancy was studied but the cause could not be determined conclusively. Therefore, it is important to continue investigating this effect until it is well understood. This may be done in two ways: one dedicated to better understand the backgrounds (e.g., through more precise measurements of processes such as  $t\bar{t}W$ , further study of possible missing background contributions, etc); and the other dedicated to isolate a possible detector effect (e.g., affecting  $b$ -tagging). On the second point, it would be interesting to cross-check the results with similar CMS analyses, since an observation of a  $2b(++)$  discrepancy on their part would be a strong argument against a detector effect.

The precision of the  $t\bar{t}H$  measurement presented here is limited in a similar degree by statistical systematic uncertainties. The latter are related to Jet Energy Scale and Resolution (JES/JER),  $t\bar{t}W$  normalization and  $t\bar{t}(Z/\gamma^*)$  cross-section modeling uncertainties. Therefore, the natural next step for  $t\bar{t}HML$  in the near future is to include the data collected in 2018, which will increase the total integrated luminosity up to approximately  $140 \text{ fb}^{-1}$ . This will almost double the amount of data used in this analysis and, thus, improve the statistical uncertainty. In addition, new object reconstruction algorithms and calibrations will be used to improve uncertainties like JES. In particular, a new method to reconstruct jets will be utilized, which combines both tracking and calorimeter information. This is expected to improve the reconstruction efficiency and energy resolution of jets, specially at low- $p_T$ , where the tracker system has better energy resolution and charged particles rejected by calorimeter noise thresholds can be recovered.

The  $t\bar{t}H$  searches constitute the first step towards the goal of constraining the top Yukawa coupling at the LHC in a direct and almost model-independent way. Among these searches, the  $t\bar{t}HML$  channel plays an important role due to its higher sensitivity, specially in the  $2\ell SS$  and  $3\ell$  channels. In the coming years the LHC accelerator will enter its third run period (Run 3), where it will begin to operate at its nominal center-of-mass energy of 14 TeV. During this period, the integrated luminosity will roughly double with respect to Run 2, allowing more precise measurements of many processes, particularly those involving Higgs bosons. During this period,  $2\ell SS$  and  $3\ell$  multilepton channels are expected to achieve  $5\sigma$  observation of the  $t\bar{t}H$  process.



# Bibliography

- [1] ATLAS Collaboration, “Observation of a new particle in the search for the Standard Model Higgs boson with the ATLAS detector at the LHC,” *Phys. Lett.*, vol. B716, pp. 1–29, 2012.
- [2] CMS Collaboration, “Observation of a New Boson at a Mass of 125 GeV with the CMS Experiment at the LHC,” *Phys. Lett.*, vol. B716, pp. 30–61, 2012.
- [3] J. Iliopoulos, “Progress in Gauge Theories,” in *High energy physics. Proceedings, 17th International Conference, ICHEP 1974, London, England, July 01-July 10, 1974*, pp. III.89–116, 1974.
- [4] C. Englert, A. Freitas, M. M. Mühlleitner, T. Plehn, M. Rauch, M. Spira, and K. Walz, “Precision Measurements of Higgs Couplings: Implications for New Physics Scales,” *J. Phys.*, vol. G41, p. 113001, 2014.
- [5] ATLAS Collaboration, “Observation of Higgs boson production in association with a top quark pair at the LHC with the ATLAS detector,” *Phys. Lett.*, vol. B784, pp. 173–191, 2018.
- [6] CMS Collaboration, “Observation of  $t\bar{t}H$  production,” *Phys. Rev. Lett.*, vol. 120, no. 23, p. 231801, 2018.
- [7] ATLAS Collaboration, “Study of the CP properties of the interaction of the Higgs boson with top quarks using top quark associated production of the Higgs boson and its decay into two photons with the ATLAS detector at the LHC,” 4 2020.
- [8] CMS Collaboration, “Measurements of  $t\bar{t}H$  production and the CP structure of the Yukawa interaction between the Higgs boson and top quark in the diphoton decay channel,” 3 2020.
- [9] S. L. Glashow, “Partial-symmetries of weak interactions,” *Nuclear Physics*, vol. 22, no. 4, pp. 579 – 588, 1961.
- [10] A. Salam, “Elementary particle theory, Relativistic groups and analyticity,” in *Proceedings of the Eighth Nobel Symposium* (Almquist & Wiksell, ed.).
- [11] S. Weinberg, “A model of leptons,” *Phys. Rev. Lett.*, vol. 19, pp. 1264–1266, Nov 1967.
- [12] K. Olive, “Review of particle physics,” *Chinese Physics C*, vol. 40, p. 100001, oct 2016.

- 
- [13] A. Salam, “Weak and Electromagnetic Interactions,” *Conf. Proc.*, vol. C680519, pp. 367–377, 1968.
  - [14] E. Noether, “Invariant variation problems,” *Transport Theory and Statistical Physics*, vol. 1, p. 186–207, Jan 1971.
  - [15] C. S. Wu, E. Ambler, R. W. Hayward, D. D. Hoppes, and R. P. Hudson, “Experimental Test of Parity Conservation in Beta Decay,” *Phys. Rev.*, vol. 105, pp. 1413–1414, 1957.
  - [16] F. Englert and R. Brout, “Broken Symmetry and the Mass of Gauge Vector Mesons,” *Phys. Rev. Lett.*, vol. 13, pp. 321–323, 1964. [,157(1964)].
  - [17] P. W. Higgs, “Broken Symmetries and the Masses of Gauge Bosons,” *Phys. Rev. Lett.*, vol. 13, pp. 508–509, 1964. [,160(1964)].
  - [18] G. S. Guralnik, C. R. Hagen, and T. W. B. Kibble, “Global Conservation Laws and Massless Particles,” *Phys. Rev. Lett.*, vol. 13, pp. 585–587, 1964. [,162(1964)].
  - [19] Michael D. Scadron, *Advance quantum theory and its application through Feynman diagrams*. Springer-Verlag, 1979.
  - [20] LHC Higgs Cross-Section Working Group, “Handbook of LHC Higgs Cross Sections: 4. Deciphering the Nature of the Higgs Sector,” 2016.
  - [21] G. Aad *et al.*, “Combined Measurement of the Higgs Boson Mass in  $pp$  Collisions at  $\sqrt{s} = 7$  and 8 TeV with the ATLAS and CMS Experiments,” *Phys. Rev. Lett.*, vol. 114, p. 191803, 2015.
  - [22] ATLAS Collaboration, “Evidence for the spin-0 nature of the Higgs boson using ATLAS data,” *Phys. Lett.*, vol. B726, pp. 120–144, 2013.
  - [23] CMS Collaboration, “Study of the Mass and Spin-Parity of the Higgs Boson Candidate Via Its Decays to Z Boson Pairs,” *Phys. Rev. Lett.*, vol. 110, no. 8, p. 081803, 2013.
  - [24] ATLAS Collaboration, “Study of the spin and parity of the Higgs boson in diboson decays with the ATLAS detector,” *Eur. Phys. J.*, vol. C75, no. 10, p. 476, 2015. [Erratum: *Eur. Phys. J.*C76,no.3,152(2016)].
  - [25] ATLAS Collaboration, “Evidence for the associated production of the Higgs boson and a top quark pair with the ATLAS detector,” *Phys. Rev.*, vol. D97, no. 7, p. 072003, 2018.
  - [26] ATLAS Collaboration, “Search for the standard model Higgs boson produced in association with top quarks and decaying into a  $b\bar{b}$  pair in  $pp$  collisions at  $\sqrt{s} = 13$  TeV with the ATLAS detector,” *Phys. Rev.*, vol. D97, no. 7, p. 072016, 2018.
  - [27] A. David, A. Denner, M. Duehrssen, M. Grazzini, C. Grojean, G. Passarino, M. Schumacher, M. Spira, G. Weiglein, and M. Zanetti, “LHC HXSWG interim recommendations to explore the coupling structure of a Higgs-like particle,” 2012.

- 
- [28] ATLAS Collaboration, “Combined measurements of Higgs boson production and decay using up to 80 fb<sup>-1</sup> of proton-proton collision data at  $\sqrt{s} = 13$  TeV collected with the ATLAS experiment,” *Phys. Rev.*, vol. D101, no. 1, p. 012002, 2020.
  - [29] ATLAS Collaboration, “The ATLAS Experiment at the CERN Large Hadron Collider,” *JINST*, vol. 3, p. S08003, 2008.
  - [30] CMS Collaboration, “The CMS Experiment at the CERN LHC,” *JINST*, vol. 3, p. S08004, 2008.
  - [31] LHCb Collaboration, “The LHCb Detector at the LHC,” *JINST*, vol. 3, p. S08005, 2008.
  - [32] ALICE Collaboration, “The ALICE experiment at the CERN LHC,” *JINST*, vol. 3, p. S08002, 2008.
  - [33] ATLAS Collaboration, “Luminosity determination in  $pp$  collisions at  $\sqrt{s} = 13$  TeV using the ATLAS detector at the LHC,” Tech. Rep. ATLAS-CONF-2019-021, CERN, Geneva, Jun 2019.
  - [34] “ATLAS experiment (public results): Luminosity public results of Run 2.” <https://twiki.cern.ch/twiki/bin/view/AtlasPublic/LuminosityPublicResultsRun2>, 2017.
  - [35] ATLAS Collaboration, “Measurement of the Inelastic Proton-Proton Cross Section at  $\sqrt{s} = 13$  TeV with the ATLAS Detector at the LHC,” *Phys. Rev. Lett.*, vol. 117, no. 18, p. 182002, 2016.
  - [36] K. Potamianos, “The upgraded Pixel detector and the commissioning of the Inner Detector tracking of the ATLAS experiment for Run-2 at the Large Hadron Collider,” *PoS*, vol. EPS-HEP2015, p. 261, 2015.
  - [37] S. Tsuno, “Physics performance of the ATLAS pixel detector,” *Journal of Instrumentation*, vol. 12, pp. C01025–C01025, jan 2017.
  - [38] “Expected performance of the ATLAS  $b$ -tagging algorithms in Run-2,” Tech. Rep. ATL-PHYS-PUB-2015-022, CERN, Geneva, Jul 2015.
  - [39] B. Abbott *et al.*, “Production and Integration of the ATLAS Insertable B-Layer,” *JINST*, vol. 13, no. 05, p. T05008, 2018.
  - [40] G. Knoll, *Radiation Detection and Measurement*. Wiley, 2010.
  - [41] M. Aharrouche, J. Colas, L. Di Ciaccio, M. El Kacimi, O. Gaumer, M. Gouanère, D. Goujdami, R. Lafaye, S. Laplace, C. Le Maner, *et al.*, “Energy linearity and resolution of the atlas electromagnetic barrel calorimeter in an electron test-beam,” *Nuclear Instruments and Methods in Physics Research Section A: Accelerators, Spectrometers, Detectors and Associated Equipment*, vol. 568, p. 601–623, Dec 2006.
  - [42] T. Davidek, M. Volpi, and T. Zenis, “Response of the ATLAS Tile Calorimeter to Hadrons in Stand-Alone Testbeam Data,” Tech. Rep. ATL-TILECAL-PUB-2009-004. ATL-COM-TILECAL-2009-002, CERN, Geneva, Feb 2009. The note has been updated using comments received by both referees.

- 
- [43] ATLAS Collaboration, “Measurement of the muon reconstruction performance of the ATLAS detector using 2011 and 2012 LHC proton-proton collision data,” *Eur. Phys. J.*, vol. C74, no. 11, p. 3130, 2014.
  - [44] G. Aielli *et al.*, “The rpc first level muon trigger in the barrel of the atlas experiment,” *Nuclear Physics B - Proceedings Supplements*, vol. 158, pp. 11 – 15, 2006. Proceedings of the 8th International Workshop on Resistive Plate Chambers and Related Detectors.
  - [45] S. Majewski, G. Charpak, A. Breskin, and G. Mikenberg, “A thin multiwire chamber operating in the high multiplication mode,” *Nuclear Instruments and Methods in Physics Research*, vol. 217, no. 1, pp. 265 – 271, 1983.
  - [46] H. Bertelsen *et al.*, “Operation of the upgraded ATLAS Central Trigger Processor during the LHC Run 2,” *JINST*, vol. 11, no. 02, p. C02020, 2016.
  - [47] T. Cornelissen, M. Elsing, S. Fleischmann, W. Liebig, E. Moyse, and A. Salzburger, “Concepts, Design and Implementation of the ATLAS New Tracking (NEWT),” Tech. Rep. ATL-SOFT-PUB-2007-007. ATL-COM-SOFT-2007-002, CERN, Geneva, Mar 2007.
  - [48] “The Optimization of ATLAS Track Reconstruction in Dense Environments,” Tech. Rep. ATL-PHYS-PUB-2015-006, CERN, Geneva, Mar 2015.
  - [49] R. Frühwirth, “Application of kalman filtering to track and vertex fitting,” *Nuclear Instruments and Methods in Physics Research Section A: Accelerators, Spectrometers, Detectors and Associated Equipment*, vol. 262, no. 2, pp. 444 – 450, 1987.
  - [50] T. G. Cornelissen, M. Elsing, I. Gavrilenko, J.-F. Laporte, W. Liebig, M. Limper, K. Nikolopoulos, A. Poppleton, and A. Salzburger, “The global  $\chi^2$  track fitter in ATLAS,” *Journal of Physics: Conference Series*, vol. 119, p. 032013, jul 2008.
  - [51] “ATLAS experiment (public results): Event displays from Run 2 physics analyses.” <https://twiki.cern.ch/twiki/bin/view/AtlasPublic/EventDisplayRun2Physics>, 2017.
  - [52] ATLAS Collaboration, “Electron reconstruction and identification in the ATLAS experiment using the 2015 and 2016 LHC proton-proton collision data at  $\sqrt{s} = 13$  TeV,” *Eur. Phys. J.*, vol. C79, no. 8, p. 639, 2019.
  - [53] W. Lampl, S. Laplace, D. Lelas, P. Loch, H. Ma, S. Menke, S. Rajagopalan, D. Rousseau, S. Snyder, and G. Unal, “Calorimeter Clustering Algorithms: Description and Performance,” Tech. Rep. ATL-LARG-PUB-2008-002. ATL-COM-LARG-2008-003, CERN, Geneva, Apr 2008.
  - [54] ATLAS Collaboration, “Electron and photon performance measurements with the ATLAS detector using the 2015–2017 LHC proton-proton collision data,” *JINST*, vol. 14, no. 12, p. P12006, 2019.
  - [55] ATLAS Collaboration, “Electron and photon energy calibration with the ATLAS detector using 2015–2016 LHC proton-proton collision data,” *JINST*, vol. 14, no. 03, p. P03017, 2019.

- 
- [56] ATLAS Collaboration, “Muon reconstruction performance of the ATLAS detector in proton–proton collision data at  $\sqrt{s}=13$  TeV,” *Eur. Phys. J.*, vol. C76, no. 5, p. 292, 2016.
  - [57] J. Illingworth and J. Kittler, “A survey of the hough transform,” *Computer Vision, Graphics, and Image Processing*, vol. 44, no. 1, pp. 87 – 116, 1988.
  - [58] ATLAS Collaboration, “Topological cell clustering in the ATLAS calorimeters and its performance in LHC Run 1,” *Eur. Phys. J.*, vol. C77, p. 490, 2017.
  - [59] M. Cacciari, G. P. Salam, and G. Soyez, “The anti- $k_t$  jet clustering algorithm,” *JHEP*, vol. 04, p. 063, 2008.
  - [60] M. Cacciari and G. P. Salam, “Dispelling the  $N^3$  myth for the  $k_t$  jet-finder,” *Phys. Lett.*, vol. B641, pp. 57–61, 2006.
  - [61] ATLAS Collaboration, “Jet energy scale measurements and their systematic uncertainties in proton-proton collisions at  $\sqrt{s}=13$  TeV with the ATLAS detector,” *Phys. Rev.*, vol. D96, no. 7, p. 072002, 2017.
  - [62] ATLAS Collaboration, “Performance of pile-up mitigation techniques for jets in  $pp$  collisions at  $\sqrt{s}=8$  TeV using the ATLAS detector,” *Eur. Phys. J.*, vol. C76, no. 11, p. 581, 2016.
  - [63] ATLAS Collaboration, “Jet energy measurement with the ATLAS detector in proton-proton collisions at  $\sqrt{s}=7$  TeV,” *Eur. Phys. J.*, vol. C73, no. 3, p. 2304, 2013.
  - [64] ATLAS Collaboration, “Data-driven determination of the energy scale and resolution of jets reconstructed in the ATLAS calorimeters using dijet and multijet events at  $\sqrt{s}=8$  TeV,” 2015.
  - [65] ATLAS Collaboration, “Determination of the jet energy scale and resolution at ATLAS using  $Z/\gamma$ -jet events in data at  $\sqrt{s} = 8$  TeV,” 2015.
  - [66] ATLAS Collaboration, “Monte Carlo Calibration and Combination of In-situ Measurements of Jet Energy Scale, Jet Energy Resolution and Jet Mass in ATLAS,” 2015.
  - [67] ATLAS Collaboration, “ATLAS  $b$ -jet identification performance and efficiency measurement with  $t\bar{t}$  events in  $pp$  collisions at  $\sqrt{s} = 13$  TeV,” 2019.
  - [68] ATLAS Collaboration, “Secondary vertex finding for jet flavour identification with the ATLAS detector,” Tech. Rep. ATL-PHYS-PUB-2017-011, CERN, Geneva, Jun 2017.
  - [69] ATLAS Collaboration, “Optimisation and performance studies of the ATLAS  $b$ -tagging algorithms for the 2017-18 LHC run,” Tech. Rep. ATL-PHYS-PUB-2017-013, CERN, Geneva, Jul 2017.
  - [70] ATLAS Collaboration, “Topological  $b$ -hadron decay reconstruction and identification of  $b$ -jets with the JetFitter package in the ATLAS experiment at the LHC,” Tech. Rep. ATL-PHYS-PUB-2018-025, CERN, Geneva, Oct 2018.

- 
- [71] ATLAS Collaboration, “Optimisation of the ATLAS  $b$ -tagging performance for the 2016 LHC Run,” Tech. Rep. ATL-PHYS-PUB-2016-012, CERN, Geneva, Jun 2016.
- [72] ATLAS Collaboration, “Performance of missing transverse momentum reconstruction with the ATLAS detector using proton-proton collisions at  $\sqrt{s} = 13$  TeV,” *Eur. Phys. J.*, vol. C78, no. 11, p. 903, 2018.
- [73] T. Sjostrand, S. Mrenna, and P. Z. Skands, “A Brief Introduction to PYTHIA 8.1,” *Comput. Phys. Commun.*, vol. 178, pp. 852–867, 2008.
- [74] “Further ATLAS tunes of Pythia 6 and Pythia 8,” Tech. Rep. ATL-PHYS-PUB-2011-014, CERN, Geneva, Nov 2011.
- [75] S. Agostinelli *et al.*, “GEANT4: A Simulation toolkit,” *Nucl. Instrum. Meth.*, vol. A506, pp. 250–303, 2003.
- [76] ATLAS Collaboration, “The ATLAS Simulation Infrastructure,” *Eur. Phys. J.*, vol. C70, pp. 823–874, 2010.
- [77] S. Frixione, P. Nason, and G. Ridolfi, “A Positive-weight next-to-leading-order Monte Carlo for heavy flavour hadroproduction,” *JHEP*, vol. 09, p. 126, 2007.
- [78] H. B. Hartanto, B. Jager, L. Reina, and D. Wackerroth, “Higgs boson production in association with top quarks in the POWHEG BOX,” *Phys. Rev.*, vol. D91, no. 9, p. 094003, 2015.
- [79] R. D. Ball *et al.*, “Parton distributions for the LHC Run 2,” *JHEP*, vol. 04, p. 040, 2015.
- [80] A. Djouadi, J. Kalinowski, and M. Spira, “HDECAY: A Program for Higgs boson decays in the standard model and its supersymmetric extension,” *Comput. Phys. Commun.*, vol. 108, pp. 56–74, 1998.
- [81] T. Sjöstrand, S. Ask, J. R. Christiansen, R. Corke, N. Desai, P. Ilten, S. Mrenna, S. Prestel, C. O. Rasmussen, and P. Z. Skands, “An Introduction to PYTHIA 8.2,” *Comput. Phys. Commun.*, vol. 191, pp. 159–177, 2015.
- [82] “ATLAS Run 1 Pythia8 tunes,” Tech. Rep. ATL-PHYS-PUB-2014-021, CERN, Geneva, Nov 2014.
- [83] W. Beenakker, S. Dittmaier, M. Kramer, B. Plumper, M. Spira, and P. M. Zerwas, “Higgs radiation off top quarks at the Tevatron and the LHC,” *Phys. Rev. Lett.*, vol. 87, p. 201805, 2001.
- [84] W. Beenakker, S. Dittmaier, M. Kramer, B. Plumper, M. Spira, and P. M. Zerwas, “NLO QCD corrections to  $t$  anti- $t$  H production in hadron collisions,” *Nucl. Phys.*, vol. B653, pp. 151–203, 2003.
- [85] S. Dawson, L. H. Orr, L. Reina, and D. Wackerroth, “Associated top quark Higgs boson production at the LHC,” *Phys. Rev.*, vol. D67, p. 071503, 2003.
- [86] S. Dawson, C. Jackson, L. H. Orr, L. Reina, and D. Wackerroth, “Associated Higgs production with top quarks at the large hadron collider: NLO QCD corrections,” *Phys. Rev.*, vol. D68, p. 034022, 2003.

- 
- [87] Y. Zhang, W.-G. Ma, R.-Y. Zhang, C. Chen, and L. Guo, “QCD NLO and EW NLO corrections to  $t\bar{t}H$  production with top quark decays at hadron collider,” *Phys. Lett.*, vol. B738, pp. 1–5, 2014.
  - [88] S. Frixione, V. Hirschi, D. Pagani, H. S. Shao, and M. Zaro, “Weak corrections to Higgs hadroproduction in association with a top-quark pair,” *JHEP*, vol. 09, p. 065, 2014.
  - [89] T. Gleisberg, S. Hoeche, F. Krauss, M. Schonherr, S. Schumann, F. Siegert, and J. Winter, “Event generation with SHERPA 1.1,” *JHEP*, vol. 02, p. 007, 2009.
  - [90] T. Gleisberg and S. Hoeche, “Comix, a new matrix element generator,” *JHEP*, vol. 12, p. 039, 2008.
  - [91] F. Cascioli, P. Maierhofer, and S. Pozzorini, “Scattering Amplitudes with Open Loops,” *Phys. Rev. Lett.*, vol. 108, p. 111601, 2012.
  - [92] S. Schumann and F. Krauss, “A Parton shower algorithm based on Catani-Seymour dipole factorisation,” *JHEP*, vol. 03, p. 038, 2008.
  - [93] S. Hoeche, F. Krauss, M. Schonherr, and F. Siegert, “QCD matrix elements + parton showers: The NLO case,” *JHEP*, vol. 04, p. 027, 2013.
  - [94] J. M. Campbell and R. K. Ellis, “ $t\bar{t}W^{+-}$  production and decay at NLO,” *JHEP*, vol. 07, p. 052, 2012.
  - [95] S. Frixione, V. Hirschi, D. Pagani, H. S. Shao, and M. Zaro, “Electroweak and QCD corrections to top-pair hadroproduction in association with heavy bosons,” *JHEP*, vol. 06, p. 184, 2015.
  - [96] J. Alwall, R. Frederix, S. Frixione, V. Hirschi, F. Maltoni, O. Mattelaer, H. S. Shao, T. Stelzer, P. Torrielli, and M. Zaro, “The automated computation of tree-level and next-to-leading order differential cross sections, and their matching to parton shower simulations,” *JHEP*, vol. 07, p. 079, 2014.
  - [97] R. Frederix and S. Frixione, “Merging meets matching in MC@NLO,” *JHEP*, vol. 12, p. 061, 2012.
  - [98] R. Frederix, D. Pagani, and M. Zaro, “Large NLO corrections in  $t\bar{t}W^{\pm}$  and  $t\bar{t}t\bar{t}$  hadroproduction from supposedly subleading EW contributions,” *JHEP*, vol. 02, p. 031, 2018.
  - [99] M. Cacciari, M. Czakon, M. Mangano, A. Mitov, and P. Nason, “Top-pair production at hadron colliders with next-to-next-to-leading logarithmic soft-gluon resummation,” *Phys. Lett.*, vol. B710, pp. 612–622, 2012.
  - [100] P. Bärnreuther, M. Czakon, and A. Mitov, “Percent Level Precision Physics at the Tevatron: First Genuine NNLO QCD Corrections to  $q\bar{q} \rightarrow t\bar{t} + X$ ,” *Phys. Rev. Lett.*, vol. 109, p. 132001, 2012.
  - [101] M. Czakon and A. Mitov, “NNLO corrections to top-pair production at hadron colliders: the all-fermionic scattering channels,” *JHEP*, vol. 12, p. 054, 2012.

- 
- [102] M. Czakon and A. Mitov, “NNLO corrections to top pair production at hadron colliders: the quark-gluon reaction,” *JHEP*, vol. 01, p. 080, 2013.
  - [103] M. Czakon, P. Fiedler, and A. Mitov, “Total Top-Quark Pair-Production Cross Section at Hadron Colliders Through  $O(\alpha_s^4)$ ,” *Phys. Rev. Lett.*, vol. 110, p. 252004, 2013.
  - [104] J. Pumplin, D. R. Stump, J. Huston, H. L. Lai, P. M. Nadolsky, and W. K. Tung, “New generation of parton distributions with uncertainties from global QCD analysis,” *JHEP*, vol. 07, p. 012, 2002.
  - [105] P. M. Nadolsky, H.-L. Lai, Q.-H. Cao, J. Huston, J. Pumplin, D. Stump, W.-K. Tung, and C. P. Yuan, “Implications of CTEQ global analysis for collider observables,” *Phys. Rev.*, vol. D78, p. 013004, 2008.
  - [106] P. Z. Skands, “Tuning Monte Carlo Generators: The Perugia Tunes,” *Phys. Rev. D*, vol. 82, p. 074018, 2010.
  - [107] M. Czakon and A. Mitov, “Top++: A Program for the Calculation of the Top-Pair Cross-Section at Hadron Colliders,” *Comput. Phys. Commun.*, vol. 185, p. 2930, 2014.
  - [108] M. H. Seymour and A. Siodmok, “Constraining MPI models using  $\sigma_{eff}$  and recent Tevatron and LHC Underlying Event data,” *JHEP*, vol. 10, p. 113, 2013.
  - [109] P. Golonka and Z. Was, “PHOTOS Monte Carlo: A Precision tool for QED corrections in  $Z$  and  $W$  decays,” *Eur. Phys. J.*, vol. C45, pp. 97–107, 2006.
  - [110] L. Harland-Lang, A. Martin, P. Motylinski, and R. Thorne, “Parton distributions in the LHC era: MMHT 2014 PDFs,” *Eur. Phys. J. C*, vol. 75, no. 5, p. 204, 2015.
  - [111] H.-L. Lai, M. Guzzi, J. Huston, Z. Li, P. M. Nadolsky, J. Pumplin, and C. P. Yuan, “New parton distributions for collider physics,” *Phys. Rev.*, vol. D82, p. 074024, 2010.
  - [112] M. Bahr *et al.*, “Herwig++ Physics and Manual,” *Eur. Phys. J.*, vol. C58, pp. 639–707, 2008.
  - [113] T. Sjostrand, P. Eden, C. Friberg, L. Lonnblad, G. Miu, S. Mrenna, and E. Norrbin, “High-energy physics event generation with PYTHIA 6.1,” *Comput. Phys. Commun.*, vol. 135, pp. 238–259, 2001.
  - [114] R. Ospanov, R. T. Roberts, and T. R. Wyatt, “Tagging non-prompt electrons and muons,” Tech. Rep. ATL-COM-PHYS-2016-1444, CERN, Geneva, Oct 2016.
  - [115] ATLAS Collaboration, “Analysis of  $t\bar{t}H$  and  $t\bar{t}W$  production in multilepton final states with the ATLAS detector,” Tech. Rep. ATLAS-CONF-2019-045, CERN, Geneva, Oct 2019.
  - [116] ATLAS Collaboration, “Tagging and suppression of pileup jets,” 2014.
  - [117] “Modelling of the  $t\bar{t}H$  and  $t\bar{t}V$  ( $V = W, Z$ ) processes for  $\sqrt{s} = 13$  TeV ATLAS analyses,” Tech. Rep. ATL-PHYS-PUB-2016-005, CERN, Geneva, Jan 2016.



- 
- [118] ATLAS Collaboration, “Measurement of the  $t\bar{t}Z$  and  $t\bar{t}W$  production cross sections in multilepton final states using  $3.2 \text{ fb}^{-1}$  of  $pp$  collisions at  $\sqrt{s} = 13 \text{ TeV}$  with the ATLAS detector,” *Eur. Phys. J.*, vol. C77, no. 1, p. 40, 2017.
  - [119] ATLAS Collaboration, “Measurement of the  $W^\pm Z$  boson pair-production cross section in  $pp$  collisions at  $\sqrt{s} = 13 \text{ TeV}$  with the ATLAS Detector,” *Phys. Lett.*, vol. B762, pp. 1–22, 2016.
  - [120] ATLAS Collaboration, “Measurement of the  $W^+W^-$  production cross section in  $pp$  collisions at a centre-of-mass energy of  $\sqrt{s} = 13 \text{ TeV}$  with the ATLAS experiment,” *Phys. Lett.*, vol. B773, pp. 354–374, 2017.
  - [121] ATLAS Collaboration, “Measurement of fiducial and differential  $W^+W^-$  production cross-sections at  $\sqrt{s} = 13 \text{ TeV}$  with the ATLAS detector,” *Eur. Phys. J.*, vol. C79, no. 10, p. 884, 2019.
  - [122] ATLAS Collaboration, “Observation of electroweak production of a same-sign  $W$  boson pair in association with two jets in  $pp$  collisions at  $\sqrt{s} = 13 \text{ TeV}$  with the ATLAS detector,” *Phys. Rev. Lett.*, vol. 123, no. 16, p. 161801, 2019.
  - [123] ATLAS Collaboration, “Measurement of the  $t\bar{t}Z$  and  $t\bar{t}W$  cross sections in proton-proton collisions at  $\sqrt{s} = 13 \text{ TeV}$  with the ATLAS detector,” *Phys. Rev.*, vol. D99, no. 7, p. 072009, 2019.
  - [124] M. Pinamonti, L. Valery, et al., “The TRExFitter package for statistical analysis..” <https://twiki.cern.ch/twiki/bin/viewauth/AtlasProtected/TtHFitter>, 2019.
  - [125] G. Cowan, *Statistical Data Analysis*. Clarendon Press, 1998.
  - [126] G. Cowan, K. Cranmer, E. Gross, and O. Vitells, “Asymptotic formulae for likelihood-based tests of new physics,” *Eur. Phys. J.*, vol. 71, p. 1554, Feb 2011.
  - [127] K. Cranmer, G. Lewis, L. Moneta, A. Shibata, and W. Verkerke, “HistFactory: A tool for creating statistical models for use with RooFit and RooStats,” Tech. Rep. CERN-OPEN-2012-016, New York U., New York, Jan 2012.
  - [128] W. Verkerke and D. Kirkby, “The roofit toolkit for data modeling,” 2003.
  - [129] W. Verkerke and D. P. Kirkby, “RooFit Users Manual..” <http://roofit.sourceforge.net>, 2019.
  - [130] R. M. L. Team, “Minuit2 minimization package..” <http://project-mathlibs.web.cern.ch/project-mathlibs/sw/Minuit2/html/index.html>, 2019.
  - [131] S. S. Wilks, “The Large-Sample Distribution of the Likelihood Ratio for Testing Composite Hypotheses,” *Ann. Math. Statist.*, vol. 9, pp. 60–62, 03 1938.
  - [132] A. Wald, “Tests of statistical hypotheses concerning several parameters when the number of observations is large,” *Trans. Amer. Math. Soc.*, vol. 54, pp. 426–482, 1943.
  - [133] J. Bellm *et al.*, “Herwig 7.0/Herwig++ 3.0 release note,” *Eur. Phys. J.*, vol. C76, no. 4, p. 196, 2016.

- 
- [134] J. Butterworth *et al.*, “PDF4LHC recommendations for LHC Run 2,” *J. Phys.*, vol. G43, p. 023001, 2016.